IRE
Transactions
on ANTENNAS and PROPAGATION

Volume AP-5 OCTOBER, 1957 Number 4

Published Quarterly

TABLE OF CONTENTS

PUBLISHED BY THE
Professional Group on Antennas and Propagation

IRE TRANSACTIONS® PGAP IS A QUARTERLY PUBLICATION DEVOTED TO EXPERIMENTAL AND THEORETICAL PAPERS ON ANTENNAS AND WIRELESS PROPAGATION OF ELECTROMAGNETIC WAVES

MANUSCRIPTS should be submitted to John B. Smyth, Editor, Smyth Research Associates, 3930 4th Avenue, San Diego 3, Calif. Manuscripts should be original typewritten copy, double spaced, plus one carbon copy. References should appear as footnotes and include author's name, title, journal, volume, initial and final page numbers, and date. Each paper must have a summary of not more than 200 words. News items concerning PGAP members and group activities should be sent to the News Editor, Mr. Arthur Dorne, Dorne and Margolin, Inc., 30 Sylvester Street, Westbury, L.I., N.Y.

ILLUSTRATIONS should be submitted as follows: All line drawings (graphs, charts, block diagrams, cutaways, etc.) should be inked uniformly and ready for reproduction. If commercially printed grids are used in graph drawings, author should be sure printer's ink is of a color that will reproduce. All halftone illustrations (photographs, wash, airbrush, or pencil renderings, etc.) should be clean and ready to reproduce. Photographs should be glossy prints. Call-outs or labels should be marked on a registered tissue overlay, not on the illustration itself. No illustration should be larger than 8 x 10 inches.

Copies can be purchased from
THE INSTITUTE OF RADIO ENGINEERS
1 East 79 St., New York 21, N.Y.

PRICE PER COPY: members of the Professional Group on Antennas and Propagation, $1.70; members of the IRE, $2.55; nonmembers, $5.10.

ANNUAL SUBSCRIPTION PRICE: PGAP members, included in PGAP assessment of $4.00; IRE members, $8.50; Colleges and public libraries, $10.00; nonmembers, $17.00.

IRE TRANSACTIONS ON ANTENNAS AND PROPAGATION

Entered as second-class matter, at the post office at Menasha, Wisconsin, under the act of August 24, 1912. Acceptance for mailing at a special rate of postage is provided for in the act of February 28, 1925, embodied in Paragraph 4, Section 412, P. L. & R., authorized October 26, 1927.

news and views

Administrative News

Finances

Since the May meeting of the Administrative Committee there has been considerable activity directed toward the selling of advertising and otherwise relieving the financial problems of PGAP. In particular, there was a meeting at Boulder, Colo. during the URSI General Assembly which is briefly reported below under news from that chapter. To date, over $6000.00 in firm commitments have been received for advertisements to appear in this and the next three issues. This represents approximately 60 per cent of the total estimated amount needed in addition to our anticipated income from membership dues of approximately $12,000.00. It seems hopeful that within the next few months we will solve our financial problems and the publication difficulties to which they give rise.

Administrative Committee

The following are the current members of the Administrative Committee and their assignments:

Elected Members—Terms Expire 1958: J. I. Bohnert, Chairman, H. G. Booker, Library Subscriptions, D. D. King, Awards, J. B. Smyth, PGAP Editor.

Elected Members—Terms Expire 1959: A. Dorne, News and Views Editor, F. T. Haddock, Radio Astronomy Issue of PROCEEDINGS, J. W. Herbstreit, Technical Symposia, R. L. Mattingly, Vice-Chairman and Membership.

Elected Members—Terms Expire 1960: J. W. Findlay, 1958 National Convention Program, R. K. Moore, Paper Procurement, Wm. H. Radford, No official assignment, O. G. Villard, Chapter Organization.

Ex Officio Members (Past Chairmen): P. S. Carter, term expires 1959; D. C. Ports, now assigned to Advertising, term expires 1960; A. H. Waynick, now assigned to Student Membership, term expires 1958.

Honorary Member: L. C. Van Atta.

Assisting Members—Appointed: S. A. Bowhill, Propagation Papers Review, C. Goatley, Secretary-Treasurer, S. M. King, 1958 NATIONAL CONVENTION RECORD, V. H. Rumsey, Antenna Papers Review, R. C. Spencer, PROCEEDINGS-TRANSACTIONS Liaison.

Comment: Questions or comments regarding any phase of the activity of the Administrative Committee are, of course, the prerogative of any PGAP member. One such letter recently has been received. It is published here, together with the reply that was sent the writer, because it concerns an issue which may trouble other members. Any further comments will be welcomed by this department.

"Dear Dr. Mattingly:

"This is to express profound concern over the recent 'election' to fill four vacancies on the PGAP Administrative Committee. Such 'rubber-stamp' procedures as this, in which only four candidates are nominated for an equal number of posts, make a mockery of the democratic process of voting, and the ballot becomes equal to a proxy.

"Incidentally, it is a constant source of wonderment to students from abroad to witness, in many of our organizations, such hypocritical practices, which seem to conflict with the American ideals we assert, and that are very difficult to explain away.

"It is respectfully suggested that the PGAP By-Laws be appropriately modified to allow for genuine elections in the future."

ROBERT COHEN
857 18th Street
Boulder, Colo.

"Dear Mr. Cohen:

"Thank you for your letter of June 22, 1957, in which you indicate your concern over the procedures used in the election to fill vacancies on the PGAP Administrative Committee.

"As I am sure that you realize, it is not the intent of the Administrative Committee to usurp the democratic birthright of the American citizen. However, we who are interested in the PGAP must do what we can to insure that the PGAP is administered by individuals with proven capabilities and work capacity and whose business affiliations place them in a position to carry out the uninspiring and often arduous business details of our organizations. In addition, as explained in the note accompanying the recent ballot, we must strive for a reasonable balance of representation between the antenna and propagation areas, between various geographical regions and to introduce spokesmen for such special fields, as radio astronomy, which we feel fall properly within our cognizance. It is just this sort of thinking that dictates the apparent arbitrary manner in which elections are held in other scientific organizations.

"As you imply, we could submit a list of, say, eight names from which the membership could make their choices for the four vacancies. As a matter of fact, we have done substantially this in the past. However, it has been our experience, and the experience of many other similar societies that this procedure does not serve the best interests of the group.

"I hope that you do not imagine that the write-in votes go for naught. While it is true that a write-in election would be difficult to bring about, write-in nominations are carefully tabulated, including the single-vote cases, and where there is a definite expression for certain candidates, these are considered by our nominating committee for subsequent elections. Furthermore, our local Chapters have a good deal to say in the choice of candidates. As an example, Professor Moore, recently elected to the Administrative Committee, was suggested by our Albuquerque Chapter.

"Let me assure you that there is no conspiracy on the part of the Administrative Committee to restrict admission to this body. The Administrative Committee sincerely tries, within the limitation of human frailties, to make the choice of the membership-at-large their choice, provided that certain necessary qualifications, established often by bitter experience, are met.

"I shall take pleasure in submitting your letter for consideration by the Administrative Committee at its next meeting. Thank you again for your expression of feeling."

ROBERT L. MATTINGLY
Vice-Chairman, PGAP.

CHAPTER NEWS

Chicago

The Chicago Chapter meeting took place September 13, 1957. Norman J. Foot, Assistant Chief Engineer in charge of the Antenna Section of the Hallicrafters Airborne Laboratory spoke on "Introduction to the Scimitar Antenna." The Scimitar is a very broad-band and and highly efficient antenna, the impedance and patterns of which are nearly independent of frequency. It is related to the family of antennas whose shapes are specified entirely by angles. The meeting was well attended.

Denver-Boulder

During the two-week period—August 23 to September 5, 1957—the International Scientific Radio Union (URSI) held its triennial meeting in Boulder, Colo. This Twelfth General Assembly, was the first such meeting held in the United States since 1927. Many of the sessions of the seven commissions of the Union contained material of great interest to the members of the PGAP. The occasion drew together many of the national officers of both the IRE and the PGAP. To take advantage of this, a joint business meeting of IRE executive and PGAP administrative committees was held at the Boulder Laboratories of the National Bureau of Standards on August 29th. The officers of the Denver-Boulder section of IRE and Denver-Boulder Chapter of the PGAP participated.

The attendance was approximately twenty-five and included among others, J. T. Henderson, President, IRE; Dr. Yasujiro Niwa, Vice-President, IRE, and Chairman of the Tokyo Section; Dr. Isaac Koga, Vice-Chairman of the Tokyo Section and the newly-elected Vice-President of URSI; Dr. J. I. Bohnert, National Chairman, PGAP; R. L. Mattingly, Vice-Chairman, PGAP; C. Goatley, Secretary, PGAP; R. S. Kirby, S. B. Peterson, and W. C. Worcester, Chairman, Vice-Chairman, and Secretary, respectively, of the Denver-Boulder Section, IRE; and H. V. Cottony and A. P. Barsis, Chairman and Secretary, respectively, of the Boulder-Denver Chapter of PGAP.

Los Angeles

The Los Angeles Chapter meeting was held on September 12 at the IAS Building, 7600 Beverly Boulevard. The speakers were Dr. Joseph A. Barkson of Hughes Aircraft Corporation, who spoke on "Coupling of Rectangular Waveguides," and Kenneth C. Kelly of Hughes Aircraft, who spoke on "Recent Annular Slot Array Experiments."

Philadelphia

The new officers elected for 1957–1958 are: Chairman, Edmond J. Forbes, Radio Corporation of America, Bldg. 1-5, Camden, N. J.; Vice-Chairman, Edwin A. Fink, Philco Corporation, 4700 Wissahickon Avenue, Philadelphia, Pa.; Secretary, Frank T. Barclay, ITE Circuit Breaker, 601 E. Erie Avenue, Philadelphia, Pa.

Washington, D. C.

The new officers elected for 1957–1958 are Harry Fine, Chairman; Herschel T. Ward, Vice-Chairman; and Robert J. Adams, Secretary.

contributions

Radiation from a Radial Dipole Through a Thin Dielectric Spherical Shell*

M. G. ANDREASEN†

Summary—**The radiation from and the reaction on a radial dipole placed inside a thin dielectric spherical shell are investigated. Numerical results have been obtained for the gain pattern and the impedance change of an elementary dipole. The nearer the center of the shell the dipole is placed, the less the pattern is found to be influenced by the shell, the opposite being the case for the impedance of the dipole.**

Introduction

THE use of a dielectric shell to protect an antenna against rain water or the action of the wind, as is well known, may strongly influence the electrical properties of the antenna. Part of the energy radiated by the antenna may be reflected back into the line feeding the antenna, thus changing the antenna impedance and the broad-band properties of the antenna. Furthermore, because of internal multiple reflections from the shell, the radiation pattern may be considerably distorted.

To avoid strong reflections back into the antenna line it seems reasonable from a point of view of geometrical optics that the antenna should not be placed near any focus of the shell. On the other hand, the radiation pattern of the antenna is influenced less by the shell if it is placed nearer a focus of the shell. Therefore, a compromise usually must be made as to the position of the antenna inside the dielectric shell. The electrical thickness of the shell should be either as small as permissible, due regard being given to the mechanical strength of the shell, or it should be chosen equal to half a wavelength. For a half-wavelength shell, the electrical performance of the surrounded antenna is influenced less if the dielectric constant of the shell is higher.

It is the aim of this paper to present the results of an investigation of the influence of a thin dielectric spherical shell on the radiating properties of a radially directed Hertz dipole arbitrarily placed inside the shell. An investigation of the special case of a dipole placed at the center of a spherical shell was previously made by Keller[1] and Mirimanov.[2] The results obtained by the present investigation are expected to give a very good idea of the influence of a spherical shell on the performance of a linear antenna of finite length. The method used for solving the problem is the classical one of expanding fields in spherical harmonics.[3] This method is particularly useful when the radius of the shell is at most a few wavelengths, the necessary number of terms of the infinite sum representing the radiated field thus being reasonably small. However, when the primary field is being expanded, difficulties often may be expected. But if the interest is confined to the far-field

* Manuscript received by the PGAP, May 16, 1956.
† Siemens und Halske, Munich, Germany.

[1] J. B. Keller and H. B. Keller, "Reflection and transmission of electromagnetic waves by a spherical shell," *J. Appl. Phys.*, vol. 20, pp. 393–396; April, 1949.
[2] R. G. Mirimanov, "Radiation resistance of a dipole placed in the center of a thin spherical envelope," *Dokl. Akad. Nauk*, vol. 71, pp. 1061–1064; 1950.
[3] J. A. Stratton, "Electromagnetic Theory," McGraw-Hill Book Co., Inc. New York, N.Y.; 1941.

only, a method[4] based on the reciprocity theorem may be used with advantage, the expansion of the primary field being reduced to the expansion of a plane wave. It should be noted, however, that by using the former (direct) method the antenna reactance may be determined; this will not be the case when the latter (indirect) method is used.

Because of the general character of the present investigation the expressions obtained for the radiation through a lossless spherical shell may in a wider sense represent also the influence of an absorbent shell, the real dielectric constant of the lossless shell being replaced by a complex dielectric constant. This formal procedure leads, however, to difficulties in the numerical calculations because, as far as is known to the author, no tables of spherical wave functions of complex or even just purely imaginary argument exist.

Simplified Boundary Conditions at a Thin Shell

In order to determine the exact field transmitted through a dielectric shell, in addition to the primary field, a secondary field representing a sum of standing waves must be assumed to exist inside the shell. Outside the shell the field is represented by a sum of diverging waves, whereas in the shell the field may be represented by a sum of standing and diverging waves. Thus, there are four secondary fields and four sets of constants to be determined by satisfying the boundary conditions at the two surfaces of the shell. This procedure is necessary if the electrical thickness of the shell is great. If the shell is electrically thin, however, which is assumed in the present investigation, the shell may, to a good approximation, be replaced by an infinitely thin shell, the dielectric constant of which approaches infinity so that the product of the infinitesimal thickness and the dielectric constant of the shell approaches a constant value. Thus, only two secondary fields need to be determined. To illustrate this, consider a dielectric shell of dielectric constant ϵ, permeability μ, and a thickness d, which is assumed to be negligible as compared to the smallest radius of curvature of the shell. The shell is placed in free space. Assuming the electrical thickness of the shell to be small, the discontinuity of the tangential magnetic field across the shell is approximately equal to the displacement current in the shell. Thus, if we use the time factor $e^{j\omega t}$

$$\hat{n} \times (\overline{H}_2 - \overline{H}_1) = j\omega\epsilon d(\hat{n} \times \overline{E}_s) \times \hat{n}, \qquad (1)$$

the shell dividing the space into the regions 1 and 2, $\hat{n}$ being a unit vector normal to the shell from medium 1 to medium 2, and $(\hat{n}\times\overline{E}_s)\times\hat{n}\sim\frac{1}{2}\hat{n}\times(\overline{E}_1+\overline{E}_2)\times\hat{n}$ being the mean tangential electric field in the shell. Similarly, the discontinuity of the tangential electric field across the shell is approximately equal to the magnetic current in the shell

$$\hat{n} \times (\overline{E}_2 - \overline{E}_1) = -j\omega\mu d(\hat{n} \times \overline{H}_s) \times \hat{n}, \qquad (2)$$

$(\hat{n}\times\overline{H}_s)\times\hat{n}\sim\frac{1}{2}\hat{n}\times(\overline{H}_2+\overline{H}_1)\times\hat{n}$ being the mean tangential magnetic field in the shell. Now, letting the shell shrink to a shell of infinitesimal thickness δ, dielectric constant ϵ', and permeability μ' the boundary conditions (1) and (2) at the original shell are preserved by this process when in these conditions we replace ϵd by $\epsilon_0(d-\delta)+\epsilon'\delta$ and μd by $\mu_0(d-\delta)+\mu'\delta$, thus setting $(\epsilon'-\epsilon_0)\delta=(\epsilon-\epsilon_0)d$ and $(\mu'-\mu_0)\delta=(\mu-\mu_0)d$. The boundary conditions at the infinitesimal shell are then, as we pass to the limit $\delta\to 0$, $\epsilon'\to\infty$ and $\mu'\to\infty$,

$$\hat{n} \times (\overline{H}_2 - \overline{H}_1) = j\omega(\epsilon - \epsilon_0)d(\hat{n} \times \overline{E}_s) \times \hat{n} \qquad (3)$$

$$\hat{n} \times (\overline{E}_2 - \overline{E}_1) = -j\omega(\mu - \mu_0)d(\hat{n} \times \overline{H}_s) \times \hat{n}. \qquad (4)$$

In what follows we assume $\mu=\mu_0$. Thus the magnetic current in the infinitesimal shell is zero, and the boundary conditions are reduced to

$$\hat{n} \times (\overline{H}_2 - \overline{H}_1) = Y(\hat{n} \times \overline{E}_1) \times \hat{n} = Y(\hat{n} \times \overline{E}_2) \times \hat{n} \qquad (5)$$

where

$$Y = j\frac{B}{\zeta} = j\omega(\epsilon - \epsilon_0)d = j\frac{(\kappa_e - 1)kd}{\zeta} \qquad (6)$$

is the admittance of the shell, κ_e being the relative dielectric constant of the original shell, and ζ and k being the specific impedance and propagation constant respectively of free space. The simplified boundary conditions (5) have been shown to be less approximate, the larger the dielectric constant of the actual shell is and the smaller the gradient along the surface of the shell of the electric field component normal to the shell is when compared with the value of the tangential electric field at the shell.

Primary Field

For the purposes of the following calculations a spherical coordinate system (r, θ, ϕ) (Fig. 1) is introduced, the dipole being placed at the point $(x, y, z)=(0, 0, r_0)$ inside an equivalent infinitely thin shell $r=r_1$. The fields produced by the radial dipole are evidently of the TM-type and are independent of ϕ. Thus a magnetic vector potential[5]

$$\overline{A} = rA\hat{r} \qquad (7)$$

may be introduced appropriately, $\nabla\times\overline{A}$ being equal to the magnetic induction $\overline{B}$. The scalar potential A must satisfy the wave equation $(\nabla^2+k^2)A=0$, the solutions of which determine the electromagnetic field vectors through the spherical components

$$j\omega\mu\epsilon E_r = \frac{\partial^2(rA)}{\partial r^2} + k^2(rA)$$

$$j\omega\mu\epsilon E_\theta = \frac{1}{r}\frac{\partial^2(rA)}{\partial r\partial\theta}$$

$$j\omega\mu\epsilon E_\phi = \frac{1}{r\sin\theta}\frac{\partial^2(rA)}{\partial r\partial\phi} \qquad (8)$$

[4] P. S. Carter, "Antenna arrays around cylinders," Proc. IRE, vol. 31, pp. 671–693; December, 1943.

[5] P. Frank and R. v. Mises, "Die Differentialgleichungen der Physik," Friedr. Vieweg & Sohn, Braunschweig, 2nd ed.; 1935.

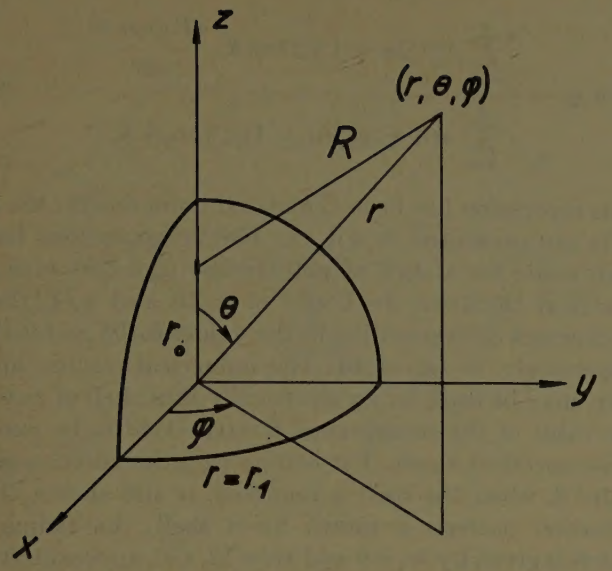

Fig. 1—Coordinate system used for the calculations.

$$H_r = 0$$

$$\mu H_\theta = \frac{1}{\sin\theta}\frac{\partial A}{\partial \phi}$$

$$\mu H_\phi = -\frac{\partial A}{\partial \theta}. \tag{9}$$

The scalar potential A_{pr} of the field radiated by a radial current distribution in free space must satisfy the inhomogeneous wave equation

$$(\nabla^2 + k^2)A_{pr} = -\frac{\mu_0 J_r}{r}, \tag{10}$$

J_r being the current density. Integrating this equation for the elementary dipole we obtain for the potential at the point (r, θ, ϕ) (see Fig. 1)

$$A_{pr} = \frac{\mu_0}{4\pi}\frac{I\Delta l}{r_0}\frac{e^{-jkR}}{R}, \tag{11}$$

I being the prescribed current of the dipole and Δl the length of the dipole. This expression is expanded in spherical harmonics,[3] giving

$$A_{pr} = \frac{C}{r_0} h_0^{(2)}(kR)$$

$$= \sum_{n=0}^{\infty} \frac{C}{r_0}(2n+1) j_n(kr_0) h_n^{(2)}(kr) P_n(\cos\theta), \tag{12}$$

which is valid for $r > r_0$; and where for simplicity a dipole constant C has been introduced,

$$C = -\frac{j\mu_0 k}{4\pi} I\Delta l. \tag{13}$$

The notations used here for the spherical Bessel function j_n and for the spherical Hankel function of the second kind h_n^2 are in accordance with those used by Morse.[6] $P_n(\cos\theta)$ is the Legendre polynomial of nth order.

[6] P. M. Morse, "Vibration and Sound," McGraw-Hill Book Co., Inc., New York, N. Y.; 1936.

Transmitted Field

The magnetic potential A_1 of the field inside the shell is taken to be the sum of the primary potential and a secondary potential representing standing waves

$$A_1 = A_{pr} + A_{1sek}$$

$$= \sum_{n=0}^{\infty}\left[\frac{C}{r_0}(2n+1) j_n(kr_0) h_n^{(2)}(kr) + a_n j_n(kr)\right] \cdot P_n(\cos\theta). \tag{14}$$

Outside the shell the potential must represent diverging waves, thus

$$A_2 = \sum_{n=0}^{\infty} b_n h_n^{(2)}(kr) P_n(\cos\theta). \tag{15}$$

The constants a_n and b_n are to be determined so as to make the resultant field satisfy the boundary conditions at the shell. Inserting (8) and (9) into (5), these conditions are seen to be given by

$$\frac{\partial(krA_1)}{\partial(kr)} = \frac{\partial(krA_2)}{\partial(kr)} = \frac{1}{(\kappa_e - 1)kd} kr_1(A_2 - A_1)\Big|_{r=r_1}. \tag{16}$$

Making use of the Wronskian

$$\rho j_n(\rho)\frac{d[\rho h_n^{(2)}(\rho)]}{d\rho} - \rho h_n^{(2)}(\rho)\frac{d[\rho j_n(\rho)]}{d\rho} = -j. \tag{17}$$

We derive from (14)–(16) the constants a_n and b_n to be

$$b_n = \frac{C}{r_0}(2n+1) j_n(kr_0) R_n \tag{18}$$

$$a_n = -j(\kappa_e - 1)kd\left[\frac{d[kr_1 h_n^{(2)}(kr_1)]}{d(kr_1)}\right]^2 b_n \tag{19}$$

where for simplicity a constant

$$R_n = \frac{1}{1 + j(\kappa_e - 1)kd\dfrac{d[kr_1 j_n(kr_1)]}{d(kr_1)}\dfrac{d[kr_1 h_n^{(2)}(kr_1)]}{d(kr_1)}}, \tag{20}$$

depending only on the parameters of the spherical shell, has been introduced.

The field transmitted through the dielectric shell may now be found by introducing (15) into (8) and (9). Making use at the same time of the differential equation for spherical Bessel functions,[3]

$$\rho^2 z_n''(\rho) + 2\rho z_n'(\rho) + [\rho^2 - n(n+1)]z_n(\rho) = 0, \tag{21}$$

the nonzero components of the transmitted field are found to be

$$E_{2r} = \frac{\zeta}{j\mu_0}\sum_{n=0}^{\infty} b_n n(n+1)\frac{h_n^{(2)}(kr)}{kr} P_n(\cos\theta)$$

$$E_{2\theta} = \frac{\zeta}{j\mu_0}\sum_{n=0}^{\infty} b_n \frac{1}{kr}\frac{d[krh_n^{(2)}(kr)]}{d(kr)}\frac{dP_n(\cos\theta)}{d\theta}$$

$$H_{2\phi} = -\frac{1}{\mu_0}\sum_{n=0}^{\infty} b_n h_n^{(2)}(kr)\frac{dP_n(\cos\theta)}{d\theta}. \tag{22}$$

This represents the field at any point (r, θ, ϕ) outside the spherical shell. For practical purposes the interest attaches primarily to the far field. Inserting the asymptotic expression for the spherical Hankel function of the second kind,[3]

$$h_n^{(2)}(\rho) = j^{n+1}\frac{e^{-i\rho}}{\rho} \qquad \rho \gg n, \tag{23}$$

we find the far field (22) to be given by

$$E_{2\theta} = -\frac{\zeta}{\mu_0}\frac{e^{-ikr}}{kr}\sum_{n=0}^{\infty} j^{n+1}b_n\frac{dP_n(\cos\theta)}{d\theta}$$

$$H_{2\phi} = -\frac{1}{\mu_0}\frac{e^{-ikr}}{kr}\sum_{n=0}^{\infty} j^{n+1}b_n\frac{dP_n(\cos\theta)}{d\theta}. \tag{24}$$

The r component of (22) has been neglected as this component is small of second order. In order to discuss these results the antenna gain will be calculated in the next section and will be made the object of numerical computations so as to give an idea of the influence of a spherical shell on the radiation pattern of an actual dipole.

Antenna Gain

The antenna gain of an antenna system of rotational symmetry is defined by

$$G(\theta, \phi) = 4\pi\frac{P(\theta, \phi)}{P_T} = 2\frac{P(\theta, \phi)}{\int_0^{\pi} P(\theta, \phi)\sin\theta d\theta}, \tag{25}$$

$P(\theta, \phi)$ and $P_T/4\pi$ being the actual and the mean power, respectively, transmitted per unit solid angle in the direction (θ, ϕ). To find the antenna gain of the radial dipole placed inside the spherical shell $P(\theta, \phi)$ is replaced by $P(\theta, \phi) = r^2|E_{2\theta}|^2/2\zeta$, $E_{2\theta}$ being the far-zone electric field from (24). Thus

$$G(\theta, \phi) = 2\frac{\left|\sum_{n=0}^{\infty} j^{n+1}b_n\frac{dP_n(\cos\theta)}{d\theta}\right|^2}{\int_0^{\pi}\left|\sum_{n=0}^{\infty} j^{n+1}b_n\frac{dP_n(\cos\theta)}{d\theta}\right|^2\sin\theta d\theta}. \tag{26}$$

The denominator of this expression may be transformed by the aid of the following orthogonality relations for the Legendre polynomials[3]

$$\int_0^{\pi}\frac{dP_n(\cos\theta)}{d\theta}\frac{dP_m(\cos\theta)}{d\theta}\sin\theta d\theta = \begin{cases} 0 & \text{for } n \neq m \\ \dfrac{2n(n+1)}{2n+1} & \text{for } n = m. \end{cases} \tag{27}$$

Then, performing the integration of (26) and introducing b_n from (18), the antenna gain is reduced to

$$G(\theta, \phi) = \frac{\left|\sum_{n=0}^{\infty} j^{n+1}(2n+1)j_n(kr_0)R_n\frac{dP_n(\cos\theta)}{d\theta}\right|^2}{\sum_{n=0}^{\infty} n(n+1)(2n+1)j_n^2(kr_0)|R_n|^2}. \tag{28}$$

This expression has been calculated numerically; the results are presented in Fig. 2. The computations have been made for a shell of polystyrene ($\kappa_e = 2.6$) with an electrical thickness $\theta = \sqrt{\kappa_e}kd$ of $\pi/16$ and $\pi/4$, these thicknesses corresponding to the values 0.195 and 0.779, respectively, of $(\kappa_e - 1)kd$. The numerical results, however, may be used for an electrically thin shell of any κ_e, the value of the susceptance $B = (\kappa_e - 1)kd$ to be one of those specified above. For comparison the antenna gain $\frac{3}{2}\sin^2\theta$, when the shell is removed, is also shown. The radiation pattern is shown for a shell, the radius of which is given by $kr_1 = 9$ and $kr_1 = 12$, *i.e.*, approximately 1.5 and 2 wavelengths, respectively. Two values 3 and 6 of the electrical distance kr_0 from the dipole to the center of the shell have been considered. From the patterns the disturbing influence of the thin shell on the radiation from the dipole is seen to be the more pronounced, the greater the susceptance $B = (\kappa_e - 1)kd$ of the shell is. Thus, in order to obtain a small distortion of the pattern for any r_0 and r_1, the chosen susceptance $(\kappa_e - 1)kd$ should never exceed 0.2. The dipole is seen to radiate a relatively large amount of the transmitted energy in directions close to $\theta = 180°$. This type of distortion is seen to be stronger, if the susceptance of the shell and the distance of the dipole from the center of the shell are greater. To avoid strong distortion of the pattern, r_0 should not be chosen greater than one wavelength ($kr_0 \sim 6$). The radius r_1 of the shell is seen to influence the pattern much less than r_0. Results that are not to be discussed here, have been obtained for a shell with a radius of approximately one wavelength and show that the shell distorts the pattern only slightly. This is to be expected according to Rayleigh's law of scattering.

Antenna Impedance

The spherical shell reacts upon the surrounded antenna, a wave being reflected back along the antenna line, thus changing the antenna impedance. To determine the resistance of the dipole inside the spherical shell the Poynting vector method may be used. To determine the reactance also, the emf method may be used. According to the former method the radiation resistance R_A is expressed by

$$R_A = 2\frac{P_T}{|I|^2}. \tag{29}$$

The total power transmitted by the dipole is found from the preceding section to amount to

$$P_T = \frac{2\pi\xi}{(\mu_0 k)^2}\sum_{n=0}^{\infty}|b_n|^2\frac{n(n+1)}{2n+1}. \tag{30}$$

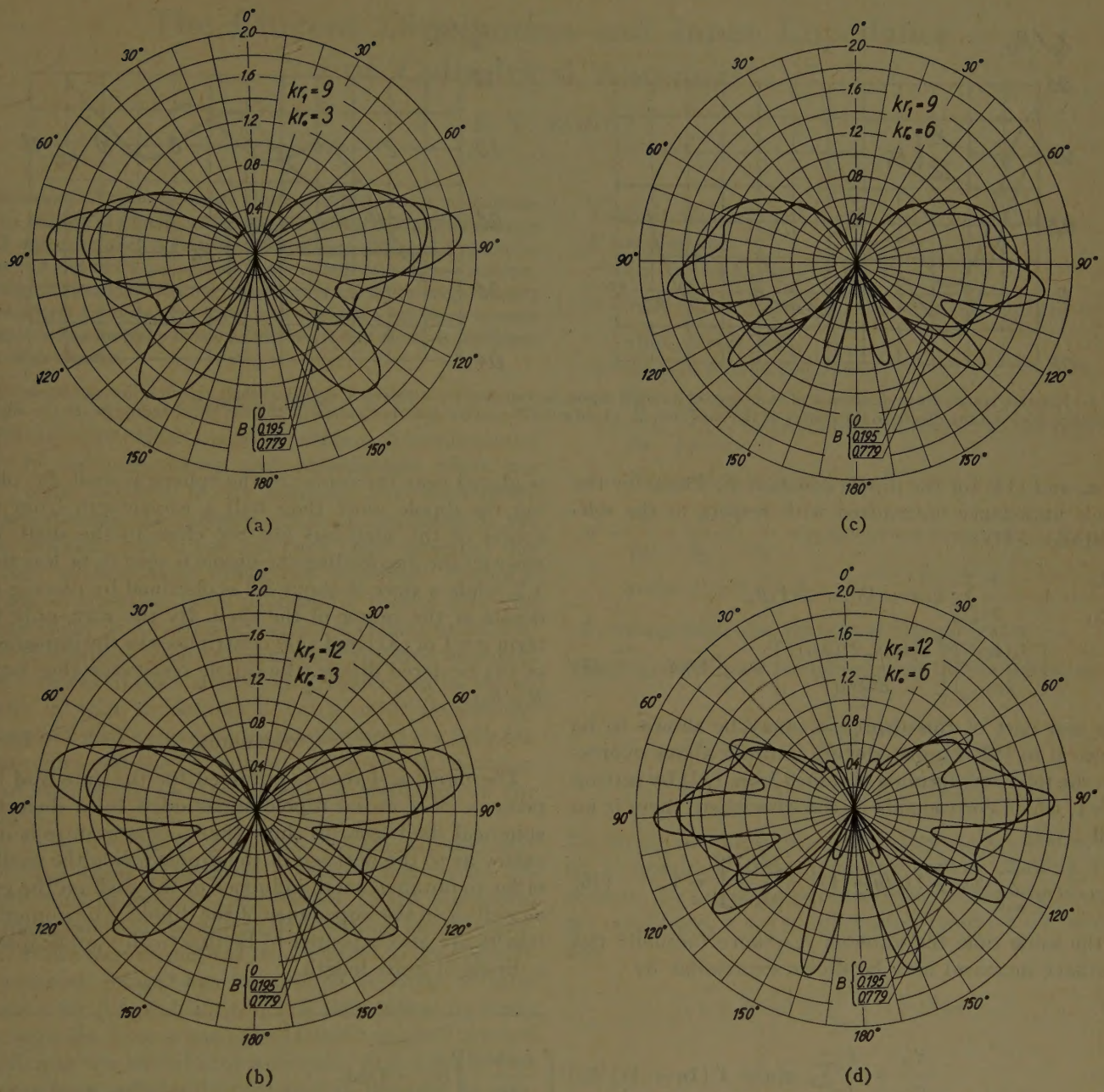

Fig. 2—Primary radiation pattern of a radial dipole surrounded by a dielectric spherical shell for different values of the electrical radius kr_1 and susceptance $B = (\kappa_e - 1)kd$ of the shell and the electrical distance kr_0 from the dipole to the center of the shell.

Introducing (18) for b_n and (13) for C, the radiation resistance of the dipole normalized with respect to the self-resistance R_{11} of the dipole

$$R_{11} = \frac{\zeta}{6\pi}(k\Delta l)^2 \tag{31}$$

is found from (29) to be expressible by

$$\frac{R_A}{R_{11}} = \frac{3}{2}\sum_{n=0}^{\infty} n(n+1)(2n+1)\,|R_n|^2\left[\frac{j_n(kr_0)}{kr_0}\right]^2. \tag{32}$$

Next, let us find the dipole impedance by the emf method,[7] according to which, assuming the dipole to be matched with the shell removed (it is no loss of generality to assume that)

$$Z_A = R_{11} - \frac{E_r \Delta l}{I}, \tag{33}$$

I being the prescribed current of the dipole and E_r the radial electric component of the secondary field in the position of the dipole inside the shell, which component is found from (8) and (14) to be

$$E_r = \frac{\zeta}{j\mu_0}\sum_{n=0}^{\infty} a_n n(n+1)\frac{j_n(kr_0)}{kr_0}, \tag{34}$$

use being made of the differential equation (21). We introduce this into (33) and insert at the same time (19)

[7] R. E. Burgess, "Aerial characteristics," *Wireless Eng.*, vol. 21, pp. 154–160; April, 1944.

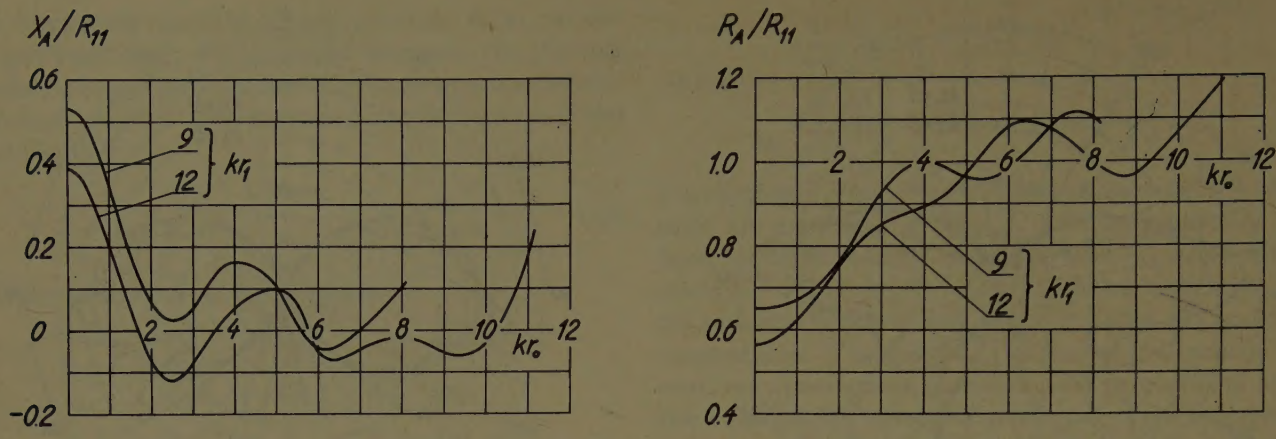

Fig. 3—Relative resistance and increase of reactance of a radial dipole surrounded by a dielectric spherical shell as a function of the electrical distance kr_0 from the dipole to the center of the shell, for $(\kappa_e-1)kd=0.779$ and for different values of the electrical radius kr_1 of the shell.

for a_n and (13) for the dipole constant C. Thus, for the dipole impedance normalized with respect to the self-resistance (31)

$$\frac{Z_A}{R_{11}} = 1 - \frac{3}{2}\sum_{n=0}^{\infty} n(n+1)(2n+1)R_n \cdot \left[\frac{j_n(kr_0)}{kr_0}\right]^2\left[\frac{d[kr_1 h_n^{(2)}(kr_1)]}{d(kr_1)}\right]^2(\kappa_e-1)kd. \quad (35)$$

The real part of this expression may be shown to be identical to (32) by introducing into the above expression the following formula obtained from (32) by setting $R_n=1$, which corresponds to the case where there is no shell

$$\frac{3}{2}\sum_{n=0}^{\infty} n(n+1)(2n+1)\left[\frac{j_n(kr_0)}{kr_0}\right]^2 = 1. \quad (36)$$

At the same time the antenna reactance (actually the reactance increase) may be shown expressible by

$$\frac{X_A}{R_{11}} = \frac{3}{2}\sum_{n=0}^{\infty} n(n+1)(2n+1)\,|R_n|^2\left[\frac{j_n(kr_0)}{kr_0}\right]^2(\kappa_e-1)kd \cdot \left\{\left[\frac{d[kr_1 j_n(kr_1)]}{d(kr_1)}\right]^2\left[(\kappa_e-1)kd\frac{d[kr_1 j_n(kr_1)]}{d(kr_1)}\frac{d[kr_1 n_n(kr_1)]}{d(kr_1)} - 1\right] + \left[\frac{d[kr_1 n_n(kr_1)]}{d(kr_1)}\right]^2\left[(\kappa_e-1)kd\frac{d[kr_1 j_n(kr_1)]}{d(kr_1)}\frac{d[kr_1 n_n(kr_1)]}{d(kr_1)} + 1\right]\right\} \quad (37)$$

where n_n is the spherical Neumann function.[3] R_A/R_{11} and X_A/R_{11} have been made the object of numerical computations, the results of which are presented in Fig. 3. The computations have been made for a shell, the electrical thickness of which is determined by $(\kappa_e-1)kd=0.779$. The thinner the shell, the nearer the relative radiation resistance and increase of reactance of the dipole are to 1 and 0, respectively. The shell is seen to influence the dipole impedance strongly as the dipole is placed near the center of the spherical shell. By placing the dipole more than half a wavelength from the center of the shell but not too close to the shell, the vswr on the line feeding the dipole is seen to be less than 1.2, while a vswr of about 2.2 is obtained by placing the dipole at the center of the shell. By the way, only the term $n=1$ of (32) and (37) contributes to the impedance of the centered dipole, the dipole resistance thus being $R_A/R_{11}=|R_1|^2$.

Conclusion

The numerical results obtained for the gain and impedance of a radial dipole surrounded by a dielectric spherical shell seem to show that a compromise is necessary as to the position of the dipole inside the shell in order to obtain a small influence of the shell on the gain as well as on the impedance of the dipole. The numerical results are also expected to be practically applicable to a dipole of finite length.

Acknowledgment

This investigation was carried out in the Institute of Electromagnetic Theory at the Technical University of Denmark by means of a grant from Civilingeniør A. R. Angelos Legat. I wish to express my thanks to Professor H. Lottrup Knudsen for having suggested this investigation. The English translation of the paper was revised by Oscar Kasch, sworn translator and interpreter.

The Current Distribution and Input Impedance of Cylindrical Antennas*

E. V. BOHN†

Summary—**This paper treats both the formulation of the problem and its solution in a fundamental way permitting only approximations which appear evident. A system of four integro-differential equations is derived and these are applied to the cylindrical antenna problem. An integral equation of Hallen's type occurs and this is solved exactly by transform methods. The input impedance of a full wave antenna is computed numerically to show that the present theory is consistent with other results.**

Introduction

THE cylindrical antenna problem is fundamental in antenna theory and considerable effort has been devoted to its solution. For moderately thick antennas the integral equation approach is the most suitable, but it has not been fully exploited due to the mathematical difficulties involved. Hallen's[1] method of iteration gives asymptotic results only and is dependent on an arbitrary choice of expansion parameter. It restricts itself to asymptotically thin antennas with a discontinuous ring driving source and is inconsistent in that it obtains a finite input impedance. It does not give a clear distinction between the cylindrical antenna and the cylindrical cavity and it is incapable of computing the free modes of oscillation of the antenna.

In order to obtain a solution which satisfactorily overcomes these objections, a more fundamental approach must be made to the problem. Infeld[2] has shown the importance of the gap in determining input impedance. However, his method is not suited to the cylindrical antenna. Synge[3] has formulated an exact integral equation for the problem which is then solved by iterative methods. This is basically Hallen's original method of splitting the kernel into a singular and a finite part and has been sufficiently criticized in the past to indicate the necessity of a more fundamental approach. In the interest of simplicity we restrict ourselves to perfectly conducting closed surfaces and introduce the following notation:

$\psi = \dfrac{e^{-j\beta r}}{r}$

i = surface current density

$\vec{A}$ = vector pot.

$\vec{T}$ = unit vector in the direction of current flow

U = scalar pot.

$r^2 = (x-x')^2 + (y-y')^2 + (z-z')^2$

$\vec{N}$ = unit vector normal to the surface and directed so that $\vec{H} = i\vec{T} > \vec{N}$

q = surface charge density

$\nabla = \dfrac{\partial}{\partial x}, \dfrac{\partial}{\partial y}, \dfrac{\partial}{\partial z}$ = gradient with respect to the point of integration x, y, z

$\nabla' = \dfrac{\partial}{\partial x'}, \dfrac{\partial}{\partial y'}, \dfrac{\partial}{\partial z'}$ = gradient with respect to the field point $x', y', z' = u$

E_i = tangential electric field of the generator.

The $\vec{E}$ and $\vec{H}$ fields are determined by the following:

$$\vec{H}(\rho') = \frac{1}{4\pi}\int \vec{i} x \nabla\psi ds \tag{1}$$

$$\vec{E}(\rho') = -j\omega\vec{A} + \nabla U. \tag{2}$$

To arrive at the fundamental antenna equations, we let ρ' approach a point on the surface. Taking into account the singularities in the integrals and the boundary conditions, it is a simple matter to derive the following:

$$\vec{i} \times \vec{N}(\rho') = \frac{1}{2\pi}\int \vec{i} \times \nabla\psi ds \tag{1a}$$

$$\vec{E}\cdot\vec{N} = \frac{q}{\varepsilon_0} \tag{2a}$$

$$-\vec{E}\cdot\vec{T} = E_i \tag{3}$$

where

$$\vec{E}(\rho') = -j\omega\vec{A}(\rho') + \frac{1}{4\pi}\int \frac{q}{\varepsilon_0}\nabla\psi ds + \frac{1}{2}\frac{q}{\varepsilon_0}\vec{N}(\rho')$$

$$\operatorname{div}\vec{i} = -j\omega q. \tag{4}$$

This is a system of four integro-differential equations for the four unknows, i, q, and the two surface components of $\vec{T}$. The antenna problem distinguishes itself from the cavity problem in the choice of $\vec{N}$ which is directed toward the field. The antenna $\vec{N}$ is directed outward. A general discussion of this system appears out of the question, but if we restrict ourselves to the cylindrical antenna the equations are considerably sim-

* Manuscript received by the PGAP, July 9, 1956.

† Canadian Aviation Electronics, Montreal, P. Q., Canada.

[1] For a thorough discussion of this problem and literature references, see S. A. Schelkunoff, "Advanced Antenna Theory."

[2] L. Infeld, "The influence of the width of the gap upon the theory of antennas," *Quart. Appl. Math.*, vol. 5; July, 1947.

[3] G. E. Albert and J. L. Synge, "The general problem of antenna radiation and the fundamental integral equation with application to an antenna of revolution," *Quart. Appl. Math.*, pt. 1, vol. 6. See also, J. L. Synge, pt. 2.

plified. We consider a completely closed cylindrical antenna (Fig. 1). Instead of applying the group [(1a), (2a), (3), and (4)] to this case it is simpler to start with a slightly modified but equivalent group of equations. For the cylindrical portion of the antenna we have

$$-j\omega\mu_0 i = -\frac{\partial E_z}{\partial \rho} + \frac{\partial E_\rho}{\partial z} \tag{1b}$$

$$\varepsilon_0 E_\rho = q \tag{2b}$$

$$\frac{di}{dz} = -j\omega q. \tag{4a}$$

The first of these equations is equivalent to (1a) in that it is obtained from the boundary conditions for $\vec{H}$. We set

$$2\pi a i = I \qquad 2\pi a q = Q$$

and obtain

$$\frac{d^2 I}{dz^2} + \beta^2 I = -2\pi a j\omega\varepsilon_0 \frac{\partial E_z}{\partial \rho} \tag{5}$$

$$I(z) = C_1 \sin\beta(l - z + \theta) + \frac{2\pi j\omega\varepsilon_0}{\beta}\int_z^l \left(a\frac{\partial E_z}{\partial \rho}\right) \cdot \sin\beta(z - u)du. \tag{6}$$

Eq. (3) is

$$-E_i = -j\omega\frac{\mu_0}{4\pi}\int_A i\psi ds + \frac{1}{4\pi\varepsilon_0}\int_{A+C} q\frac{\partial\psi}{\partial z}ds.$$

A refers to the cylindrical portion of the antenna and C to the end caps. We now restrict ourselves to a center-fed antenna so that $Q(+l) = -Q(-l)$ and assume the charge to be continuous. Partial integration and use of (4a) and (5) gives us

$$E_i + \frac{Q(l)}{4\pi\varepsilon_0}F_1 = \frac{1}{4\pi}\int_0^{2\pi}\int_{-l}^{+l}\left(a\frac{\partial E_z}{\partial \delta}\right)\psi dz d\phi \tag{7}$$

where

$$F_1 = \frac{1}{2\pi}\int_0^{2\pi}\{\psi(|l-u|) + \psi(|l+u|)\}d\phi - \frac{a}{4\pi}\frac{\partial}{\partial u}\int_0^{2\pi}\{\psi(|l-u|) - \psi(|l+u|)\}d\phi.$$

In F_1 we have taken $q = q(+l)$ over the cap and also ψ to be constant for a fixed value of u.

We now set

$$a\frac{\partial E_z}{\partial \rho} = y + y' + y''$$

and consider (7) to be an integral equation for the y's.

$y'(z)$ has an impulse type singularity at $z = \pm l$;
$y''(z)$ has a doublet type singularity at $z = \pm l$.

These functions are defined by

$$\int_{-l}^{+l} y'(z)f(z-u)dz = \frac{Q}{2\pi\varepsilon_0}\{f(l-u) + f(-l-u)\}$$

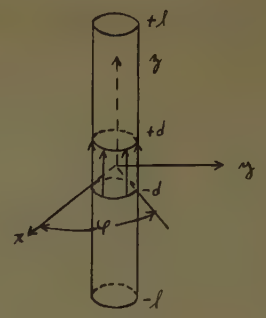

Fig. 1.

$$\int_{-l}^{+l} y''(z)f(z-u)dz = -\frac{Qa}{4\pi\varepsilon_0}\times\frac{\partial}{\partial u}\{f(l-u) - f(-l-u)\}.$$

To determine y we have the integral

$$E_i(u) = \frac{V}{2d}g(u) = \frac{1}{4\pi}\int_0^{2\pi}\int_{-l}^{+l} y(z)\psi(|z-u|)dz d\phi \tag{8}$$

where

$$r^2 = (z-u)^2 + 2a^2(1-\cos\phi)$$

and V is the "driving voltage." From (6) we have

$$I(z) = C_1\sin\beta(l - z + \theta) - j\frac{\omega Q}{\beta}\sin\beta(l-z) - j\omega Q\frac{a}{2}\cos\beta(l-z) + \frac{2\pi j\omega\varepsilon_0}{\beta}\int_z^l y(u)\sin\beta(z-u)du.$$

Over the end caps C of the antenna we have

$$\frac{1}{\rho}\frac{\partial}{\partial\rho}(\rho I_1(\rho)) = -j\omega Q(+l).$$

We set $I_1(\rho) = -B\rho$ and find $B = j\omega Q/2$. To determine C_1 and θ we have

$$I(+l) = I_1(a) = \frac{j\omega Q}{2}a; \qquad \left(\frac{\partial I}{\partial z}\right)z = +l = j\omega Q.$$

Neglecting higher powers in a, this leads to

$$C_1 = \frac{2j\omega Q}{\beta}; \qquad \theta = \frac{a}{2}$$

$$I(z) = I_0\sin\beta\left(l - z + \frac{a}{2}\right) + \frac{2\pi j\omega\varepsilon_0}{\beta}\int_z^l y(u)\sin\beta(z-u)du \quad (z>0) \tag{9}$$

where

$$I_0 = \frac{j\omega Q(+l)}{\beta}.$$

Eq. (9) is correct provided y contains no further singularities. The problem is now to solve (8) for y and then to obtain I from (9). The manner in which I_0 is

determined will be discussed later. We now turn to the solution of the integral (8). To obtain a solution we begin with the following relation:[4]

$$\psi = \frac{e^{-j\beta r}}{r} = \frac{1}{j\pi}\int_C K_0(\rho\sqrt{-\beta^2 - s^2})e^{s(u-z)}ds$$

$$r^2 = (z-u)^2 + \rho^2$$

$$\rho^2 = 2a^2(1-\cos\phi).$$

We substitute $S = S/l$ and obtain

$$\frac{e^{-j\beta r}}{r} = \frac{1}{j\pi l}\int_C K_0\left(\frac{\rho}{l}\sqrt{-\beta^2 l^2 - \delta^2}\right)e^{s/l(u-z)}ds.$$

We have[5]

$$\frac{1}{2\pi}\int_0^{2\pi} K_0\left(\frac{\rho}{l}\sqrt{-\beta^2 l^2 - s^2}\right)d\phi$$

$$= K_0\left(\frac{a}{l}\sqrt{-\beta^2 l^2 - s^2}\right)I_0\left(\frac{a}{l}\sqrt{-\beta^2 l^2 - s^2}\right)$$

$$= K_0 I_0[s].$$

$I_0(z)$ represents a Bessel function and should not be confused with the current amplitude I_0.

Hence

$$\frac{1}{2\pi}\int_0^{2\pi}\psi d\phi = \frac{1}{j\pi l}\int_C K_0 I_0[s]e^{s/l(u-z)}ds$$

$$= \sum_{n,m} k(t,p)e^{-tz/l}e^{pu/l} \qquad \begin{cases} t = j\pi m \\ p = j\pi n \end{cases} \qquad (10)$$

where

$$k(t,p) = k_{nm} = \frac{1}{j\pi l}\int_C K_0 I_0[s]\cdot\frac{\sinh(s-p)}{s-p}\cdot\frac{\sinh(s-t)}{s-t}ds. \qquad (11)$$

The integral equation is now reduced to a system of linear equations:

$$\frac{V}{2d}g_n = \sum_m lk_{nm}y_m \qquad (12)$$

where

$$y_m = \frac{1}{2l}\int_{-l}^{+l} ye^{-j(\pi mz/l)}dz.$$

Fig. 2 illustrates the path c and the two branch cuts W_1 and W_2 to the branch points $\pm j\beta l$. To evaluate (11), we take p and t to the left of c and break up the integrand into two parts. One part can be evaluated by deforming c into W_2; the second part can be evaluated by deforming c into W_1 and two integrals around the poles p and t which can be readily evaluated. The integral along the branch cut W_1 can then be transformed into an integral along W_2. The result of this operation is the following expression.

[4] See S. A. Schelkunoff, "Electromagnetic Waves," p. 414.
[5] See Watson, "Theory of Bessel Functions," p. 360.

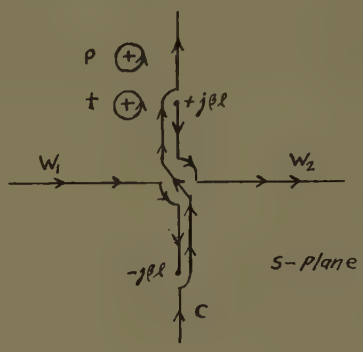

Fig. 2.

$$lk(t,p) = \frac{1}{4}\int_W J_0 I_0[s]\left\{\frac{e^{-2s+p+t} - \cosh(p-t)}{(s-p)(s-t)} + \frac{e^{-2s-p-t} - \cosh(p-t)}{(s+p)(s+t)}\right\}ds + \frac{1}{2}\frac{\sinh(p-t)}{p-t}\{K_0 I_0[t] + K_0 I_0[p]\}.$$

For $J_0 I_0$ we have the expansion

$$J_0 I_0[s] = 1 - \frac{1}{32}\left(\frac{a}{l}\right)^4(\beta^2 l^2 + s^2) + \cdots.$$

Hence we can set $J_0 I_0[s] \approx 1$ in the integrand for the lower order matrix elements. The integrals can then be reduced to the familiar sin-cos integrals by suitably choosing W_2. The results are given in the Appendix.

Since

$$\frac{\sinh(p-t)}{p-t} = \begin{cases} 1 & p = t \\ 0 & p \neq t \end{cases}$$

we have the result that the lower order of diagonal elements are nearly independent of a and the diagonal elements have a logarithmic singularity in a. Hence asymptotically as $a \to 0$ the diagonal elements become very large and this leads to the following approximate solution of (12)

$$lk_{nn}y_n = \frac{V}{2d}\left\{g_n - \sum_{m,m\neq n}\frac{lk_{nn}}{lk_{mn}}g_m\right\}. \qquad (12a)$$

The infinite system of linear (12) reflects the properties of the integral (8). We can now obtain a clearer insight into Hallen's method of iteration. Hallen's method in effect attempts to compute all the matrix elements by means of (12a). Only the lower order diagonal elements are dominant due to the logarithmic singularity of K_0 at the origin. Hence we can apply the iterative solution (12a) to the lower order elements only. This is the fundamental reason for the asymptotic divergent character of Hallen's solution.

Having solved (8) we can substitute y into (9) and obtain for the current the following expression

$$I(z) = I_0\sin\beta\left(l - z + \frac{a}{2}\right) + V\cdot f_1(z). \qquad (13)$$

f_1 is now a known function but the relationship between I_0 and V is still to be determined. To obtain this, we can derive the following result

$$E_z = -\frac{1}{4\pi}\int_0^{2\pi}\int_{-l}^{+l} y(z)\psi(|z-u|)\,dz\,d\phi$$

where

$$r^2 = (z-u)^2 + a^2 + \rho^2 - 2a\rho\cos\phi$$

in the same manner as we did (8).

For $u=0$ and $\rho\to\infty$ we must have

$$\frac{E_z}{H_\phi} = n = 120\pi = \frac{-\int_0^l y(z)\,dz}{\frac{j\beta}{2\pi}\int_0^l I(z)\,dz}. \qquad (14)$$

This leads to

$$\left(-\frac{4l}{V}y_0 + \frac{2l}{V}y_1\right) = \frac{240}{V}jI_0. \qquad (14a)$$

The Case of the Sinusoidal Current Distribution

If we imagine V fixed and let $a\to 0$, we see from (12a) and (14a) that, in general, I_0 is of the same order as f_1. Hence as $a\to 0$, $f_1(z)\to 0$, $I_0\to 0$, but the sinusoidal term does not necessarily become dominant in the limit. Since the sinusoidal current distribution has played such a successful role in antenna theory, it is of interest to see under what circumstances I_0 will become dominant over f_1. As $a\to 0$, we can solve (12) asymptotically and obtain

$$lK_0(\beta a)y_n = \frac{V}{2d}g_n; \qquad y = \frac{E_j(u)}{lK_0(\beta a)}.$$

Hence

$$I(z) = I_0\sin\beta\left(l - z + \frac{a}{2}\right) + \frac{jV}{120lK_0(\beta a)}\cdot\sin\beta(d-z) \qquad z>0$$

where we have taken

$$g(u) = \begin{cases} 1 & |u| < d \\ 0 & |u| > d \end{cases} \qquad d \ll l$$

and

$$\sin\beta(d-z) = 0, \qquad z > d.$$

Since

$$I_0 \text{ and } \frac{V}{120lK_0(\beta a)}$$

are of the same order, the condition that the sinusoidal term dominates is that $d\to 0$. The sufficient conditions for a sinusoidal current distribution are that $a\to 0$ and that $d\to 0$. Actual practical antennas approximately meet these conditions.

From the theory of equations of type (8) and (12) it can be seen that we must choose a fixed $d>0$. If we attempt to choose $d=0$, (12) becomes invalid since $\sum|g_n|^2=\infty$. The input current is infinite under this condition.

The sinusoidal current distribution is also very successful in the computation of antenna impedances. This is all the more surprising because of the very great discrepancies in the tangential electric fields of the sinusoidal and the actual current distributions. To obtain a more fundamental understanding of this situation, we derive the following:

$$p_2 - p_1 = j\omega\mu_0\int|\vec{H}_2-\vec{H}_1|^2d\tau - j\omega\varepsilon_0\int|\vec{E}_2-\vec{E}_1|^2d\tau + n\int|\vec{E}_2-\vec{E}_1|^2ds + \int\vec{E}_1\cdot(\vec{i}_1^{\,*}-\vec{i}_2^{\,*})d\tau. \qquad (15)$$

p is the complex power of the electromagnetic field and the indices refer to two different field distributions. Eq. (15) can be easily proven by the use of the reciprocity theorem and the usual vector identities.

We can now state the following minimum theorem: if $\vec{i}_1$ is the correct current distribution meeting the boundary conditions and if $\vec{i}_2$ is a second current distribution such that $\vec{i}_1=\vec{i}_2$ over the generator region, then the correct current distribution requires the least real power.

The condition that the input current be held constant is approximately fulfilled in the case of a concentrated generator and provided that $\sin\beta l\neq 0$. This minimum theorem is the reason why the sinusoidal current distribution can be successfully applied in computing the radiation resistance.

Free Modes of Oscillation

These are defined by setting $g_n=0$ in (12). The eigenvalues are obtained from $\|k_{nm}(\beta)\|=0$. Due to the asymptotic behavior of the diagonal matrix elements, the problem of solving for the eigenvalues may not be so formidable as it first appears. This would be of importance in the study of the transient behavior of antennas.

Numerical Results for a Full Wave Antenna

We take

$$\beta l = \pi \qquad \frac{l}{2a} = 37.1 \qquad \frac{d}{a} = 5$$

$$g(u) = \begin{cases} 1 & |u| < d \\ 0 & |u| > d. \end{cases} \qquad (16)$$

The arbitrary choice of d brings out a fundamental weakness in present antenna theory. E_i is determined by the terminal driving conditions from a coax cable or transmission line and can not be arbitrarily chosen. The only known property of E_i is that it is "concentrated" near the driving point. Without further infor-

mation about E_i there is no purpose in taking all the Fourier coefficients of (16) in the calculation. We therefore compute y_n from $g_n(n=0, 1, \cdots, 5)$ and set $y_n=0(n=6, 7, \cdots,)$. This simplifies the numerical work and still leads to a field which is "concentrated." From (12a) we now obtain

$$\frac{2l}{V}y_0 = 0.2615 + j0.1458$$

$$\frac{2l}{V}y_1 = 0.2870 + j0.0679$$

$$\frac{2l}{V}y_2 = 0.3812 - j0.0098$$

$$\frac{2l}{V}y_3 = 0.4050 + j0.0070$$

$$\frac{2l}{V}y_4 = 0.4573 - j0.0052$$

$$\frac{2l}{V}y_5 = 0.4698 - j0.0036.$$

For the function f_1 in (13) we have

$$Vf_1(z) = j\frac{V}{60}\left[\frac{f(z)}{V}\right]$$

$$\frac{f(z)}{V} = -\frac{1}{\pi}(0.0433 + j0.0773)\cos\frac{\pi z}{l} - \frac{1}{2\pi}\left(\frac{2l}{V}y_0\right) + \left(\frac{ly_1}{V}\right)\left(1 - \frac{z}{l}\right)\sin\frac{\pi z}{l} + \frac{1}{\pi}\sum_{n=2}^{5}\left(\frac{2l}{V}y_n\right)\frac{\cos\frac{\pi nz}{l}}{n^2-1}.$$

From (14a) we get

$$240\frac{I_0}{V} = 0.2237 + j0.2360.$$

For the complex power we have

$$p = \int_0^l E_i I^* dz = \tfrac{1}{2}Y_i\left|V\right|^2 = \tfrac{1}{2}Z_0\left|I_0\right|^2.$$

Y_i is the input admittance and Z_0 is the loop impedance based on the sinusoidal current. We find

$$Z_i = \frac{1}{Y_i} = 730 - j570; \qquad Z_0 = 464 - j362.$$

The loop impedance calculated from the field of a sinusoidal current alone is $Z_0=200+j120$.

Since the input current is not even approximately constant, we can not expect the minimum theorem to be applicable here. From Schelkunoff[6] we have

$$Z_i = 850 - j660.$$

[6] S. A. Schelkunoff, "Antenna Theory and Practice," p. 439.

The result (17) is seen to be consistent with other results. An accurate comparison between the various theories and experimental results is not possible due to the lack of knowledge concerning E_i.

Conclusion

The method of solving the cylindrical antenna problem by the use of Fourier coefficients is superior to Hallen's iterative procedure both theoretically and numerically. Improved solutions by Hallen's method would require graphical analysis, while the solution of (12) by arithmetic means involves no theoretical difficulty. The one objection to (12)—that a large number of terms may be required—cannot be answered until there is more detailed knowledge of E_i. Asymptotically as $a\to 0$ (12) can be just as readily solved for an impulse type of solution (requiring an infinite number of terms) as the integral (8) directly. The complex power and the input impedance can be computed exactly without graphical analysis as it would have to be done by Hallen's method. The various theories give comparable results because each uses a "concentrated" type of field.

Appendix

Matrix Elements for $1/2\pi\int_0^{2\pi}\psi d\phi$

$k_{n,m}$ is symmetrical about both diagonals

$$\begin{cases} k_{n,-m} = k_{m,-n} \\ k_{n,m} = k_{m,n} \end{cases} \qquad (n \neq m).$$

We use the short hand notation

$$K_0I_0[s] = K_0\left(\frac{a}{l}\sqrt{-\beta^2l^2 - s^2}\right)I_0\left(\frac{a}{l}\sqrt{-\beta^2l^2 - s^2}\right)$$

where I_0 and K_0 are the modified Bessel functions of the first and second kind, respectively.

$$\left.\begin{matrix} \pi n > \beta l \\ \pi m > \beta l \end{matrix}\right\} \quad n \neq m \qquad (18)$$

$$4\pi j(n-m)(-1)^{n+m}lk_{nm} = \ln\frac{(\pi n - \beta l)(\pi m + \beta l)}{(\pi m - \beta l)(\pi n + \beta l)} - \mathrm{Ci}\,2(\pi n - \beta l) + \mathrm{Ci}\,2(\pi m - \beta l) + \mathrm{Ci}\,2(\pi n + \beta l) - \mathrm{Ci}\,2(\pi m + \beta l) + j\{-\mathrm{Si}\,2(\pi n - \beta l) + \mathrm{Si}\,2(\pi m - \beta l) - \mathrm{Si}\,2(\pi n + \beta l) + \mathrm{Si}\,2(\pi m + \beta l)\}$$

$$\left.\begin{matrix} \pi n < \beta l \\ \pi m > \beta l \end{matrix}\right\} \quad n \neq m \qquad (19)$$

$$4\pi j(n-m)(-1)^{n+m}lk_{nm} = \ln\frac{(\beta l - \pi n)(\pi m + \beta l)}{(\pi m - \beta l)(\pi n + \beta l)} - \mathrm{Ci}\,2(\beta l - \pi n) + \mathrm{Ci}\,2(\pi m - \beta l) + \mathrm{Ci}\,2(\beta l + \pi n) - \mathrm{Ci}\,2(\beta l + \pi m) + j\{\mathrm{Si}\,2(\beta l - \pi n) + \mathrm{Si}\,2(\pi m - \beta l) - \mathrm{Si}\,2(\beta l + \pi n) + \mathrm{Si}\,2(\beta l + \pi m)\}$$

$$\pi n > \beta l \qquad (n = m) \qquad (20)$$

$$lk_{nn} = K_0 I_0[j\pi n] + \frac{e^{-2j\beta l} - 1}{4j}\left\{\frac{1}{\beta l + \pi n} + \frac{1}{\beta l - \pi n}\right\} + \frac{1}{2}\,\mathrm{Ci}\,2(\pi n + \beta l) + \frac{1}{2}\,\mathrm{Ci}\,2(\pi n - \beta l) + \frac{j}{2}\left\{\mathrm{Si}\,2(\pi n - \beta l) - \mathrm{Si}\,2(\pi n + \beta l)\right\}$$

$$\pi n < \beta l \qquad (n = m) \tag{21}$$

$$lk_{nn} = K_0 I_0[j\pi n] + \frac{e^{-2j\beta l} - 1}{4j}\left\{\frac{1}{\beta l + \pi n} + \frac{1}{\beta l - \pi n}\right\} + \frac{1}{2}\,\mathrm{Ci}\,2(\pi n + \beta l) + \frac{1}{2}\,\mathrm{Ci}\,2(\beta l - \pi n) + \frac{j}{2}\left\{\pi - \mathrm{Si}\,2(\beta l + \pi n) - \mathrm{Si}\,2(\beta l - \pi n)\right\}.$$

For $\beta l = \pi$ and $n, m = \pm 1$ we have

$$n > 1 \tag{22}$$

$$4\pi j(n-1)(-1)^{n+1} lk_{n1} = \ln 2\pi\frac{(n-1)}{(n+1)} + C + \ln 2 - \mathrm{Ci}\,2\pi(n-1) + \mathrm{Ci}\,2\pi(n+1) - \mathrm{Ci}\,4\pi + j\left\{-\mathrm{Si}\,2\pi(n-1) - \mathrm{Si}\,2\pi(n+1) + \mathrm{Si}\,4\pi\right\}$$

$$m > 1 \tag{23}$$

$$-4\pi j(m+1)(-1)^{m-1} lk_{-1,m} = \ln 2\pi\frac{(m+1)}{(m-1)} - \mathrm{Ci}\,4\pi + \mathrm{Ci}\,2\pi(m-1) + C + \ln 2 - \mathrm{Ci}\,2\pi(m+1) + j\left\{-2\pi + \mathrm{Si}\,4\pi + \mathrm{Si}\,2\pi(m-1) + \mathrm{Si}\,2\pi(m+1)\right\}$$

$$lk_{11} = -\frac{1}{2}\ln 2\pi - \ln\frac{a}{l} + \frac{3}{2}\ln 2 - \frac{1}{2}(C+1) + \frac{1}{2}\,\mathrm{Ci}\,4\pi - \frac{j}{2}\,\mathrm{Si}\,4\pi \tag{24}$$

$$4\pi j lk_{01} = \ln 2\pi + C + \ln 2 - \mathrm{Ci}\,4\pi + j\,\mathrm{Si}\,4\pi \tag{25}$$

$$-4\pi j lk_{1,-1} = \ln 2\pi + C + \ln 2 - \mathrm{Ci}\,4\pi + j[-\pi + \mathrm{Si}\,4\pi]. \tag{26}$$

Scanning Lens Design for Minimum Mean-Square Phase Error*

E. K. PROCTOR† AND M. H. REES‡

Summary—**Microwave lenses of the constraining or binormal type having superior wide-angle scanning properties can be achieved by suitable choices of lens contours and of the manner in which the index of refraction varies from point to point across the aperture plane. The phase error (*i.e.*, departure from a plane phase front at the exit surface of the lens) can be expressed in terms of three unknown functions: the equations of the two lens surfaces and of the index of refraction. The square of this error is integrated over the desired angle of scan and also over the aperture area of the lens. The three unknown functions which minimize the phase-error integral are then determined from the Euler-Lagrange equations of the calculus of variations. Graphs of phase errors for several typical lens designs are included.**

Introduction

MICROWAVE lenses in which metallic plates are used in such a manner as to constrain the internal wave propagation to directions parallel to the lens axis have been called "constraining" or "binormal" lenses. Snell's Law is not obeyed at the surfaces of such lenses and the refractive properties are described most conveniently in terms of the differential phase shifts imparted along various ray paths through the lens. Since these phase shifts are independent of the angles of incidence (neglecting surface-impedance effects), constraining lenses have inherent advantages in scanning antenna systems.

Ruze[1] in 1950, and Ellis, Fine, and Reynolds[2] in 1951, have reported analytical and experimental work on such lenses. A brief summary of the Ruze method of analysis is in order here by way of introduction to the analytical method of this paper.

The geometry and notation for what will be called a "two-dimensional" lens are shown in Fig. 1. It is assumed that the lens is so constructed that ray paths within the lens are parallel to the x axis for all incident and emergent rays. The lens is illuminated by a suitable point source which can move along a circular feed path to cause the emergent beam to scan through a total angle of $2\theta_1°$. The feed circle is centered at the origin

* Manuscript received by the PGAP, August 22, 1956. This paper (less the Appendixes) was presented at the WESCON Convention, Los Angeles, Calif., August 21–24, 1956. Work based on a study program carried out by Sperry Gyroscope Co., under Contract DA 36-039-sc-15323 for the Evans Signal Lab., of the U. S. Signal Corps.

† General Electric Microwave Lab., Palo Alto, Calif. Formerly with Sperry Gyroscope Co., Great Neck, N. Y.

‡ University of Colorado, Boulder, Colo. Formerly with Sperry Gyroscope Co., Great Neck, N.Y.

[1] J. Ruze, "Wide-angle metal-plate optics," PROC. IRE, vol. 38, pp. 53–59; January, 1950.

[2] Ellis, Fine, and Reynolds, "A Point Source Binormal Lens," Air Force Cambridge Res. Labs., Rep. No. E5067; March, 1951.

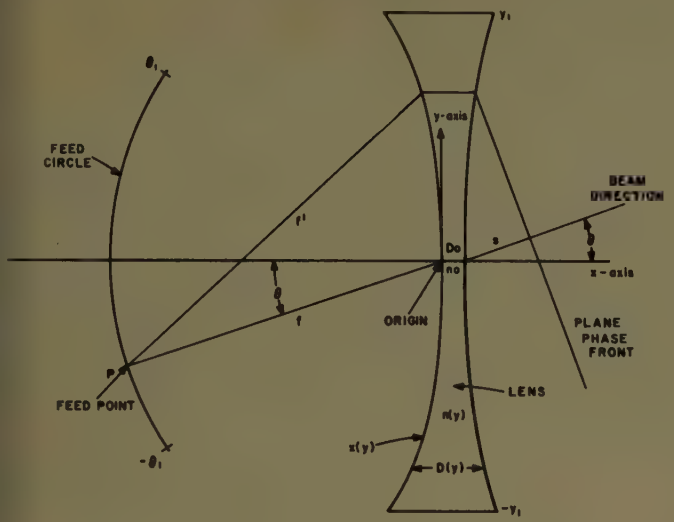

Fig. 1—Schematic diagram for scanning lens.

and has a radius equal to the focal length, f. The aperture or width of the lens is $2y_1$ and its center thickness is D_0. The lens is to be designed to convert the incident circular phase front from the point-source feed into a plane emergent phase front. The equations of the illuminated surface, $x(y)$, the lens thickness, $D(y)$, and the index of refraction for any ray path through the lens, $n(y)$, are to be determined. These three equations are independent and may be considered as design parameters which are to be so chosen as to minimize the scanning aberrations of the lens.

Since three independent equations are to be determined, three independent conditions must be specified. In Ruze's method of analysis, two conditions are prescribed by the requirement that perfect focus be obtained at two symmetrical off-axis feed positions. This leads to the explicit requirement that the illuminated surface, $x(y)$, be an ellipse and yields an equation relating $n(y)$ and $D(y)$. For other feed positions, Ruze obtains an expression for the phase or path-length error, δ, and expands it in a power series in the coordinate y. (The power series converges for all feed angles if the focal length-to-aperture ratio is greater than 0.8.) In the power series the coefficients, which are functions of the feed position, θ, and of the lens equations, represent distortions of the phase front. The effects on these coefficients of several choices of the third condition including specification of a third perfect-focus feed position (the triple-correction-point design), are considered in some detail in Ruze's paper.

A more general method of determining the three unknown functions is to choose them so that the phase error is minimized throughout the scan angle, $2\theta_1$, and over the entire lens aperture, $2y_1$. This can be accomplished by using variational methods.

The Variational Solution

Consider two rays originating at an arbitrary point, P, on the feed circle as shown in Fig. 1. One of these is a reference ray passing through the center of the lens. The other passes through the lens at an arbitrary distance, y, from the origin. The path-length difference is given by

$$\delta = f + n_0 D_0 + s - f' - n(y)D(y) \tag{1}$$

in which n_0 and D_0 are the values of $n(y)$ and $D(y)$ at $y=0$ and the other quantities are indicated in the figure. For a perfect plane phase front inclined at an angle θ with respect to the y axis, δ is zero. Hence, it is desirable to make δ as small as possible for all feed positions and for all ray paths.

Using the relations

$$f' = [(f\cos\theta + x)^2 + (f\sin\theta + y)^2]^{1/2} \tag{2}$$

and

$$s = (x + D - D_0)\cos\theta + y\sin\theta, \tag{3}$$

the error term may be expressed as

$$\delta = f - [(f\cos\theta + x)^2 + (f\sin\theta + y)^2]^{1/2} + (n_0 D_0 - nD) + (x - D - D_0)\cos\theta + y\sin\theta \tag{4}$$

or

$$\delta = \delta[x(y),\ D(y),\ n(y),\ \theta,\ y,\ \text{constants}]. \tag{4a}$$

The square of δ may be integrated over the lens aperture dimension, $2y_1$, and over the full scan angle, $2\theta_1$. Thus,

$$\Delta = \int_{-y_1}^{y_1}\int_{-\theta_1}^{\theta_1} \delta^2[x(y),\ D(y),\ n(y),\ \theta,\ y,\ \text{constants}]\,d\theta\,dy \tag{5}$$

is an integral expression which is a measure of the cumulative phase error. In particular, since it comes from a definite integral, Δ is a *number* which has a specific value for each combination of $x(y)$, $D(y)$, and $n(y)$. If three explicit functions can be found such that Δ is minimized, they determine a scanning lens which is optimum in a mean-square sense.

Since the functional dependence of δ^2 on θ is known explicitly from (4), the integration with respect to θ in (5) can be carried out to yield

$$\Delta = \int_{-y_1}^{y_1} G[x(y),\ D(y),\ n(y),\ y,\ \theta_1]\,dy \tag{6}$$

in which

$$G = \int_{-\theta_1}^{\theta_1} \delta^2\,d\theta. \tag{6a}$$

The explicit form of G is given in Appendix I. Solution of (6) for the minimizing functions $x(y)$, $D(y)$, and $n(y)$ is a relatively simple problem in the calculus of variations since the derivatives of the unknown functions are not involved.

[Though the details are more complicated, the logic of the variational method is the same as for ordinary maximum and minimum problems in calculus where the expression to be minimized is differentiated once with respect to each of the independent variables and the

derivatives set equal to zero. In the present case, the variables are the three unknown functions $x(y)$, $D(y)$, $n(y)$ and the procedure is roughly equivalent to setting equal to zero the partial derivatives

$$\frac{\partial \Delta}{\partial x(y)}, \quad \frac{\partial \Delta}{\partial D(y)}, \quad \text{and} \quad \frac{\partial \Delta}{\partial n(y)}.$$

This results in three simultaneous equations from which the unknown functions may be determined. It should be noted that these equations are only necessary conditions for the existence of an extremum which may be a maximum, a minimum, or a point of inflection. The evaluation of sufficiency criteria for the existence of a minimum is a problem of considerable mathematical complexity. In most engineering problems it is usually advisable to rely upon geometric or physical intuition to interpret the results.]

The variational problem represented by (6) is of the type involving several unknown functions of a single independent variable, y. It can be shown that the three equations which must be satisfied are

$$G_D = \frac{\partial G}{\partial D(y)} = 0, \tag{7a}$$

$$G_n = \frac{\partial G}{\partial n(y)} = 0, \tag{7b}$$

and

$$G_x = \frac{\partial G}{\partial x(y)} = 0. \tag{7c}$$

(These equations are derived using somewhat different notations in the works of Courant and Hibert[3] Margenau and Murphy,[4] and Weinstock[5] and several other texts which include chapters on the calculus of variations.) Performing the indicated operations (using the expression for G from Appendix I) yields, after some manipulation,

$$x + D - D_0 = \frac{N - L \sin \theta_1/\theta_1}{\theta_1 + \sin \theta_1 \cos \theta_1 - \dfrac{2 \sin^2 \theta_1}{\theta_1}}, \tag{8a}$$

$$n_0 D_0 - nD = \frac{L}{2\theta_1} - \frac{(x + D - D_0) \sin \theta_1}{\theta_1} - f, \tag{8b}$$

$$\frac{(N - L \sin \theta_1/\theta_1)(L' \sin \theta_1/\theta_1 - N')}{\theta_1 + \sin \theta_1 \cos \theta_1 - \dfrac{2 \sin^2 \theta_1}{\theta_1}} - \frac{LL'}{2\theta_1}$$

$$+ 2f \sin \theta_1 - yM' + 2x\theta_1 = 0. \tag{8c}$$

The expressions L, M, N, and

$$L' = \frac{\partial L}{\partial x}, \quad M' = \frac{\partial N}{\partial x}, \quad \text{and} \quad N' = \frac{\partial N}{\partial x}$$

contain elliptic integrals and are given in Appendixes I and II. Eq. (8c) contains x as the only unknown function, but in a very involved implicit form since x appears in the arguments of the elliptic integrals. However, a graphical solution is possible for specific values of θ_1 and the other constants. To avoid double interpolation in the elliptic integral tables, it is advisable to change the variables to

$$\alpha = \tan^{-1} \frac{y}{x} \tag{9a}$$

and

$$\kappa = \sin^{-1} \sqrt{\frac{4\sqrt{x^2 + y^2}}{f^2 + x^2 + y^2 + 2\sqrt{x^2 + y^2}}}. \tag{9b}$$

These relations are illustrated in Fig. 6. Note that the positive x and y axes are to the right and upward respectively so that $x(y)$ has only negative values. It is also desirable to normalize the dimensions to the focal length, f. The required transformation is carried out in Appendix III.

The values of x for a given range of the independent variable, y, may be substituted into (8a) to obtain the corresponding values of $D(y)$. Since $D(y)$ is given explicitly, graphical solution is not required. It should be noted, however, that the two quantities in the numerator of (8a) differ only in the fourth or fifth decimal place. Thus, an eight- or ten-place table of incomplete elliptic integrals is required.[6] The values of $x(y)$ and $D(y)$ from (8c) and (8a) enable one to find the desired values of $n(y)$ quite readily from (8b).

Numerical Evaluation

Eqs. (8a) through (8c) are not very amenable to interpretation except on a numerical basis. Accordingly, calculations of lens contours, index of refraction, and phase error were performed for two versions of the LMSE (lease mean-square error) lens. Corresponding calculations were carried out for lenses whose design equations are determined by conventional methods in order to have a basis for comparison.

Consider first a lens having a plane illuminated surface, $x(y) \equiv 0$. This will be called a two-parameter lens since only $n(y)$ and $D(y)$ can be varied to optimize the phase error. Such a lens is not especially good for scanning, but it offers the advantage that setting $x(y) \equiv 0$ in

[3] R. Courant and D. Hilbert, "Methods of Mathematical Physics," vol. I, Interscience Publishers, New York, N. Y., chap. IV; 1953.
[4] H. Margenau and G. M. Murphy, "The Mathematics of Physics and Chemistry," D. Van Nostrand Co., Inc., New York, N. Y., chap. 6; 1945.
[5] Weinstock, "Calculus of Variations," McGraw-Hill Book Co., Inc., New York, N. Y.; 1952.

[6] "Table of Complete and Incomplete Elliptic Integrals," reissued from Legendre's "Traité des Fonctions Elliptiques," Paris, 1825; issued by the *Biometrika* Office, University College, London; printed at the Cambridge University Press, 1934.

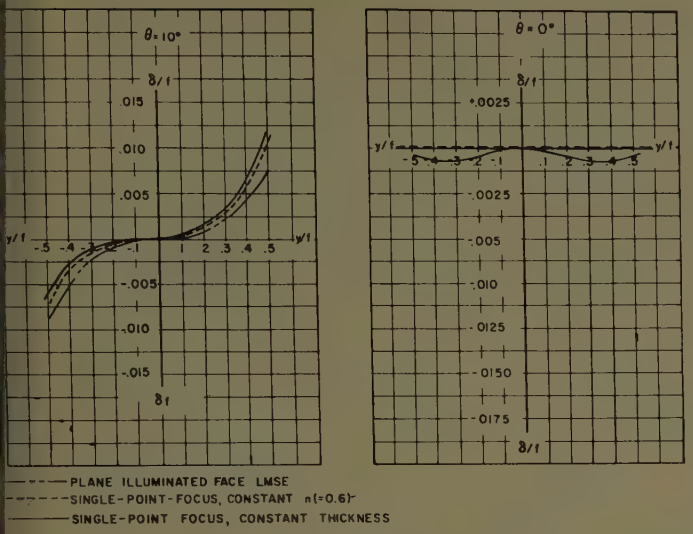

Fig. 2—Phase-error data for two-parameter lens designs.

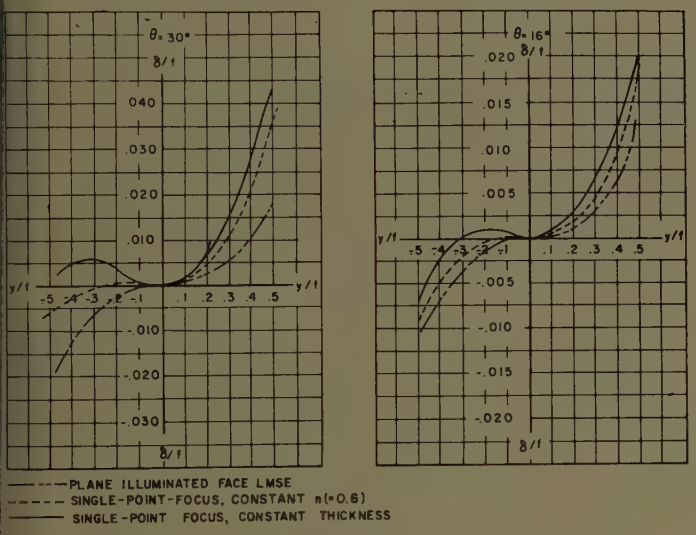

Fig. 3—Phase-error data for two-parameter lens designs.

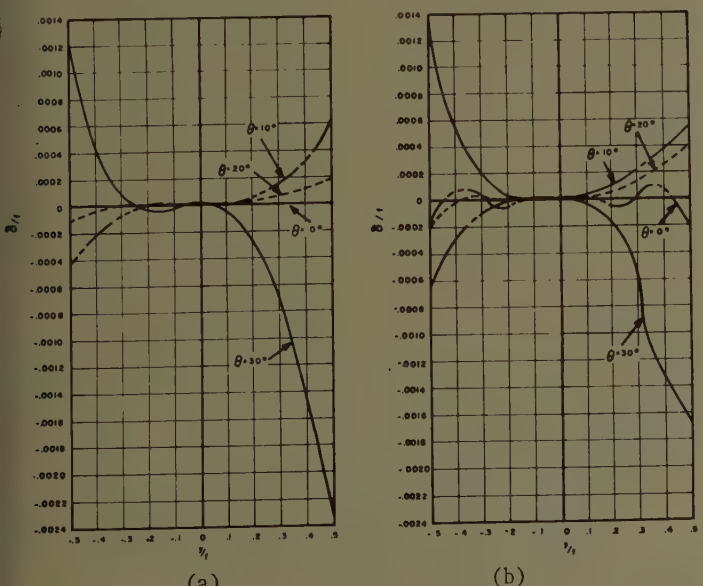

(a) (b)

Fig. 4—(a) Phase error of triple-correction-point lens. (b) phase error of LMSE lens.

the equations eliminates (8c) and considerably simplifies (8a) and (8b). For comparison purposes consider two other lenses having plane illuminated surfaces and designed by the usual methods to give perfect focus at $\theta=0$. One of these has a constant thickness, $D(y)=D_0$, and a varying index of refraction. The other has a constant index of refraction, $n(y)=0.6$, and a varying thickness. For a scan angle of $2\theta_1=60°$ for the LMSE lens, quite reasonable ranges of $n(y)$ and $D(y)$ are obtained. The phase errors of the three lenses for several feed positions are shown in Fig. 2 and Fig. 3. For convenience, both δ and y are normalized to the focal length, f. Values of δ/f are shown only for positive values of θ since the lenses are symmetrical about the x axis. Except for the negligible error at $\theta=0$, it can be seen that for $y>0$ the LMSE design gives the smallest error. For $y<0$ the error of the LMSE lens is greater than for one or the other of the comparison lenses but in a direction which tends to make the error curve symmetrical. This can be interpreted as meaning that the LMSE approach has redistributed the error so as to reduce the peak value. This comparison is not a real test of the effectiveness of the variational approach since the LMSE lens has two parameters, $D(y)$ and $n(y)$, while the comparison lenses have only one each and are not good scanning lenses in any reasonable sense. However, these calculations indicate that the extremum obtained from the Euler equations is certainly not a maximum.

For the three-parameter lens, where $x(y)$, $D(y)$, and $n(y)$ are simultaneously optimized, the obvious comparison lens is the Ruze triple-correction-point design since the feed path is circular in both. To this end the values of $x(y)$, $D(y)$, and $n(y)$ as given by (8) and by the appropriate equations in Ruze's[1] paper were calculated for a total scan angle of $2\theta_1=60°$. The results are shown in Table I and reveal a marked similarity. As might be

TABLE I

Comparison of $x(y)$, $D(y)$, and $n(y)$ for Least Mean-Square Error (LMSE) and Triple-Correction-Point (TCP) Lenses

$\pm y/f$	$-x/f$		$\frac{D-D_0}{f}$		$\frac{nD-n_0D_0}{f}$	
	LMSE	TCP	LMSE	TCP	LMSE	TCP
0	0	0	0	0	0	0
00.171	00.013	00.014	00.028	00.028	00.013	00.014
00.258	00.031	00.031	00.063	00.064	00.029	00.030
00.329	00.052	00.052	00.106	00.104	00.050	00.049
00.477	00.112	00.114	00.216	00.213	00.096	00.093
00.877	00.479	—	00.739	—	—	—

expected, the calculated values of δ/f as shown in Fig. 4 for the two lenses also are nearly identical. It is thus apparent that the variational approach leads to essentially the same lens design as Ruze's power series method. However, the result strongly supports the belief that a true minimum mean-square-phase-error design was obtained. Moreover, the variational method ap-

pears to have no limitations on the focal length-to-aperture ratio.

The "two-dimensional" design equations considered thus far are of doubtful practical value except insofar as they serve to place Ruze's results on a firmer theoretical foundation. The following extension to the three-dimensional case is thought to be somewhat more important.

Extension to Three-Dimensional Case

The method of analysis can easily be extended to the three-dimensional geometry shown in Fig. 5. As before, the feed path is a circle in the xy plane with its center at the origin. The equations to be determined are $x(y, z)$ for the illuminated surface, $D(y, z)$ for the thickness, and $n(y, z)$ for the index of refraction. The path-length difference between an arbitrary ray and the reference ray through the origin is given by

$$\delta = f + n_0 D_0 + s - f' - nD. \tag{10}$$

From the figure,

$$s = (x + D - D_0) \cos\theta + y \sin\theta \tag{11}$$

and

$$f' = [(f\cos\theta + x)^2 + (f\sin\theta + y)^2 + z^2]^{1/2} \tag{12}$$

so that

$$\begin{aligned}\delta &= f - (f^2 + x^2 + y^2 + z^2 + 2fx\cos\theta + 2fy\sin\theta)^{1/2} \\ &\quad + n_0 D_0 - nD + (x + D - D_0)\cos\theta + y\sin\theta \\ &= \delta[x(y, z), n(y, z), D(y, z), y, z, \theta].\end{aligned} \tag{13}$$

The integral to be minimized is

$$\begin{aligned}\Delta &= \int_{-z_1}^{z_1}\int_{-y_1}^{y_1}\int_{-\theta_1}^{\theta_1} \delta^2 d\theta dy dz \\ &= \int_{-z_1}^{z_1}\int_{-y_1}^{y_1} H[x(y, z), D(y, z), n(y, z), y, z, \theta_1] dy dz\end{aligned} \tag{14}$$

in which

$$H = \int_{-\theta_1}^{\theta_1} \delta^2 d\theta. \tag{15}$$

The three unknown functions $x(y, z)$, $n(y, z)$, and $D(y, z)$ can be found by simultaneous solution of

$$\frac{\partial H}{\partial x(y, z)} = 0, \tag{16a}$$

$$\frac{\partial H}{\partial n(y, z)} = 0, \tag{16b}$$

and

$$\frac{\partial H}{\partial D(y, z)} = 0. \tag{16c}$$

Carrying out the indicated operations and rearranging terms lead to a set of equations which may be made identical to (8) by adding terms in z^2 to the arguments and coefficients of the elliptic integrals as shown in Appendix I. Thus, the algebraic form of the original solution is retained. However, graphical solution of (8c) for $x(y, z)$ is considerably more laborious than for the two-dimensional case. It should be noted that in the three-dimensional case none of the equations have rotational symmetry about the x axis since the feed path is a curve, not a surface.

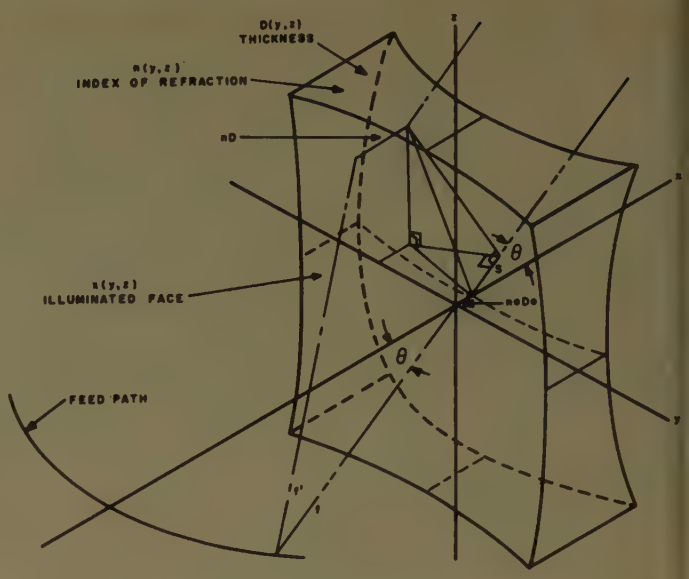

Fig. 5—Three-dimensional lens.

Numerical calculations for the three-dimensional case have not been carried out. However, in view of the similarity of (8) for the two- and three-dimensional cases and the small phase errors indicated by Fig. 4, it seems reasonable to assume that the phase error is, in fact, minimized by the variational method.

Conclusion

In general, the analytical method described in the foregoing is of greater interest than the specific results. In the two-dimensional case Ruze's far simpler equations should be used for design purposes since they apparently lead to the same result. In the three-dimensional case, however, it would probably be impractical to determine an optimum design by means of a power-series analysis. A double series would be required and it is usually quite difficult to evaluate the coefficients and to associate them with the physical system being analyzed.

Certain additional extensions, which the authors considered but lacked time to carry out, should be noted for the benefit of others who might be interested in pursuing the method further.

1) A circular feed path most certainly is not ideal. It should be possible and desirable to carry through a similar analysis with the feed path as a fourth unknown equation to be determined.
2) The numerical similarities between the Ruze triple-correction-point design and the least-mean-square-error design indicate that suitable ap-

proximations would reduce (8) to the Ruze equations in the two-dimensional case.

3) In the three-dimensional case it is possible to write three independent algebraic equations, each of which imposes a requirement for perfect focus at one of three distinct feed points. A triple-correction-point design can be obtained by simultaneous solution of these equations. It is suspected that the resulting equations for $x(y, z)$, $n(y, z)$, and $D(y, z)$ would be easier to work with than (8) and that they would determine a lens which closely approximates the optimum design. Numerical calculations to verify this hypothesis for a few representative cases should prove to be profitable and illuminating.

4) Nonconstraining variable-index-of-refraction materials have recently been developed for microwave lenses. In principle, the path length through such a medium can be expressed as a line integral involving the unknown functions. The expected result of a variational analysis would be a set of simultaneous integral or differential equations for the determination of the unknown functions instead of the algebraic equations obtained for constraining lenses. The mathematics would be much more difficult to carry out, but the resulting optimized nonconstraining scanning lens might have some useful properties.

5) The mathematical solution obtained in this paper implicitly assumes that all phase errors are equally undesirable regardless of their location in the radiating aperture. However, since most lenses have a tapered energy distribution, it might be preferable to modify the phase error by a weighting function related to the distribution of energy over the aperture. This can be accomplished by multiplying the integrands of (5) and (14) by suitably-chosen weighting functions $w(y)$ and $w(y, z)$ respectively. This will not change the method of determining the lens equations but should alter the results considerably.

Appendix I

Evaluation of $G=\int_{-\theta_1}^{\theta_1}\delta^2 d\theta$

Squaring (4) gives

$$\begin{aligned}\delta^2 = &-2(n_0D_0-nD+f)(f^2+x^2+y^2+2fx\cos\theta+2fy\sin\theta)^{1/2}\\ &-2y\sin\theta(f^2+x^2+y^2+2fx\cos\theta+2fy\sin\theta)^{1/2}+y^2\sin^2\theta\\ &-2\cos\theta(x+D-D_0)(f^2+x^2+y^2+2fx\cos\theta+2fy\sin\theta)^{1/2}\\ &+(x+D-D_0)^2\cos^2\theta+2y(x+D-D_0)\sin\theta\cos\theta\\ &+2y\sin\theta(n_0D_0-nD+2f)\\ &+[2(n_0D_0-nD)(x+D-D_0)+2f(2x+D-D_0)]\cos\theta\\ &+(n_0D_0-nD+f)^2+f^2+x^2+y^2. \qquad (17)\end{aligned}$$

Hence,

$$\begin{aligned}G=\int_{-\theta_1}^{\theta_1}\delta^2 d\theta &= A_1\int_{-\theta_1}^{\theta_1}(a+b\cos\theta+c\sin\theta)^{1/2}d\theta\\ &+A_2\int_{-\theta_1}^{\theta_1}(a+b\cos\theta+c\sin\theta)^{1/2}\sin\theta d\theta+A_3\int_{-\theta_1}^{\theta_1}\sin^2\theta d\theta\\ &+A_4\int_{-\theta_1}^{\theta_1}(a+b\cos\theta+c\sin\theta)^{1/2}\cos\theta d\theta+A_5\int_{-\theta_1}^{\theta_1}\cos^2\theta d\theta\\ &+A_6\int_{-\theta_1}^{\theta_1}\sin\theta\cos\theta d\theta+A_7\int_{-\theta_1}^{\theta_1}\sin\theta d\theta\\ &+A_8\int_{-\theta_1}^{\theta_1}\cos\theta d\theta+A_9\int_{-\theta_1}^{\theta_1}d\theta \qquad (18)\end{aligned}$$

where the upper case letters $A_1, A_2, \cdots$, represent constant coefficients and

$$a = f^2 + x^2 + y^2 \qquad (19a)$$

$$b = 2fx \qquad (19b)$$

$$c = 2fy. \qquad (19c)$$

The several integrals, after some manipulation, reduce to the following:

$$\begin{aligned}L &= \int_{-\theta_1}^{\theta_1}(a+b\cos\theta+c\sin\theta)^{1/2}d\theta\\ &= 2\sqrt{a+m}\,[E(\beta, k)-E(-\gamma, k)] \qquad (20)\end{aligned}$$

in which

$$m = 2f\sqrt{x^2+y^2} \qquad (21a)$$

$$\alpha = \tan^{-1}\frac{y}{x} \qquad (21b)$$

$$k = \sqrt{\frac{2m}{a+m}} \qquad (21c)$$

$$\beta = \frac{\theta_1-\alpha}{2} \qquad (21d)$$

$$\gamma = \frac{\theta_1+\alpha}{2} \qquad (21e)$$

and E is the elliptic integral of the second kind.

$$\begin{aligned}M &= \int_{-\theta_1}^{\theta_1}(a+b\cos\theta+c\sin\theta)^{1/2}\sin\theta d\theta\\ &= -\frac{2\cos\alpha}{3m}[(a+m\cos 2\beta)^{3/2}-(a+m\cos 2\gamma)^{3/2}]\\ &\quad+4\sqrt{a+m}\sin\alpha\left\{\left[\frac{1}{3k^2}-\frac{1}{6}\right][E(\beta, k)-E(-\gamma, k)]\right.\\ &\quad+\left[\frac{1}{3}-\frac{1}{3k^2}\right][F(\beta, k)-F(-\gamma, k)]\\ &\quad+\frac{1}{6}\sin 2\beta\sqrt{1-\frac{k^2}{2}(1-\cos 2\beta)}\\ &\quad\left.+\frac{1}{6}\sin 2\gamma\sqrt{1-\frac{k^2}{2}(1-\cos 2\gamma)}\right\} \qquad (22)\end{aligned}$$

in which F is the elliptic integral of the first kind.

$$N = \int_{-\theta_1}^{\theta_1} (a + b\cos\theta + c\sin\theta)^{1/2}\cos\theta d\theta$$
$$= \frac{2\sin\alpha}{3m}[(a + m\cos 2\beta)^{3/2} - (a + m\cos 2\gamma)^{3/2}] + 4\sqrt{a+m}\cos\alpha\left\{\left[\frac{1}{3k^2} - \frac{1}{6}\right][E(\beta, k) - E(-\gamma, k)] + \left[\frac{1}{3} - \frac{1}{3k^2}\right][F(\beta, k) - F(-\gamma, k)] + \frac{1}{6}\sin 2\beta\sqrt{1 - \frac{k^2}{2}(1 - \cos 2\beta)} + \frac{1}{6}\sin 2\gamma\sqrt{1 - \frac{k^2}{2}(1 - \cos 2\gamma)}\right\}. \quad (23)$$

The remaining integrals are simple.

The final expression for G is

$$G = -2L(n_0D_0 - nD + f) - 2yM - 2N(x + D - D_0) + y^2(\theta_1 - \sin\theta_1\cos\theta_1) + (x + D - D_0)^2(\theta_1 + \sin\theta_1\cos\theta_1) + 4\sin\theta_1[(n_0D_0 - nD)(x + D - D_0) + f(2x + D - D_0)] + 2\theta_1[(n_0D_0 - nD + f)^2 + f^2 + x^2 + y^2]. \quad (24)$$

The expression for $H = \int_{-\theta_1}^{\theta_1}\delta^2 d\theta$ in the three-dimensional case is identical to (24) if (19a) is changed to

$$a = f^2 + x^2 + y^2 + z^2, \quad (25)$$

in which case (21c) becomes

$$k = \sqrt{\frac{2m}{a+m}} = \left[\frac{4f\sqrt{x^2+y^2}}{f^2 + x^2 + y^2 + z^2 + 2f\sqrt{x^2+y^2}}\right]^{1/2}. \quad (26)$$

Appendix II

Evaluation of L', M', and N'

Using the expressions for L, M, and N from Appendix I, one obtains

$$\frac{\partial L}{\partial x} = L' = \frac{x(f + \sqrt{x^2+y^2})}{x^2+y^2}[E(\gamma, k) - E(-\beta, k)] - \frac{x(f - \sqrt{x^2+y^2})}{x^2+y^2}[F(\gamma, k) - F(-\beta, k)] + \frac{y(f + \sqrt{x^2+y^2})}{x^2+y^2}[R - S]; \quad (27)$$

$$\frac{\partial M}{\partial x} = M' = -\frac{xv(f + \sqrt{x^2+y^2})(2f^2 - x^2 - y^2)}{3f(x^2+y^2)^2}\cdot[E(\gamma, k) - E(-\beta, k)] + \frac{xy(f - \sqrt{x^2+v^2})(2f^2 - x^2 - y^2)}{3f(x^2+y^2)^2}\cdot[F(\gamma, k) - F(-\beta, k)] + \frac{f + \sqrt{x^2+y^2}}{3f(x^2+y^2)^2}[(f^2 + x^2 + y^2)(x^2 - y^2) - 3x^2(x^2+y^2)][R - S] + \frac{f + \sqrt{x^2+y^2}}{3(x^2+y^2)}[(R+S)y\sin\theta_1 - (R - S)x\cos\theta_1]; \quad (28)$$

and

$$\frac{\partial N}{\partial x} = N' = \frac{f + \sqrt{x^2+y^2}}{3f(x^2+y^2)^2}[3x^2(x^2+y^2) - (x^2 - y^2)(f^2 + x^2 + y^2)][E(\gamma, k) - E(-\beta, k)] + \frac{f - \sqrt{x^2+y^2}}{3f(x^2+y^2)^2}[3x^2(x^2+y^2) + (x^2 - y^2)(f^2 - x^2 - y^2)][F(\gamma, k) - F(-\beta, k)] - \frac{xv(f + \sqrt{x^2+y^2})(2f^2 - x^2 - y^2)}{3f(x^2+y^2)^2}[R - S] + \frac{f + \sqrt{x^2+y^2}}{3(x^2+y^2)}[(R+S)x\sin\theta_1 + (R - S)y\cos\theta_1]. \quad (29)$$

In these equations,

F = the elliptic integral of the first kind,
E = the elliptic integral of the second kind,
θ_1 = half the total scan angle,
f = the focal length of the lens,
α, k, β, and γ are as given in Appendix I,

$$R = \sqrt{1 - k^2\sin^2\beta},$$

and

$$S = \sqrt{1 - k^2\sin^2\gamma}.$$

Appendix III

Equation of the Illuminated Surface in Terms of α and κ

The transformation of (8c) to the coordinates α and κ is effected by using the relations

$$\frac{x}{f} = \cos\alpha \tan^2\frac{\kappa}{2} \tag{30a}$$

$$\frac{y}{f} = \sin\alpha \tan^2\frac{\kappa}{2} \tag{30b}$$

$$k^2 = \sin^2\kappa. \tag{30c}$$

After substitution and reduction of the resulting expression, one obtains

$$\frac{\left\{\frac{N}{f} - \frac{L}{f}\left[\frac{\sin\theta_1}{\theta_1}\right]\right\}\left\{N' - L'\left[\frac{\sin\theta_1}{\theta_1}\right]\right\}}{\theta_1 + \sin\theta_1\cos\theta_1 - \frac{2\sin^2\theta_1}{\theta_1}} + \frac{LL'}{2f\theta_1}$$

$$- 2\sin\theta_1 + M'\sin\alpha\tan^2\frac{\kappa}{2} - 2\theta_1\cos\alpha\tan^2\frac{\kappa}{2} = 0, \tag{31}$$

where

$$\frac{N}{f} = \frac{\cos\alpha(1+\tan^4\kappa/2)}{3\sin^2\kappa/2}[E(\gamma,\kappa) - E(-\beta,\kappa)]$$
$$- \frac{\cos\alpha\cos\kappa(1-\tan^4\kappa/2)}{3\sin^2\kappa/2}[F(\gamma,\kappa) - F(-\beta,\kappa)]$$
$$+ \frac{\sin\alpha(1+\tan^4\kappa/2)}{3\sin^2\kappa/2}[V - W]$$
$$+ \frac{2\sin\theta_1}{3\cos^2\kappa/2}[V + W]; \tag{32}$$

$$\frac{L}{f} = \frac{2}{\cos^2\kappa/2}[E(\gamma,\kappa) - E(-\beta,\kappa)]; \tag{33}$$

$$N' = \frac{1}{3\cos^2\kappa/2}\left[1 + \cos^2\alpha - \frac{\cos 2\alpha}{\tan^4\kappa/2}\right]$$
$$\cdot[E(\gamma,\kappa) - E(-\beta,\kappa)]$$
$$+ \frac{\cos\kappa}{3\cos^2\kappa/2}\left[1 + \cos^2\alpha + \frac{\cos 2\alpha}{\tan^4\kappa/2}\right]$$
$$\cdot[F(\gamma,\kappa) - F(-\beta,\kappa)]$$
$$+ \frac{\sin\alpha\cos\alpha}{3\cos^2\kappa/2}\left[1 - \frac{2}{\tan^4\kappa/2}\right][V - W]$$
$$+ \frac{V+W}{3\sin^2\kappa/2}(\cos\alpha\sin\theta_1 + \sin\alpha\cos\theta_1); \tag{34}$$

$$L' = \frac{\cos\alpha}{\sin^2\kappa/2}[E(\gamma,\kappa) - E(-\beta,\kappa)]$$
$$- \frac{\cos\alpha\cos\kappa}{\sin^2\kappa/2}[F(\gamma,\kappa) - F(-\beta,\kappa)]$$
$$+ \frac{\sin\alpha}{\sin^2\kappa/2}(V - W); \tag{35}$$

$$M' = \frac{\sin\alpha\cos\alpha}{3\cos^2\kappa/2}\left[1 - \frac{2}{\tan^4\kappa/2}\right][E(\gamma,\kappa) - E(-\beta,\kappa)]$$
$$+ \frac{\sin\alpha\cos\alpha\cos\kappa}{3\cos^2\kappa/2}\left[1 + \frac{2}{\tan^4\kappa/2}\right]$$
$$\cdot[F(\gamma,\kappa) - F(-\beta,\kappa)]$$
$$- \frac{1}{3\cos^2\kappa/2}\left[1 + \cos^2\alpha - \frac{\cos 2\alpha}{\tan^4\kappa/2}\right][V - W]$$
$$+ \frac{\sin\alpha\sin\theta_1}{3\sin^2\kappa/2}[V + W] - \frac{\cos\alpha\cos\theta_1}{3\sin^2\kappa/2}[V - W]; \tag{36}$$

in which

$$V = \sqrt{1 - \sin^2\kappa\sin^2\beta}$$
$$W = \sqrt{1 - \sin^2\kappa\sin^2\gamma}.$$

The curves $\kappa =$ constant are a family of circles with centers at the origin. For the normalized polar-coordinate radius defined by

$$\frac{\rho}{f} = \sqrt{\left(\frac{x}{f}\right)^2 + \left(\frac{y}{f}\right)^2} \tag{37}$$

it can be shown that

$$\frac{\rho}{f} = \tan^2\frac{\kappa}{2}. \tag{38}$$

The coordinate α is the angle of ρ/f measured from the positive x axis in a counterclockwise sense. These relations are shown in Fig. 6. To compute values of x vs y take successive integral values of κ and find corresponding values of α which satisfy (31). Each pair of such values gives a point on the contour $x(y)$.

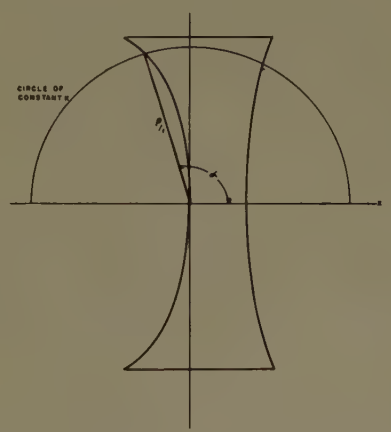

Fig. 6—Illuminated face of scanning lens in terms of coordinates κ and α.

Acknowledgment

The authors wish to express their appreciation to the U. S. Signal Corps and to Sperry Gyroscope Company for permission to publish these results. In addition, the indispensable aid of Richard Angevine in carrying out many difficult integrations and algebraic manipulations is gratefully acknowledged.

Second-Order Beams of Two-Dimensional Slot Arrays*

L. A. KURTZ† AND J. S. YEE‡

Summary—**Second-order beams in the space patterns of two-dimensional slot array antennas may far exceed the sidelobe level and therefore increase the susceptibility of a search radar to jamming or to spurious target echoes. These beams arise from the nonuniform orientation of successive slots; *i.e.*, alternating inclination or displacement with respect to the waveguide axis. In this paper, expressions are derived for the positions of the second-order beams and for their amplitudes relative to the main beam. Experimental verification of these expressions is presented for two-dimensional arrays of edge, series, and shunt slots. Methods for suppressing the second-order beams are discussed.**

Introduction

THE RADIATION PATTERNS of two-dimensional slot arrays frequently contain second-order beams whose magnitudes far exceed the low values demanded of the sidelobes. Lying outside the principal coordinate planes of the main beam, these beams may be easily overlooked during radiation pattern measurements. Because of the present-day emphasis on achieving low sidelobes to reduce the susceptibility of a radar to jamming, it is imperative that these second-order beams be suppressed.

The source of the second-order beams lies in the small differences in the orientation of successive slots. For instance, edge slots and series slots are inclined to the waveguide axis in order to couple to the fields within; however, successive slots have opposite inclinations in order to preserve the proper phase relations. Similarly, shunt slots, which are parallel to the waveguide axis, are displaced on alternate sides of the center line in order to couple with the proper phase relations to the fields within. As a result of this nonuniform orientation of successive slots, there are usually certain directions in which their radiated fields fail to cancel as expected so that second-order beams appear.

The term "second-order beams" was used by Gruenberg[1] in a study of linear arrays of shunt slots. He considered the slots on one side of the centerline as forming one array and the slots on the opposite side as forming a secondary array. In the present analysis, only one array is assumed, but groups of slots instead of single slots are considered as elements of the array. Of course, either method should lead to the same results.

The following study was made to determine the position and magnitudes of the second-order beams as functions of slot geometry and relative phase. Three types of slots and two types of arrays are discussed: edge, series, and shunt slots with adjacent linear arrays that are either identical or mirror images. Experimental measurements on arrays of each type of slot are presented along with means for suppressing the second-order beams.

* Original manuscript received by the PGAP, October 31, 1956; revised manuscript received, April 19, 1957. Presented at the Spring Meeting of URSI, Natl. Bur. of Standards, Washington, D. C., May, 1956. This work was performed while the authors were members of the Technical Staff, Microwave Lab., Hughes Aircraft Co., Culver City, Calif.

† Rantec Corp., Calabasas, Calif.

‡ Boling Aircraft Co., Seattle, Washington.

[1] H. Gruenberg, "Second-order beams of slotted waveguide arrays," *Can. J. Phys.* vol. 31, pp. 55–69; January, 1953.

Analysis

The radiation pattern of a two-dimensional array is generally described by the product of an array factor and an element factor. These factors express the sum of the contributions from each of the elements to the field in a given direction in space. The element factor describes the radiation from a single element, and the array factor accounts for the relative amplitudes, phases, and positions of the elements in the array. Separating the element factor from the array factor is permissible only if all elements of the array are identical.

Often, for the purpose of radiation-pattern calculations, the slots in an array are assumed to be identical. This assumption cannot be made, however, if second-order beams are to be taken into account. Instead, it becomes necessary to group the slots into the smallest number so that successive groups appear identical. The radiation pattern of the group then becomes the element factor for the array. The slots within an element group, however, are assumed to have equal amounts of inclination or displacement and equal amplitudes of excitation. These assumptions may be made safely for large arrays of many elements where the change in aperture illumination between successive slots is small. For small arrays the assumptions are still adequate if the aperture distributions are symmetrical and there are even numbers of rows and columns. To allow for the variations due to tapered aperture distributions, an averaged value of inclination or displacement should be used as discussed in the experimental portion of this paper.

A group of four slots has been chosen to form the elements in the present analysis. This choice was made because four slots are required in the element group when adjacent linear arrays appear as mirror images of each other (left-hand group at the bottom of Table I). Only two slots per group are required when adjacent linear arrays are identical; however, this case is included in the more general analysis of the four-slot group.

With four slots combined into one element, the element spacing becomes twice the slot spacing and the phase shift between elements becomes twice the phase shift between slots. The radiation pattern of a plane two-dimensional array may then be written as

TABLE I*

SUMMARY OF SECOND-ORDER BEAM EXPRESSIONS

Inclined Slots

$$S = 10 \log_{10} \frac{\left| \sin^2\beta(L_1+L_2)^2\left[1-\left(\frac{\gamma_1+p}{2d_1}\right)^2\right] + \cos^2\beta(L_1-L_2)^2\left[1-\left(\frac{\gamma_2+q}{2d_2}\right)^2\right] \right.}{\left| \sin^2\beta(L_1-L_2)^2\left[1-\left(\frac{\gamma_1}{2d_2}\right)^2\right] + \cos^2\beta(L_1+L_2)^2\left[1-\left(\frac{\gamma_2}{2d_2}\right)^2\right] \right.}$$

$$\frac{\left. + \sin 2\beta(L_1^2-L_2^2)\left(\frac{\gamma_1+p}{2d_1}\right)\left(\frac{\gamma_2+q}{2d_2}\right)\right| p, q \text{ (see diagram)}}{\left. + \sin 2\beta(L_1^2-L_2^2)\left(\frac{\gamma_1}{2d_2}\right)\left(\frac{\gamma_2}{2d_2}\right)\right| p = q = 0}$$

$$L_i = \frac{\cos\left[\frac{\pi}{2}\left(\frac{\gamma_2+q}{2d_2}\cos\beta_i + \frac{\gamma_1+p}{2d_1}\sin\beta_i\right)\right]}{1-\left(\frac{\gamma_2+q}{2d_2}\cos\beta_i + \frac{\gamma_1+p}{2d_1}\sin\beta_i\right)^2} \qquad \gamma = \frac{\text{phase shift}}{\pi}$$

$$d = \frac{\text{slot spacing}}{\lambda}$$

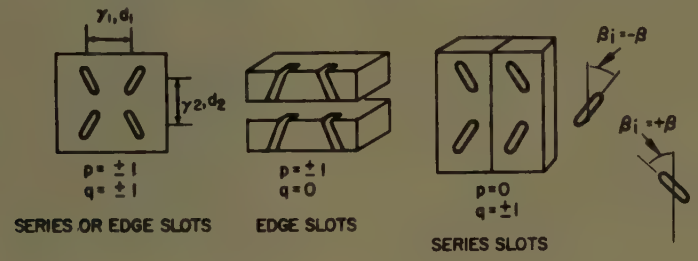

Displaced Slots

$$= 10 \log_{10} \left| \frac{L^2\left[1-\left(\frac{\gamma_2+q}{2d_2}\right)^2\right]\sin^2\left(\frac{\gamma_1+p}{d_1}\delta\pi\right)}{L^2\left[1-\left(\frac{\gamma_2}{2d_2}\right)^2\right]\cos^2\left(\frac{\gamma_1}{d_1}\delta\pi\right)} \right| \begin{matrix} p, q \\ p = q = 0 \end{matrix}$$

$$\delta = \frac{\text{slot displacement}}{\lambda}$$

$$L = \frac{\cos\left[\frac{\pi}{2}\left(\frac{\gamma_2+q}{2d_2}\right)\right]}{1-\left(\frac{\gamma_2+q}{2d_2}\right)^2}$$

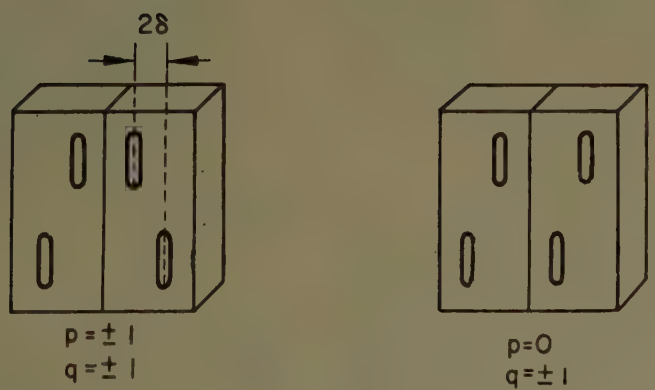

* The figures denote design of edge-slot linear arrays.

$$E(\theta, \phi) = F_4(\theta, \phi) \sum_{n=0}^{N/2} A_n e^{jn(k2d_1 \sin\theta \sin\phi - 2\gamma_1)} \cdot \sum_{m=0}^{M/2} A_m e^{jm(k2d_2 \cos\theta - 2\gamma_2)} \qquad (1)$$

where

$F_4(\theta, \phi)$ = element factor for group of four slots,

A_n, A_m = relative amplitudes of the groups.

This radiation pattern will have principal maxima whenever contributions from all element groups add in phase; that is, when both phase factors are either zero or multiples of 2π. Thus

$$(k2d_1 \sin\theta \sin\phi - 2\gamma_1) = 2\pi p, \quad p = 0, \pm 1, \pm 2 \cdots$$

$$(k2d_2 \cos\theta - 2\gamma_2) = 2\pi q, \quad q = 0, \pm 1, \pm 2 \cdots . \qquad (2)$$

In practical arrays, recurrence of the main beams is

avoided by restricting[2] the values of d_1 and d_2 to lie between $\lambda/2$ and λ, or by limiting the values of γ_1 or γ_2 to less than their full range of $-\pi$ to $+\pi$. Observing these restrictions, solutions to (2) can be found for at most only three values of p and q, namely, 0 and ± 1. Thus, there are nine possible directions of principal maxima of which only one, $p=q=0$, corresponds to the main beam. The other values for p and q correspond to second-order beams.

Since the array factor portion of (1) has principal maxima in the directions of the second-order beams as well as the direction of the main beam, the magnitudes of the second-order beams are determined almost entirely by the group element factor. The method followed in calculating these magnitudes is outlined in the Appendix, while the results of the calculations are presented in Table I. Two expressions giving the relative magnitudes of the second-order beams have been derived, one for inclined slots and one for displaced slots. The values of p and q corresponding to the types of slots are shown at the bottom of Table I. A general picture of the positions of the second-order beams can be obtained if the slots are assumed to be in phase and spaced 0.7λ. Then for the mirror image array, there are four second-order beams approximately centered in the four sectors of space in front of the array. For identical arrays there are only two second-order beams and they lie in a plane perpendicular to the plane of the array and parallel to the linear arrays. They lie at 45° relative to the broadside direction.

The expressions for S in Table I contain only the parameters of the array and the values of p and q. The parameters are the slots spacing, the relative phase shift, and the angle of inclination or the displacement. Once these are specified, the magnitudes of the second-order beams can be calculated directly. If the positions of the second-order beams are required they may be obtained from (2), again in terms of the parameters of the array and the values of p apd q.

Experimental Verification

Measurements of second-order beams have been performed using three two-dimensional arrays consisting of identical linear arrays of edge, series, and shunt slots respectively. The slot spacings were one-half guide wavelength so that the relative phase along the linear arrays was zero. The spacings between linear arrays were also one-half guide wavelength, and the relative phase between linear arrays was varied by changing the path length between the coupling slots in the feed array. Fig. 1 is a photograph of the edge-slot two dimensional array and Fig. 2 is a radiation pattern, $\gamma_1=\gamma_2=0$, illustrating second-order beams.

The second-order beams of the edge-slot array were measured for several values of phase shift γ_2. The measured values together with values calculated using the

[2] S. Silver, "Microwave Antenna Theory and Design," McGraw-Hill Book Co., Inc., New York, N. Y., ch. 9, sec. 9: 19, p. 318; 1949.

Fig. 1—Sixteen-by-sixteen array of edge slots. The path length between feed slots can be varied by means of waveguide inserts to obtain a variable phase shift, γ_2.

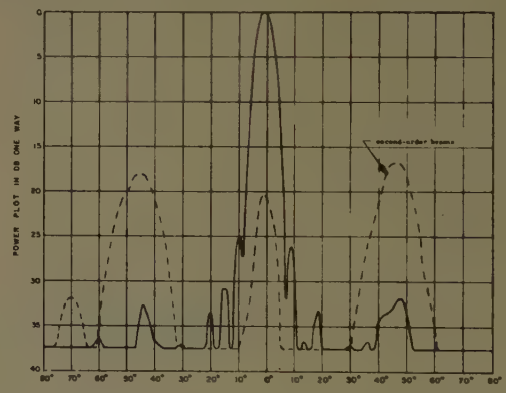

Fig. 2—*E*-plane radiation pattern of 16×16 array of edge slots showing cross-polarized second-order beams. There is a gap of 0.380 inch between waveguides.

expressions from Table I are shown in Fig. 3. Since the aperture distribution of the array is tapered, an average value of 13.6° was used for B. In order to choose this average value, the conditions of broadside operation were considered. For these conditions ($\gamma_1=\gamma_2=0$, $q=0$, $p=\pm 1$, $L_1=L_2$), the expression for second order beams reduces to

$$S = 10\log_{10}\frac{\left|\left[1-\left(\frac{1}{2d_1}\right)^2\right]\cos^2\left(\frac{\pi}{4d_1}\sin B\right)\sin^2 B\right|}{\left[1-\left(\frac{1}{2d}\sin\beta\right)^2\right]\cos^2 B} \quad (3)$$

For small angles the cosine terms approximately cancel and the denominator is nearly unity so that the ratio

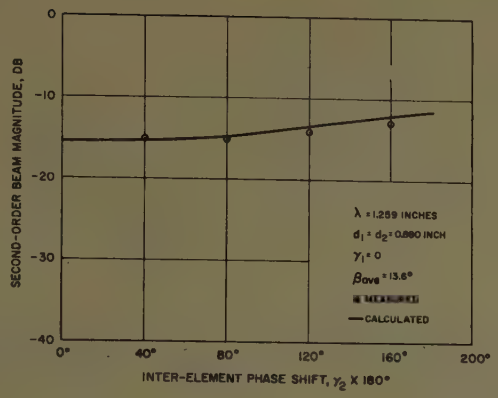

Fig. 3—Second-order beam magnitude vs phase shift for a 16×16 array of edge slots.

Fig. 4—Seven-by-ten array of series slots showing the variable path length feed. All slots are inclined 11.1°.

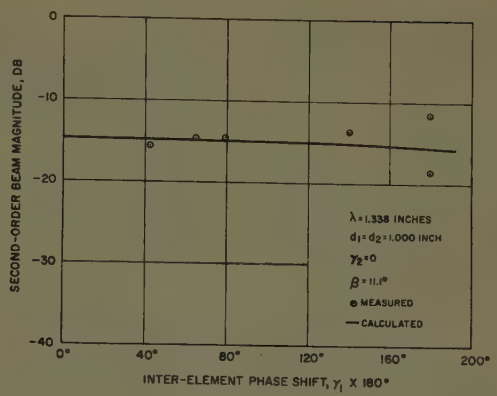

Fig. 5—Second-order beam magnitude vs phase shift for a 6×10 array of series slots.

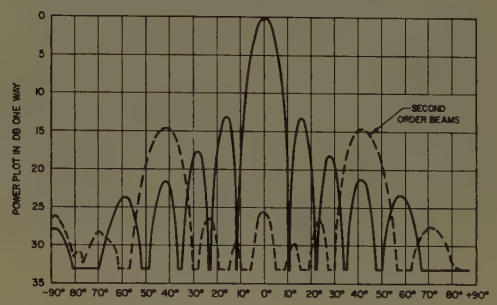

Fig. 6—*H*-plane radiation pattern of the 7×10 array of series slots with uniform illumination: $f = 8820$ mc.

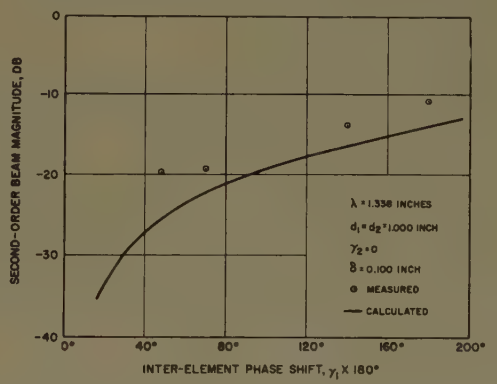

Fig. 7—Second-order beam magnitude vs phase shift for a 6×10 array of shunt slots.

of second-order beam to main beam is a constant times sin B. Thus, by adding the second-order beam and main beam fields of all the slot groups an average value was obtained for sin B and hence for B.

$$\sin B_{\text{ave}} = \frac{\sum_n A_n \sin B_n}{\sum_n A_n} . \qquad (4)$$

All the linear arrays are identical, hence B varies only along one coordinate of the array and the averaging need be done for only one linear array.

The second-order beams of the series-slot array in Fig. 4, were measured, and their values together with values calculated using the expressions of Table I are plotted in Fig. 5. A radiation pattern showing the cross-polarized, second-order beams is given in Fig. 6. Only six of the seven rows of slots were used in the second-order beam measurements to avoid having a side lobe of the main beam lie in the same direction as the second-order beam.

An array of shunt slots, similar in appearance to the series slot array, was used in a third measurement of second-order beams. The results of these measurements are shown in Fig. 7. The differences between measured and calculated values can be explained largely by the fact that the second-order beams and the side lobes of the main beam have the same polarization. It is noteworthy that a two-dimensional array of shunt slots with broadside beam does not produce second-order

beams provided that the beam widths are sufficiently narrow and that the linear arrays are identical.

The displacements of all the slots in the edge slot array are one-tenth inch. If the displacements were unequal, however, an average value for δ could be calculated in a manner similar to the calculation of B average. Adding the contributions to the second-order beam field and main beam field of each element group leads to the relation

$$\tan\left(\frac{\gamma_1}{d_1}\pi\delta_{ave}\right) = \frac{\sum_m A_m \sin\left(\frac{\gamma_1}{d_1}\pi\delta_m\right)}{\sum_m A_m \cos\left(\frac{\gamma_1}{d_1}\pi\delta_m\right)}. \quad (5)$$

Suppression of Second-Order Beams

The methods used for suppressing second-order beams may be simple or complex, depending on the design and scanning requirements of the two-dimensional array. Perhaps the most obvious method is to eliminate the cause of the second-order beams by aligning the slots so they are colinear. Colinear alignment of the slots may be obtained by using a corrugated-wall waveguide,[1] probe-fed slots,[3] or iris-fed slots.[4] For the three types of slots considered here, such alignment is not possible. It was seen, however, that operating near $\gamma_1=0$ effectively suppresses second-order beams of identical linear arrays of shunt slots.

Another method for suppressing second-order beams is to restrict the spacing between slots so that the beams are outside visible space. This method, when practical, serves only for near-broadside operation of large arrays with narrow beamwidths and it requires that adjacent linear arrays be mirror images. The limitations on spacing can be readily determined from (2) which gives the directions of the second-order beams. For example, consider the case of broadside operation, $\gamma_1=\gamma_2=0$, and equal slot spacing, $d_1=d_2=d$. Then,

$$\sin\theta\sin\phi = \frac{\pm 1}{2d}$$

$$\cos\theta = \pm\frac{1}{2d}, \quad (6)$$

and these relations can be satisfied only as long as $|\sin\theta|$ is larger than or equal to $|\cos\theta|$. If d is chosen such that (6) cannot be satisfied, there will be no second-order beam; therefore, d should be less than 0.707. (This may require loading a waveguide to reduce its physical size sufficiently.) An easy way to visualize this situation is to note that (2) represents two sets of cones centered, respectively, on the y and z axis. The directions of the second-order beams correspond with the intersections of the cones determined by $p=\pm 1$, $q=\pm 1$. With the above restrictions imposed on d,

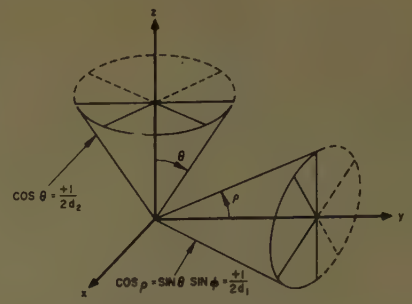

Fig. 8—Cones represented by (2) with $\gamma_1=\gamma_2=0$, $d_1=d_2=0.6$, $p=q=1$. Since d_1 and d_2 are less than 0.707, the cones do not intersect and there are no second-order beams.

these cones do not intersect, and there are no second-order beams. Such a situation is depicted in Fig. 8.

A method that is suitable for suppressing second-order beams of edge slots is to suppress the z component of the surface current generated by the slots. The gap between the waveguides supporting the edge slots forms an effective choke for this purpose if its depth (dimension c in Fig. 9) is suitably chosen. A curve showing the effectiveness of chokes in the array in Fig. 1 is given in Fig. 10. In addition to its critical dependence on choke depth, the effectiveness of chokes depends also on the phase shift between slots, γ_2, in the manner shown in Fig. 11. The reason for this dependence is that the field in the choke, E_c, consists of approximately equal contributions from the slots on either side of the choke. Therefore, as the relative phase of these contributions tends toward 180° the value of E_c tends toward zero with the result that there is very little suppression of the second-order beams. The situation is reversed if the linear arrays happen to be mirror images because then the components of the surface current are 180° out of phase when $\gamma_2=0$. The chokes are effective in this case only when γ_2 tends toward 180°.

In order to eliminate second-order beams for all values of γ and d and for all types of slots, it is necessary to use baffles between slots, as shown in Fig. 12. The baffles form parallel plate horns that force the electric field to lie entirely in the y direction and to be independent of the slot orientation. Any amount of suppression can be obtained by adjusting the width and height of the baffles. As an example, baffles one-half wavelength high, with a 0.39-wavelength gap between, reduced the second-order beams by more than 12 db over the entire range of γ_2.

Conclusion

The second-order beam magnitudes have been determined for two-dimensional arrays with mirror-image linear arrays and with identical linear arrays consisting of edge slots, series slots, and shunt slots. The second-order beams are of seriously high magnitudes for all cases except the special one of a broadside array of shunt slots in which the linear arrays are identical. Equations have been derived for the directions and magnitudes of the second-order beams, and they are summarized in Table I. The equations have been verified experiment-

[3] *Ibid.*, p. 301.
[4] R. Tang, "A Slot with Variable Coupling and Its Applications to a Linear Array," Hughes Aircraft Co., Report RLM (M) 56-15; July, 1956.

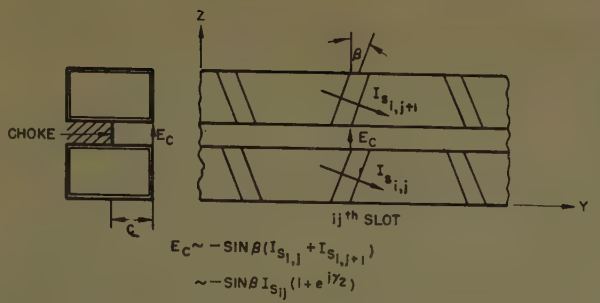

Fig. 9—The choke between these waveguides suppresses second-order beams when the depth c is one quarter wavelength. Attenuation of second-order beams is greatest for $\gamma_2=0$ and it is zero for $\gamma_2=180°$.

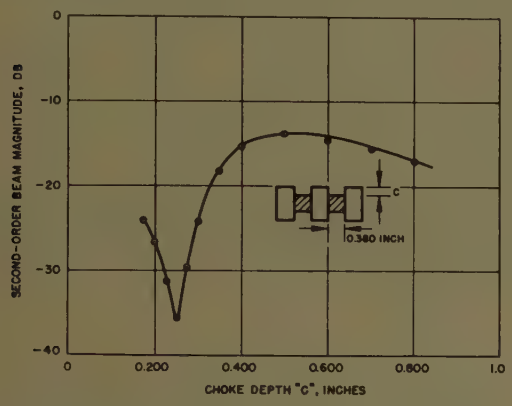

Fig. 10—Magnitude of second-order beam vs choke depth: $\lambda=1.259$ inches.

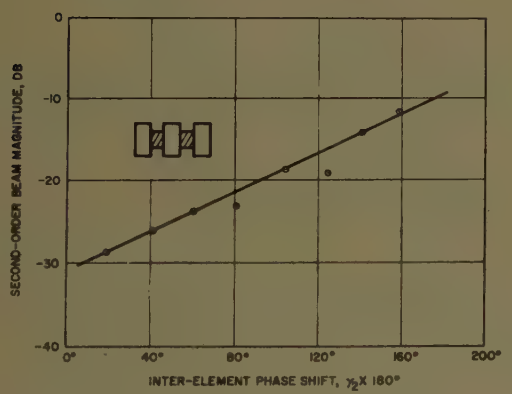

Fig. 11—Second-order beam magnitude versus phase shift for a 16×16 edge-slot array with chokes.

ally by using three two-dimensional arrays. Several means are described that result in reduced levels for the second-order beams. So far as it is known, however, baffles are the only means by which these beams can be satisfactorily suppressed for all scan angles. Baffles may increase weight, conplexity, and mutual coupling, but they have yielded the best results so far achieved.

Appendix

To illustrate the method used in deriving the expressions given in Table I, the derivation will be made for the combination of inclined slots shown at the lower left corner of Table 1. The group element factor is obtained by adding together, with proper phase retardations, the fields of the four individual slots in the group.

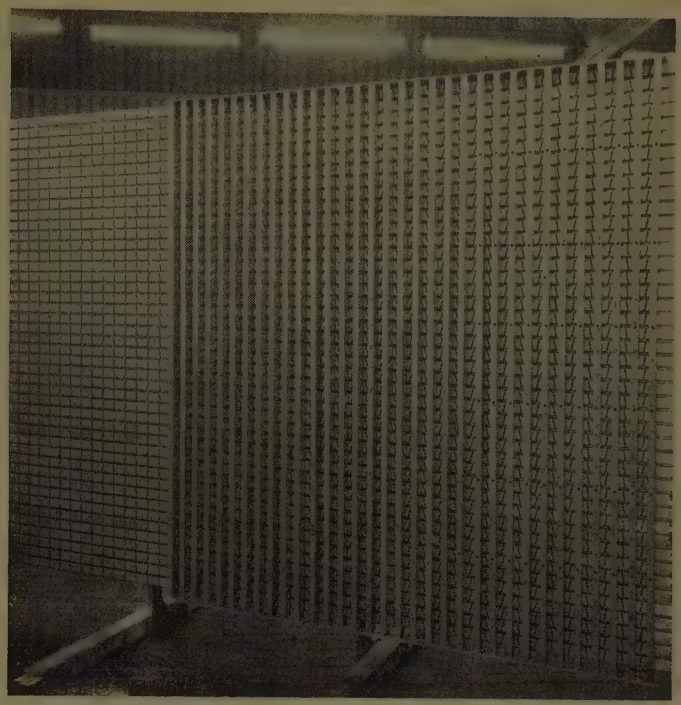

Fig. 12—Two-dimensional array of edge slots showing baffles that suppress the second-order beams.

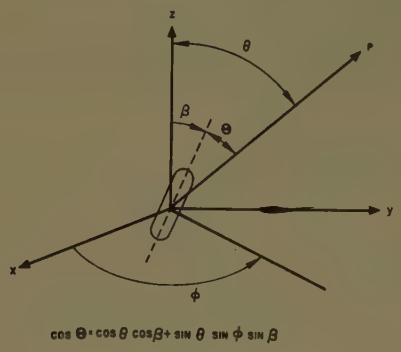

Fig. 13.

This may be done conveniently in terms of the magnetic radiation vector L. Using the magnetic radiation vector, the electric field radiated by the inclined slot of Fig. 13 may be written[5] as

$$E_\theta = -j\frac{e^{-jkr}}{2\lambda r}(L_y\cos\phi)$$

$$E_\phi = j\frac{e^{-jkr}}{2\lambda r}(L_y\sin\phi\cos\theta - L_z\sin\theta), \qquad (7)$$

where

$$L_y = \frac{4gE_m}{K}\frac{\cos\left[\frac{\pi}{2}\cos\Theta\right]}{\sin^2\Theta}\sin B$$

$$L_z = \frac{4gE_m}{K}\frac{\cos\left[\frac{\pi}{2}\cos\Theta\right]}{\sin^2\Theta}\cos B. \qquad (8)$$

[5] S. Ramo and J. R. Whinnery, "Fields and Waves in Modern Radio," John Wiley and Sons, Inc., New York, N. Y., sec.12:21 p. 535; 1953.

The radiated field for the four inclined slots is obtained by inserting their combined magnetic radiation vector in (7). This combined magnetic radiation vector is

$$L_y = \frac{4gE_m}{K}\sin B\left[-L_1 - L_1 e^{j(kd_1 \sin\theta\sin\phi-\gamma_1)}e^{j(kd_2\cos\theta-\gamma_2)} + L_2 e^{j(kd_1\sin\theta\sin\phi-\gamma_1} + L_2 e^{j(kd_2\cos\theta-\gamma_2)}\right]$$

$$L_z = \frac{4gE_m}{K}\cos B\left[L_1 + L_1 e^{j(kd_1\sin\theta\sin\phi-\gamma_1)}e^{j(kd_2\cos\theta-\gamma_2)} + L_2 e^{j(kd_1\sin\theta\sin\phi-\gamma_1)} + L_2 e^{j(kd_2\cos\theta-\gamma_2)}\right]. \quad (9)$$

L_1 and L_2 are obtained by substituting $-B$ and $+B$ as indicated in Table I into the expression

$$L_i = \frac{\cos\left[\frac{\pi}{2}\cos\Theta_i\right]}{\sin^2\Theta}, \quad (10)$$

where $\cos\Theta_i = \cos(\theta\cos B_i) + \sin\theta\sin\phi\sin B_i$.

It should be noted that the algebraic sign of $\sin B$ has been accounted for inside the brackets of (9). Hence $\sin B$ is always positive. Effectively $\sin B = |\sin B_i|$.

The expressions for the magnetic radiation vector can be simplified for the purpose of calculating second-order beams since only directions given by (2) are of interest. Eq. (2) can be solved for $\sin\theta\sin\phi$ and $\cos\theta$. Letting λ be the unit measure of d and π the unit measure of γ

$$\sin\theta\sin\phi = \frac{\gamma_1 + p}{2d_1}, \qquad p = 0, \pm 1$$

$$\cos\theta = \frac{\gamma_2 + q}{2d_2}, \qquad q = 0, \pm 1. \quad (11)$$

With the substitution of (11), (9) and (10) become

$$L_y = \frac{4gE_m}{K}\sin B\left\{-L_1[1 + e^{j(p+q)\pi}] + L_2[e^{jp\pi} + e^{jq\pi}]\right\}$$

$$L_z = \frac{4gE_m}{K}\cos B\left\{L_1[1 + e^{j(p+q)\pi}] + L_2[e^{jp\pi} + e^{jq\pi}]\right\} \quad (12)$$

and

$$L_i = \frac{\cos\left[\frac{\pi}{2}\left(\frac{\gamma_2 + q}{2d_2}\cos B_i + \frac{\gamma_1 + p}{2d_1}\sin B_i\right)\right]}{1 - \left(\frac{\gamma_2 + q}{2d_2}\cos B_i + \frac{\gamma_1 + p}{2d_1}\sin B_i\right)^2}. \quad (13)$$

In (12) it is apparent that only for p and q not equal to zero do the second order beams appear for this slot configuration.

The magnitude of the second-order beam relative to mainbeam is found by taking the ratio of the electric fields radiated in their respective directions. This ratio, expressed in db and denoted by S, is

$$S = 10\log_{10}\frac{|E_\theta^2 + E_\phi^2|\ p = \pm 1, q = \pm 1}{|E_\theta^2 + E_\phi^2|\ p = q = 0}. \quad (14)$$

The expression $|E^2_\theta + E^2_\phi|$ may be simplified by again using (11) and neglecting constants that will eventually cancel in the ratio.

$$|E_\theta^2 + E_\phi^2|$$

$$\sim L_y^2\cos^2\phi + (L_y\sin\phi\cos\theta - L_z\sin\theta)^2$$

$$\sim L_y^2(1 - \sin^2\phi\sin^2\theta) + L_z(1 - \cos^2\theta) - 2L_yL_z\cos\theta\sin\theta\sin\phi$$

$$\sim L_y^2\left[1 - \left(\frac{\gamma_1 + p}{2d_1}\right)^2\right] + L_z\left[1 - \left(\frac{\gamma_2 + q}{2d_2}\right)^2\right] - 2L_yL_z\left(\frac{\gamma_1 + p}{2d_1}\right)\left(\frac{\gamma_2 + q}{2d_2}\right). \quad (15)$$

Finally, then, the magnitudes of the second-order beams for the four inclined slots are obtained substituting (12) and (15) into (14):

$$S = 10\log_{10}\frac{\left|\sin^2 B(L_1 + L_2)^2\left[1 - \left(\frac{\gamma_1 + p}{2d_1}\right)^2\right] + \cos^2 B(L_1 - L_2)^2\left[1 - \left(\frac{\gamma_2 + q}{2d_2}\right)^2\right]\right.}{\left|\sin^2 B(L_1 - L_2)^2\left[1 - \left(\frac{\gamma_1}{2d_1}\right)^2\right] + \cos^2 B(L_1 + L_2)^2\left[1 - \left(\frac{\gamma_2}{2d_2}\right)^2\right]\right.}$$

$$\frac{\left.\sin 2B(L_1^2 - L_2^2)\left(\frac{\gamma_1 + p}{2d_1}\right)\left(\frac{\gamma_2 + q}{2d_2}\right)\right| p = \pm 1, q = \pm 1}{\left.\sin 2B(L_1^2 - L_2^2)\left(\frac{\gamma_1}{2d_1}\right)\left(\frac{\gamma_2}{2d_2}\right)\right| p = q = 0}. \quad (16)$$

Eqs. 13 and 16 appear in Table I.

20-70 MC Monopole Antennas on Ground-Based Vehicles*

ROBERT E. WEBSTER†

Summary—Antenna design for ground-based vehicular application is discussed with particular emphasis on omnidirectional, vertically polarized types. Limitations of vehicle size and shape in controlling the efficiency and radiation patterns are considered. Pronounced interferences are shown to arise from the usually nonsymmetrical currents to the earth. Modifications of vehicle and antenna proved effective in reducing this interference. The radiation characteristics of vertical monopoles excited against the vehicle are shown over the frequency band.

Introduction

THIS paper is concerned with communication antennas on ground-based vehicles in the frequency range where the vehicle dimensions become appreciable in terms of a wavelength. The vehicle of primary interest was the $\frac{3}{4}$-ton army weapons carrier, the body of which is elevated several feet above the earth and insulated from it with lossy dielectrics (rubber tires). Profiles of this truck with the presently used 20–70 mc whip antenna are shown in Fig. 1. This antenna and the associated radio equipment are designed for short-range ground wave communication among a number of such units. Vertical polarization and omnidirectional radiation patterns were therefore of particular interest in the investigation.

The two factors which render the design of antennas for this type of ground-based vehicle somewhat less than straightforward are the relatively complex geometry of the vehicle, and the presence of an imperfectly conducting ground. This first difficulty has received considerable attention in investigations of aircraft antennas.[1] Current distribution measurements have revealed the nature of favored current flow paths on such structures.[2–4] Since the contours of truck vehicles are even more complex than those of most aircraft, many discrete paths with high current densities are to be expected. The second complication of a lossy material beneath the behicle is an added problem for ground-based structures. The effect of lossy ground on antenna impedances has been treated for certain symmetrical

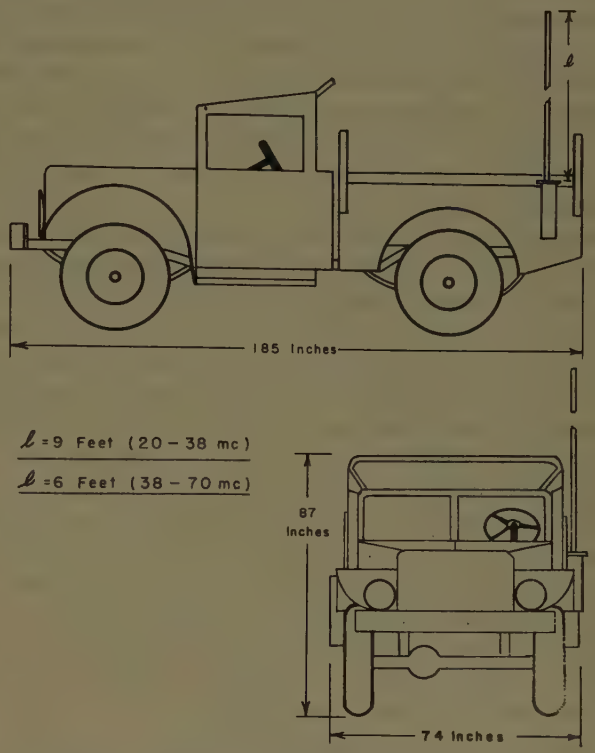

Fig. 1—Profiles of $\frac{3}{4}$-ton army weapons carrier with standard whip antenna.

configurations.[5,6] Obstacles to the determination of ground current distribution and resultant losses and radiation patterns for the vehicular antennas of interest here are the elevation of the bodies above the earth and their pronounced asymmetries.

The success achieved in this type of antenna design is then dependent on the extent to which the current distribution over the vehicle surface can be controlled in the presence of those contours which are considered unalterable, and an imperfectly conducting earth. The available design parameters are controls of the driven elements (number, size, shape, and location) and practicable modifications of the vehicle.

Limitations Imposed by the Vehicle

In view of the sharply discontinuous metal contours of these vehicles, it would seem desirable to avoid the problem of controlling the body surface current distribution. At the high-frequency end of the 20–70 mc band

* Manuscript received by the PGAP, January 30, 1956; revised manuscript received, March 15, 1957. This article is based on work done under a contract between the Ohio State Univ. Res. Foundation and the Signal Corps. Eng. Labs., Fort Monmouth, N. J.

† Antenna Lab., Ohio State Univ., Columbus, Ohio.

[1] J. V. N. Granger and J. T. Bolljahn, "Aircraft antennas," PROC. IRE, vol. 43, pp. 533–550; May, 1955.

[2] J. V. N. Granger and T. Morita, "Radio-frequency current distributions on aircraft structures," PROC. IRE, vol. 39, pp. 932–938; August, 1951.

[3] I. Carswell, "Current distribution on wing-cap and tail-cap antennas," IRE TRANS., vol. AP-3, pp. 207–212; October, 1955.

[4] A. R. Ellis, "Methods of Improving Tail-Cap Antenna Patterns," Tech. Rep. No. 35, Contract AF 19(604)-1296, Stanford Res. Inst., Stanford, Calif.; January, 1955.

[5] F. R. Abbott, "Design of optimum buried-conductor rf ground system," PROC. IRE, vol. 40, pp. 846–852; July 1952.

[6] J. R. Wait, "Impedance of a top-loaded antenna of arbitrary length over a circular grounded screen," *J. Appl. Phys.*, vol. 25, pp. 553–555; May, 1954.

a choke system, such as loaded dipoles with sleeves, for minimizing the antenna-vehicle coupling is feasible. Such systems, of course, are frequency sensitive and often are not easily adjusted. At the low frequencies, however, purely mechanical considerations limit the protrusion of the radiators from the vehicle. Then it becomes necessary to use the vehicle as a counterpoise in order to obtain reasonable efficiencies, and no effective isolation of vehicle and antenna is possible. The primary design problem then becomes that of arranging the driven element to produce the desired current distribution on the vehicle.

Regarding impedance limitations, it can be shown that no great difficulty exists in this frequency range if full use is made of the available volume within the vehicle contours (assuming, of course, that no attempt is made to obtain a highly directive antenna). The relatively large electrically open regions enclosed only by canvas and wood structure on these vehicles permit this freedom in impedance design. With compensation at the low-frequency end we can expect a standing-wave ratio less than 5 to 1 over the entire band. Such impedances were actually obtained with fan-shaped screen antennas placed along the canvas contours.[7] Impedance bandwidths of the presently used whip antennas, which consist of thin linear elements protruding to a maximum height of approximately seven feet above the vehicle, also fall within these limits.

The rather obvious mechanical limitations of antenna elements on ground-based vehicles may be briefly summarized as follows.

1) Flexibility and light weight are always desirable.
2) If the structure is confined within the vehicle contours, however, it may be reasonably rigid.
3) Protruding elements, such as whips, must be of a smooth, thin shape and highly flexible to prevent damage from passing obstacles.

The tendency of the complex geometry of the vehicle surfaces to control the surface current distribution is the limitation of primary importance in antenna design for this class of vehicles. The results of simple modifications of the vehicle contours are shown in the following sections, in addition to improvements in radiation characteristics obtained by major contour changes.

Effect of the Earth

The close proximity to the earth of current-carrying surfaces of ground-based vehicles suggests an influence on the efficiency and current distribution of vehicular antennas due to the earth's behavior as an imperfect conductor. Measurements of earth constants by McPetrie[8] yielded the values $\sigma = 0.10$ mho/meter and $\epsilon/\epsilon_0 = 7$ to 16 for the conductivity and relative dielectric constant, respectively. These values are known to vary with soil types and moisture content. Choosing $\sigma = 0.10$ and $\epsilon/\epsilon_0 = 15$ as typical values and computing the earth's intrinsic impedance, we obtain $\eta_1 = 39.5 \angle 40°$ as compared with the value for free space above the earth $\eta_0 = 377 \angle 0°$. This impedance discontinuity results in a reflection coefficient $\rho = 0.85 \angle 172°$ for a plane wave incident normal to the earth from the space above. The ratio $\sigma/\omega\epsilon$ over the 20–70 mc range is seen to be approximately 9 to 2.6. These measurements depict the earth as a lossy conductor in this frequency band. Thus, its presence is commonly expected to produce pronounced changes in the free-space radiation properties of vehicular antennas.

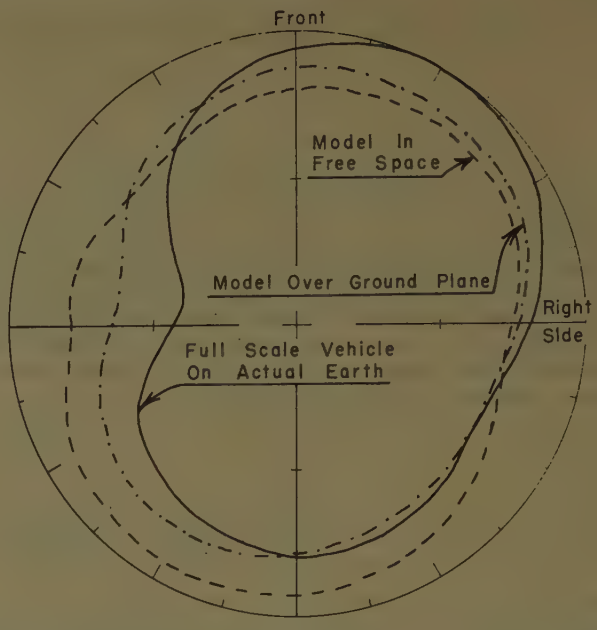

Fig. 2—Horizontal plane relative electric field intensity patterns for standard whip antenna on ¾-ton weapons carrier vehicle (see Fig. 1). Full-scale and 1/15-scale model patterns. Vertical polarization. 28 mc full-scale frequency.

The patterns of Fig. 2 indicate this effect to some extent although at that frequency the modification was not critical. Striking effects are seen in Figs. 3 and 4, which show radiation patterns and current density distribution measurements obtained for the previously described whip antenna and for a symmetrically located, inverted-L monopole on the 1/15-scale model vehicle at frequencies where the currents to ground were critical. Notice that the vehicle was modified by removal of the top cab structure and closure of the gap behind the cab so that the vehicle would approximate more closely the idealization of an electrically smooth body. The notation of the current distribution plots is as follows.

1) The dot denotes the point of measurement.
2) The arrow stem shows the axis of current flow.
3) The arrow head indicates the assumed positive sense of current.
4) The numbers give the amplitude and phase of the voltage induced in a small loop held perpendicular to the surface.

[7] D. R. McCoy and R. E. Webster, "Model Techniques in 20–70 MC Vehicular Antenna Research," Rep. 522-7, Ohio State Univ. Res. Foundation, Antenna Lab., prepared under Contract DA 36-039 sc42548, U. S. Army Signal Corps Eng. Lab., Fort Monmouth, N. J.; April 30, 1954.

[8] J. S. McPetrie, "A determination of the electrical constants of the earth's surface at wavelengths of 1.5 and 0.46 meters," *Proc. Phys. Soc.*, vol. 46, pp. 637–648; September, 1934.

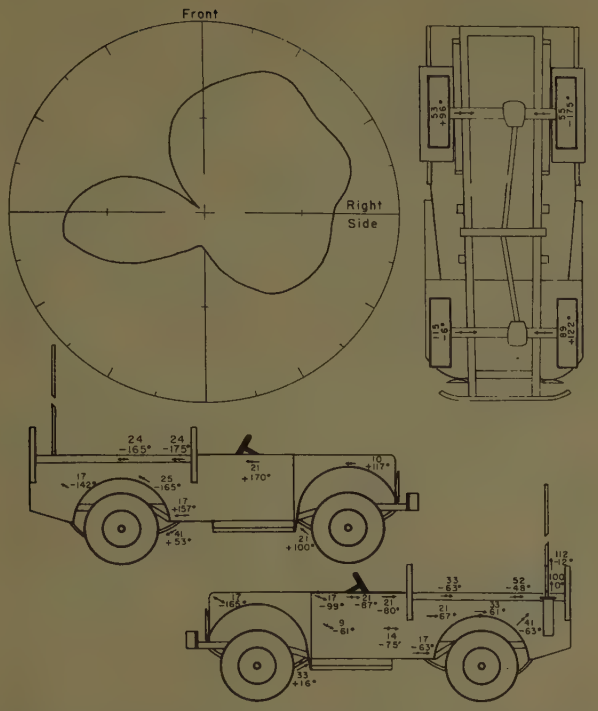

Fig. 3—Horizontal plane radiation pattern and current density distribution for whip antenna on modified 1/15-scale model of $\frac{3}{4}$-ton weapons carrier vehicle over ground plane. 44 mc equivalent full-scale frequency.

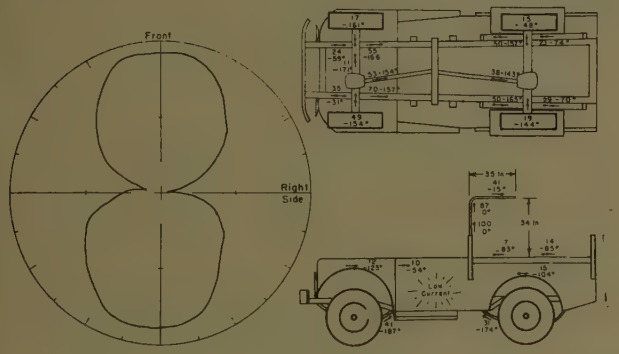

Fig. 4—Horizontal plane radiation pattern and current density distribution for inverted-L antenna on modified 1/15-scale model of $\frac{3}{4}$-ton weapons carrier vehicle over ground plane. 50 mc equivalent full-scale frequency.

Because of the finite loop size and the very complex surface geometries, the loop voltage vs current density correspondence is not perfect. Nevertheless, these measurements have been invaluable in establishing the nature of current distributions on these vehicles.

The deep null off the left front (Fig. 3) is characteristic for the whip antenna. Its depth and azimuthal location change with frequency and ground conditions, as will be seen in the next section, but its presence and presumably its cause is invariable. It is seen from the current distribution plots that the only currents capable of producing this destructive interference with the driven element currents are those flowing to the ground through the wheels and adjacent regions. The largest current densities existing in the region of the wheels were those shown on the axles and springs. The very complex geometry around the wheels and the finite size of the probing loop prevented a more detailed distribution plot in these regions. It is clear, however, that there must exist vertical components of currents on the vehicle surfaces leading to the wheels, springs, and axles. Displacement currents between the vehicle extremities and the ground plane, and currents along the ground plane beneath these extremities, must also exist. Taking into account the phases, amplitudes, and spacings of the axle currents and the driven element currents, one can obtain a qualitative horizontal plane pattern of the vertically polarized radiation which has the characteristics of the measured pattern. The vehicle body thus seems to behave somewhat as a linear element loaded at its lower extremities. It is apparent, then, that directional effects will occur when the spacing between the currents in the driven element and the currents to ground through these extremities is sufficiently large to produce significant phase differences. These model measurements were made to simulate 44 mc (the lowest frequency of severe destructive interference). The full-scale patterns of the next section indicate that over actual earth the interference is not as severe at this frequency as the model measurements show. The important point demonstrated by the scale model measurements here, however, is that in this frequency range there do exist current distributions on the vehicle similar to those on linear elements, and more or less discrete paths of current flow to the earth. These currents to ground are important in determining the radiation patterns, and their effect on efficiency may be anticipated.

Similarly the measured pattern of the inverted-L monopole may be surmised from the current densities measured on the driven element and the region of the wheels (see Fig. 4). Consider the geometry to be approximated by three point sources in free space as in Fig. 5. The end currents represent the radiation from

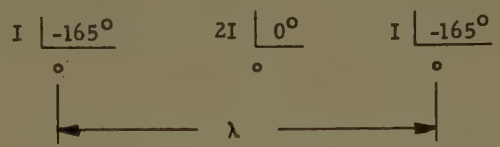

Fig. 5—Point source approximation.

front and rear extremities of the vehicle, while the center point source accounts for the driven element current. A figure-of-eight type pattern with filled-in nulls clearly results from this idealization. This qualitative synthesis is not proposed as a substitute for direct pattern determination. Our choice of the point-source amplitudes, in fact, was prejudiced by the knowledge of deep minima in the radiation pattern. These distributions are of greatest value, however, in revealing the specific surfaces associated with the interference currents. The lowest frequency of major interference is higher than for the whip location, as would be expected with smaller spacings of the driven element and wheel regions. This relatively symmetrical geometry shows also the linear-element behavior of the vehicle. At this frequency the

body is near a wavelength long, and with the excitation employed the phases of the body currents are seen to correspond approximately to those of a self-resonant linear element.

Single-Feed Vertical Monopoles

Consider now the characteristics of a single monopole excited against the $\frac{3}{4}$-ton weapons carrier body, where vertically polarized omnidirectional radiation is desired. The standard whip antenna is a particular case of this single-feedpoint geometry. Radiation patterns for this antenna over the 20–70 mc range are shown in Fig. 6. The vehicle was located on central Ohio clay earth. Note the characteristic minimum discussed in the previous section. Its position and depth are seen to change with frequency. Minima of less importance are also present, and their effects become more pronounced at the higher frequencies. Differences in the grounds and imperfect scaling of the model vehicle tires are offered as reasonable explanations of the discrepancies between model and full scale results. The observed dependence of minima depths on ground conditions is in agreement with this explanation.

To improve the pattern circularity it is necessary to reduce the currents to ground in the wheel regions or to change their relative phase and/or amplitude with respect to the driven element currents so that the destructive interference is diminished. A change in length of the driven monopole or relocation of it are two obviously convenient controls. Fig. 7 shows the results of lengthening the whip antenna with a view toward changing the relative phases and amplitudes of the interfering currents. An improvement is obtained in pattern circularity at the previously discussed critical model frequency. Model pattern measurement at adjacent frequencies and over the entire frequency range showed that this improvement was actual and not merely a shift in the critical frequency. As mentioned before, the frequencies at which destructive interference is critical do not correspond exactly between the full-scale and model measurements. Effects similar to these produced by changing the antenna length on the model, however, should occur with modification of the lengths on the full-scale vehicle at corresponding critical frequencies.

The alternate choice of relocating the monopole was investigated by using an inverted-L radiator symmetrically located with the feed point near the center of the vehicle. This configuration, which fits within the vehicle contours, is shown in Fig. 4. As noted in the previous section, the lowest frequency where destructive interference occurred was raised to 50 mc by this change. Noticeable deviation from acceptable circularity throughout the entire 20–70 mc range was restricted to the region around this critical frequency. The 1/15-scale model patterns are shown in Fig. 8 (opposite). Attempts to improve the relationship between the driven element and lower extremity currents by increasing the length

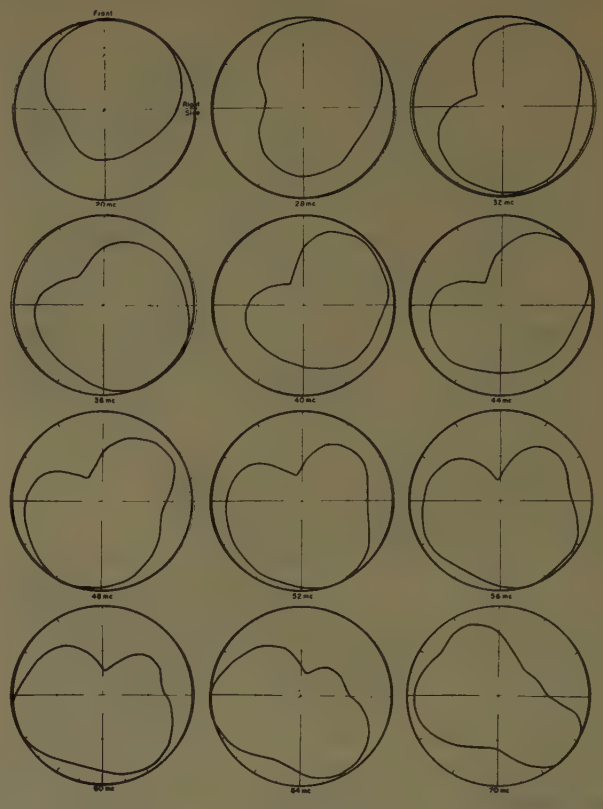

Fig. 6—Horizontal plane radiation patterns for whip antenna (see Fig. 1) on weapons carrier vehicle located over central Ohio clay earth. Vertical polarization.

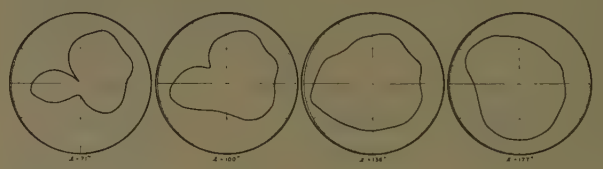

Fig. 7—Horizontal plane radiation patterns for whip antennas on 1/15-scale model weapons carrier over ground plane. 44 mc equivalent full-scale frequency (the frequency of critical interference).

of the monopole resulted in the patterns of Fig. 9. This type of monopole thus shows promise of operating as an effective omnidirectional antenna over a broad frequency band. The improvement was again found to be actual and not merely a small shift in the critical frequency. For the longer monopoles ($l=136$ inches) other frequencies of critical interference were noted above 66 mc. Two or three different lengths would thus be required to produce omnidirectional patterns over the frequency band.

Notice that these results were obtained on a vehicle with considerably modified contours, the most notable of which were removal of the top cab structure and closure of the gap between the cab and rear bed. An additional modification of the lower surfaces of the vehicle showed appreciable effects—all cylindrical elements and gaps (axles, drive shaft, springs, etc.) were bonded to the body resulting in improvements of the patterns of Figs. 3 and 8. The minima were generally

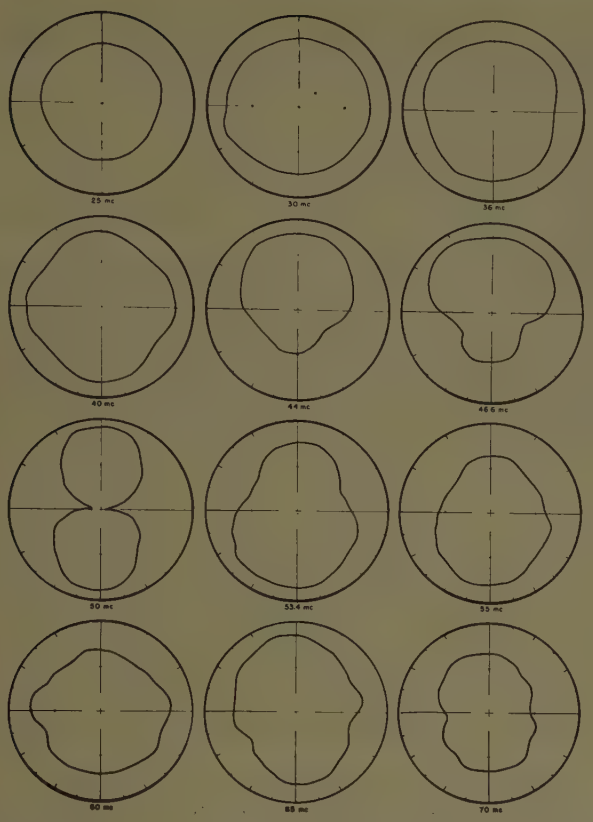

Fig. 8—Horizontal plane radiation patterns for inverted-*L* monopole (Fig. 4) on 1/15-scale model weapons carrier vehicle over ground plane. Equivalent full-scale frequencies.

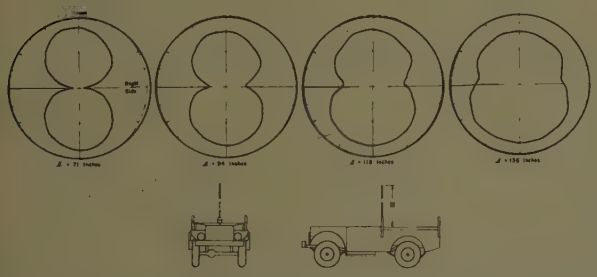

Fig. 9—Horizontal plane radiation patterns for symmetrically located vertical monopole on 1/15-scale model weapons carrier vehicle over ground plane. 49 mc equivalent full-scale frequency (the frequency of critical interference).

filled in and shifted to higher frequencies, but omnidirectional patterns were obtained again only over a portion of the frequency band when the monopoles were restricted to one length. The vehicle in this stripped-down condition corresponded more closely to the idealization of an electrically smooth body, although high current densities were still noted along the outer edges of the body surfaces and on the lower extremities. In the final design of such a monopole or other antenna on this type of vehicle all of these modifications may not be necessary. The changes mentioned, however, were found to have critical effects on radiation patterns of various radiators on the vehicle. Extensive bonding of all joints, gaps, and cylindrical elements separated from the body has proved generally desirable. Behavior of the steering column and adjacent body surface as a resonant circuit producing nulls in the pattern in one instance is an example of the local resonances which must be suppressed in this type of vehicle.

Multiple Feeds

The radiation characteristics shown for vertical monopoles excited at a single feed point indicate that this configuration is at a basic disadvantage. Numerous interference possibilities exist among such a discrete driven element and the various current paths to ground along the bottom of the vehicle. It should be possible to resolve this interference problem by modifying the discreteness of either or both of these current regions.

This solution has not yet been applied to the ground current paths. Mechanical problems are immediately presented in this situation. Extensive bonding of the bottom surfaces is a practicable first step toward redistribution of the ground currents, but it proved to be insufficient with the antennas discussed before. Efficiency and interference considerations, however, make redistribution of ground currents particularly attractive if practicable means can be found to change the bottom surfaces of these vehicles to more symmetrical structures.

Means of "spreading" the feed system and the resulting effects are more obvious. An example of this approach is the structure sketched in Fig. 10. Here all of

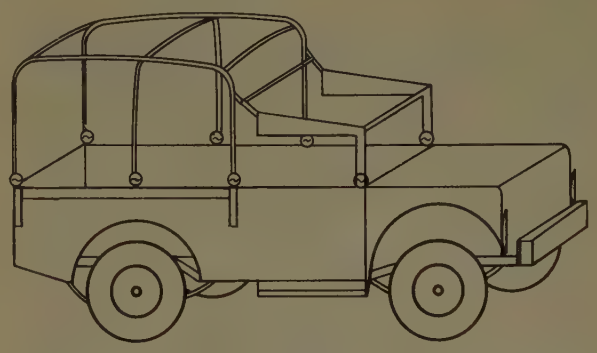

Fig. 10—Sketch of multiply fed "spread" monopole on weapons carrier.

the vehicle contours have been metallized, and the entire top half of the truck is excited uniformly as an extended monopole. The phase difference between the distributed feed currents and currents to ground should be minimized. Radiation patterns obtained for this configuration before and after bonding the lower vehicle surfaces are shown in Figs. 11 and 12. The characteristic figure-of-eight pattern found at 50 mc for both this distributed monopole and the inverted *L* singly-fed monopole is seen to be eliminated here by the lower surface bonding. These patterns do not yet attain the desired omnidirectional qualities over the entire frequency range, but further modification of the vehicle's lower surfaces may extend the pattern bandwidth.

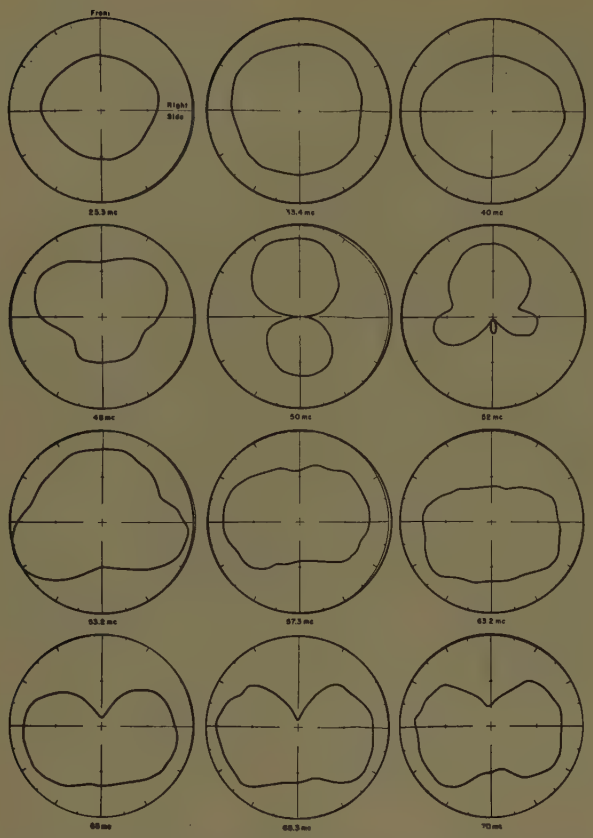

Fig. 11—Horizontal plane radiation patterns for multiply fed monopole (Fig. 10) on 1/15-scale model weapons carrier vehicle over ground plane. Equivalent full-scale frequencies.

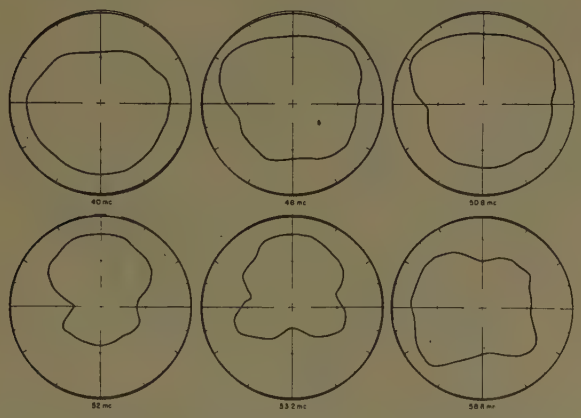

Fig. 12—Patterns for antenna of Fig. 10 continued. Lower extremities of vehicle model extensively bonded to body.

Conclusion

Some aspects of antenna design for ground-based vehicles in the high-frequency range have been discussed In this range, where the vehicle dimensions vary from an appreciable fraction of a wavelength to several wavelengths, current distributions on the vehicle surfaces similar to those of linear elements in free space have been shown to exist. These distributions and their effects on the antenna characteristics were seen to depend on the surface contours of the vehicle, properties of the adjacent earth, and design and location of the driven elements. The only practicable means of predicting antenna behavior of these complex geometries is through systematic measurements of surface current densities, radiation patterns, and impedances for driven elements which appear likely to give the desired properties in the presence of the vehicle body which is considered as an isolated surface with loading corresponding to ground effects.

Omnidirectional horizontal plane patterns were found to be obtainable with a series of vertical monopoles symmetrically located on vehicles modified to approximate an electrically smooth body. Persistence of the omnidirectional property throughout a large frequency band is dependent on control of interference between vertical currents on the monopoles and on the vehicle surface in the regions of favored flow paths to ground. Current paths to ground were shown to be more or less discrete with relatively high densities in the regions of the wheels. Interference between these currents and those of the driven elements is pronounced in some cases. Length and location of the driven elements are convenient controls over these effects. Two alternate systems for reducing this interference problem were suggested:

1) Isolation of the antenna from the vehicle in the higher frequency region by "choke" arrangements to impede the antenna current flow onto the vehicle surfaces.
2) Modification of the lower extremities of the vehicle and use of multiply fed driven elements to destroy the discreteness of the interfering currents.

Patterns obtained with a multiply fed monopole indicate the improvement possible with the latter system.

Modification of the vehicle surfaces was shown to be necessary in certain cases. Presence of the top cab structure and the centrally located gap between the cab and rear bed of the $\frac{3}{4}$-ton army weapons carrier vehicle was particularly detrimental to the omnidirectional characteristics of a symmetrically located vertical monopole. Extensive bonding of the complex lower surfaces (springs, axles, drive shaft, etc.) also produced improvements. All practicable changes in contours to eliminate resonant effects and render the vehicle an electrically smooth symmetrical body are considered generally desirable.

Results of these investigations apply generally to other ground-based vehicles. The basic problem with any radiator excited against the body is the nonsymmetrical nature of the currents to ground. Thus, it is unrealistic, perhaps hopeless, to exclude consideration of the vehicle's lower surfaces and currents to ground from the design of any hf antenna for ground-based vehicles.

Acknowledgment

The author wishes to thank V. Arnold and D. McCoy for their assistance in obtaining the experimental data.

New Method of Antenna Array Synthesis Applied to Generation of Double-Step Patterns*

C. J. SLETTEN†, P. BLACKSMITH, JR.†, AND G. R. FORBES, JR.†

Summary—**A method of synthesizing linear antenna arrays utilizes the natural phase distribution that exists on transmission lines. The far-field pattern function obtained with equispaced elements is decomposed in terms of the feeding coefficients realizable along the feeding guide. Such functions are sufficiently general to permit synthesis of any arbitrary pattern with arbitrary phase. This theory is applied to an asymmetric pattern. The engineering techniques needed to design this pattern are described. Experimental results are in good agreement with the theory.**

Introduction

SEVERAL methods of designing linear antenna arrays for achieving asymmetrical functions such as $\csc^2\theta$ patterns are in use.[1-3] For deriving feeding coefficients that will produce a given power plot, a method developed by Woodward[2] is often applied because the feeding coefficients can be realized on a feeding waveguide. The Woodward technique, however, involves approximating a continuous aperture distribution by means of discrete radiating elements and, since phasing is approximately obtained by varying the space between elements, pattern calculation is difficult.

The method presented here is based on a distribution of discrete radiators whose elements are uniformly spaced about $\lambda_g/4$ apart.[4] For the double-step pattern design described in this paper, almost half of the possible elements can be omitted, leaving most of the spacings $\lambda_g/2$ apart.

Method of Pattern Synthesis

We shall restrict our discussion to a treatment of the problem in one dimension, the θ plane. Fig. 1 shows θ measured from the normal to the array. The radiation pattern produced by a linear array of omnidirectional elements will always have symmetry that is even with respect to the line of the array unless the elements are made directive by a ground screen or some other device.

The required power pattern $E(\theta)\cdot E^*(\theta)$ is specified in the interval $-90°\leq\theta\leq 90°$. We shall assume that individual radiating elements produce identical radiation patterns and the same polarization at each point in space; *i.e.*, $E(\theta)=f(\theta)\hat{E}$, where $\hat{E}$ is a unit vector in the direction of polarization, and the complex function $f(\theta)$ is the scalar function to be generated. The complex function $f(\theta)$ is ordinarily $|f(\theta)|e^{j\gamma(\theta)}$, with the phase function $\gamma(\theta)$ being adjusted for different applications or to simplify design.

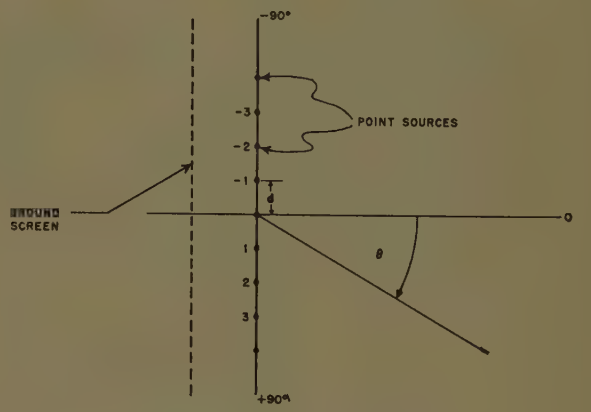

Fig. 1—Linear array with ground screen.

The far-field pattern of a linear array of equally spaced radiators, where the directivity of each element is $D(\theta)$, is given by

$$f(\theta) = D(\theta)\sum_{n=-N}^{n=N} R_n e^{j(\phi_n + nd(2\pi/\lambda)\psi)} \qquad (1)$$

where

R_n is the amplitude of excitation
ϕ_n is the phase of excitation
λ is the wavelength in free space
d is the element spacing
ψ is equal to $\sin\theta$.

Fig. 2 illustrates how $f(\theta)$ can be resolved into component functions that are simply related to phase on the feeding line or guide. On a transmission-line shunt loaded with real admittances at nodes or antinodes in the standing-wave pattern, the phase increases 90° from the feeding end at each successive maximum and minimum of the transmission-line fields. When 180° phase reversal of the radiator is possible, by crossing the leads on a dipole or, as shown here, by placing longitudinal shunt slots on opposite sides of a rectangular waveguide in the TE_{10} mode, the values of $e^{j\phi_n}$ can be 1, -1, j, and $-j$.

In Fig. 2 the phase reference is the slot in the center of the array. The feeding coefficients A_n, B_n, C_n, and D_n

* Manuscript received by the PGAP, February 27, 1956.
† Air Force Cambridge Research Center, Bedford, Mass.

[1] S. A. Schelkunoff, "A mathematical theory of linear arrays," *Bell Sys. Tech. J.*, vol. 22, pp. 80–107; January, 1943.

[2] P. M. Woodward, "A method of calculating the field over a plane aperture required to produce a given polar diagram," *J. IEE*, pt. 111A, vol. 93, pp. 1554–1558; 1946.
P. M. Woodward and J. D. Lawson, "The theoretical precision with which an arbitrary radiation pattern may be obtained from a source of finite size," *J. IEE*, pt. 111, vol. 95, pp. 363–369; September, 1948.

[3] T. T. Taylor and J. R. Whinney, "Applications of potential theory to the design of linear arrays," *J. Appl. Phys.*, vol. 22, pp. 19–29; January, 1951.

[4] C. J. Sletten, P. Blacksmith, Jr., and G. R. Forbes, Jr., "New Method of Antenna Array Synthesis Applied to Generation of Double-Step Patterns," Air Force Cambridge Research Center, AFCRC-TR-55-108; September, 1955.

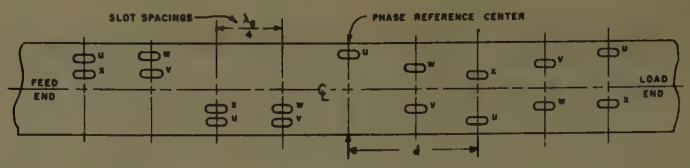

$$f_u = \frac{C_2}{2}e^{-j(2\pi\psi/l)} + \frac{C_1}{2}e^{-j(\pi\psi/l)} + C_0 + \frac{C_1}{2}e^{j(\pi\psi/l)} + \frac{C_2}{2}e^{j(2\pi\psi/l)}$$

$$f_x = \frac{D_2}{2}e^{-j(2\pi\psi/l)} + \frac{D_1}{2}e^{-j(\pi\psi/l)} - \frac{D_1}{2}e^{j(\pi\psi/l)} - \frac{D_2}{2}e^{j(2\pi\psi/l)}$$

$$f_w = -j\frac{A_1}{2}e^{-j(3\pi\psi/2l)} - j\frac{A_0}{2}e^{-j(\pi\psi/2l)} - j\frac{A_0}{2}e^{j(\pi\psi/2l)} - j\frac{A_1}{2}e^{j(3\pi\psi/2l)}$$

$$f_v = -j\frac{B_1}{2}e^{-j(3\pi\psi/2l)} - j\frac{B_0}{2}e^{-j(\pi\psi/2l)} + j\frac{B_0}{2}e^{j(\pi\psi/2l)} + j\frac{B_1}{2}e^{j(3\pi\psi/2l)}$$

$$f_u(\psi) = \sum_{n=0}^{N} C_n \cos\frac{n\pi\psi}{l} \qquad \text{where} \quad l = \frac{\lambda}{2d}$$

$$f_x(\psi) = -j\sum_{n=0}^{N} D_n \sin\frac{n\pi\psi}{l} \qquad \psi = \sin\theta$$

$$f_w(\psi) = -j\sum_{n=0}^{N} A_n \cos\left(n+\frac{1}{2}\right)\frac{\pi\psi}{l} \qquad +j \text{ is } 90^\circ \text{ lead in time}$$

$$f_v(\psi) = \sum_{n=0}^{N} B_n \sin\left(n+\frac{1}{2}\right)\frac{\pi\psi}{l}$$

Fig. 2—Resolution of radiated pattern in terms of phase on transmission line.

are assumed to be real, and are adjustable by the coupling conductance g of the radiator. The phase of the element is obtained from its longitudinal position and its location right or left of the center line. Only the first few elements (terms) are shown, but it is clear that more can be added, in pairs, on the ends of each elementary array. The term under each radiator represents the pattern contribution by that element. Elements are identified and summed to illustrate how they can be combined into four simple sine and cosine series. Each of these four series is in the form of a Fourier series in $\psi = \sin\theta$ in the interval $-l$ to l. It is clear that superimposing the four elemental slot arrays that correspond to the four series will result in longitudinal slot separations of about $\lambda_g/4$ where λ_g is the guide wavelength.

Any ideal required pattern $f(\theta)$ can be decomposed into even and odd parts since electromagnetic fields are linear and can be superposed on one another. Hence

$$f(\theta)_{\text{ideal}} = [f_{\text{real,even}}(\theta) + f_{\text{real,odd}}(\theta)] + j[f_{\text{imag,even}}(\theta) + f_{\text{imag,odd}}(\theta)] \quad (2)$$

$$f_{\text{even}} = \tfrac{1}{2}[f(\theta) + f(-\theta)]; \quad f_{\text{odd}} = \tfrac{1}{2}[f(\theta) - f(-\theta)]. \quad (3)$$

We can let

$$f_{r,e}(\theta) = f_u(\psi) = \sum_{n=0}^{n=N} C_n \cos\frac{n\pi\psi}{l} \quad (4)$$

$$f_{r,o}(\theta) = f_v(\psi) = \sum_{n=0}^{n=N} B_n \sin\left(n+\frac{1}{2}\right)\frac{\pi\psi}{l} \quad (5)$$

$$f_{i,e}(\theta) = jf_w(\psi) = \sum_{n=0}^{n=N} A_n \cos\left(n+\frac{1}{2}\right)\frac{\pi\psi}{l} \quad (6)$$

$$f_{i,o}(\theta) = jf_x(\psi) = \sum_{n=0}^{n=N} D_n \sin\frac{n\pi\psi}{l}. \quad (7)$$

The degree of approximation to $f(\theta)$, of course, wil depend on the number of terms in the series, that is, on the number of radiators used. Of the various types of approximations that could be used over the interval $-l$ to l, approximation in the least square sense is the most convenient. For this type of approximation the coefficients A_n, B_n, C_n, and D_n are merely Fourier coefficients for which we have the following explicit formulas:

$$A_n = \frac{1}{l}\int_{-l}^{l} f_{i,e}(\theta)\cos\left(n+\frac{1}{2}\right)\frac{\pi\psi}{l}\,d\psi,$$

$$B_n = \frac{1}{l}\int_{-l}^{l} f_{r,o}(\theta)\sin\left(n+\frac{1}{2}\right)\frac{\pi\psi}{l}\,d\psi,$$

$$C_n = \frac{1}{l}\int_{-l}^{l} f_{r,e}(\theta)\cos\frac{n\pi\psi}{l}\,d\psi,$$

$$D_n = \frac{1}{l}\int_{-l}^{l} f_{i,o}(\theta)\sin\frac{n\pi\psi}{l}\,d\psi.$$

To check orthogonality, we note that

$$I = \int_{-l}^{l} \cos\frac{(n+\frac{1}{2})\pi\psi}{l}\left\{\begin{matrix}\sin\dfrac{(m+\frac{1}{2})\pi\psi}{l}\\ \cos\dfrac{(m+\frac{1}{2})\pi\psi}{l}\end{matrix}\right\}d\psi = 0, \qquad m \neq n.$$

It is evident that this decomposition is sufficient to approximate any arbitrary pattern $f(\theta)$ in the least square sense.

We have developed $f(\theta)$ in a least square approximation in $\psi = \sin\theta$. If we want a least square approximation in θ we must evaluate a system of equations where integrals like

$$C\int_{\sin^{-1}-l}^{\sin^{-1}l} f(\theta)\sin\left[\frac{n\pi}{l}\sin\theta\right]d\theta$$

are typical. These can usually be expressed in Bessel or Struve functions when $f(\theta)$ is simple.

Only when $l=1$ or $d=\lambda/2$ will the expansion interval agree with the physical interval $-\pi/2\leq\theta\leq\pi/2$. When $l>1$, $d<\lambda/2$, part of $f(\theta)$ will not be visible. When $l<1$, $d>\lambda/2$, $f(\theta)$ will start repeating when $\theta=\sin^{-1}l$, and this will generally be the case when slotted waveguide is used.

Application of Method to the Double-Step Function

Our experimental efforts have been limited to generating the ideal function shown in Fig. 3. We have used both waveguide and two-wire line-feeding systems. For most of the work presented here we used 1/16-inch slots on 1 inch by $\frac{1}{2}$ inch waveguide, at a wavelength of 3.2 cm. The double-step function was selected because it minimized the number of $\lambda_g/4$ spaced elements and their resulting mutual couplings.

The pattern in Fig. 3 can be approximated by a cosine symmetric main lobe and a step function on one side of the $\theta=0$ axis. To simplify the design we let $f_w(\theta)$ produce the main lobe and let a combination of $f_v(\theta)$ and $f_u(\theta)$ produce the step function. We thereby obtain the odd and even patterns in phase quadrature where they do not destructively interfere with each other.

As a first step, suppose we make f_v produce an odd function as shown in Fig. 4. Then

$$f_v=\sum_{n=0}^{n=N}B_n\sin\left(n+\frac{1}{2}\right)\frac{\pi\psi}{l}\,d\psi,$$

$$B_n=\frac{1}{l}\int_{-l}^{0}-\frac{1}{2}\sin\left(n+\frac{1}{2}\right)\frac{\pi\psi}{l}\,d\psi$$

$$+\frac{1}{l}\int_{0}^{l}\frac{1}{2}\sin\left(n+\frac{1}{2}\right)\frac{\pi\psi}{l}\,d\psi=\frac{1}{(n+\frac{1}{2})\psi}\cdot \quad (8)$$

$$n=0 \quad B_0=2/\pi=0.6366$$
$$n=1 \quad B_1=2/3\pi=0.2122$$
$$n=2 \quad B_2=2/5\pi=0.1273$$
$$n=3 \quad B_3=2/7\pi=0.09095.$$

Note that when $f_u(\psi)$ generates a constant function equal to $\frac{1}{2}$, the series reduces to one term, $C_0=\frac{1}{2}$.

Now, to produce a step function of unity amplitude in the interval between $0\leq\theta\leq\pi/2$ and approximately zero in the interval $-\pi/2\leq\theta\leq0$, we can write for the first seven radiators:

$$f_{\text{step}}=f_v+f_u=0.5+0.637\sin\frac{k\pi\psi}{2}+0.212\sin\frac{3k\pi\psi}{2}$$

$$+0.127\sin\frac{5k\pi\psi}{2} \quad (9)$$

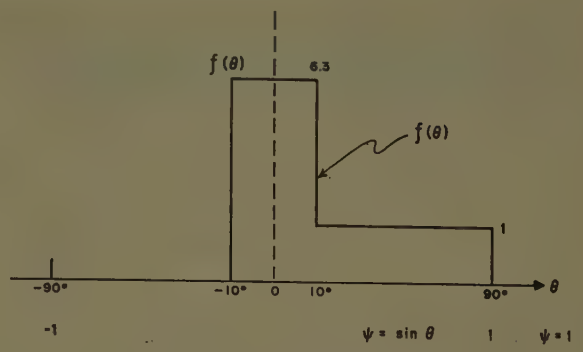

Fig. 3—Ideal field pattern.

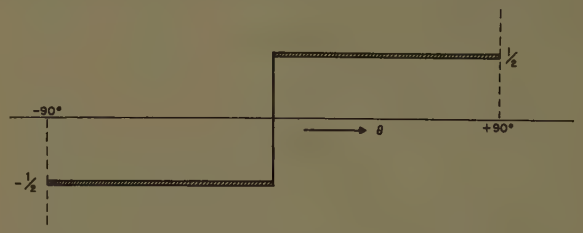

Fig. 4—Desired characteristics of odd function.

where $k=2d/\lambda$ and $d=\lambda g/2$. The first slots on each side of the phase reference center are spaced $\lambda_g/4$, and all other slots are spaced $\lambda_g/2$.

The peak quadrature pattern can be derived by using Tchebycheff coefficients to get low side lobes. We computed these and for a 32-db side lobe level obtained

$$A_0=3.755; \quad A_1=2.502; \quad \text{and} \quad A_2=1.000.$$

These values result in an equation of the form

$$f_w(\psi)=3.775\cos\frac{k\pi\psi}{2}+2.502\cos\frac{3k\pi\psi}{2}+1.000\cos\frac{5k\pi\psi}{2}.$$

Since the peak value of the pattern is to be 16 db above the step function, the coefficients for $f_w(\psi)$ have to be modified by a multiplicative constant. By setting $\psi=0$ in $f_w(\psi)$ and adjusting the sum at 6.3, we get the desired 16 db above the 1.0 value of the function $f_{\text{step}}(\psi)$. The resulting equation for $f_w(\psi)$ is then

$$f_w(\psi)=3.259\cos\frac{k\pi\psi}{2}+2.170\cos\frac{3k\pi\psi}{2}+0.868\cos\frac{5k\pi\psi}{2}.$$

We now calculate the field (E) and power (P) excitation for the final array (see Table I). With the distribution given in Table I, the patterns of the individual

TABLE I

Field and Power Excitation of Double-Step Array

Slot No.	Step E_{rad}	Peak E_{rad}	Relative	
			Total E_{rad}	P_{rad}
1	−0.0636	0.434	0.370	0.137
2	−0.1061	1.085	0.979	0.860
3	−0.3183	1.625	1.307	1.708
4	0.5000	—	0.500	0.250
5	0.3183	1.625	1.943	3.775
6	0.1061	1.085	1.191	1.418
7	0.0636	0.434	0.498	0.248

radiating elements combine to produce the total field:

$$f_t(\psi) = D(\theta)\left[0.500 + 0.637 \sin\frac{k\pi\psi}{2} + 0.212 \sin\frac{3k\pi\psi}{2} + 0.127 \sin\frac{5k\pi\psi}{2} + j\left(3.259 \cos\frac{k\pi\psi}{2} + 2.170 \cos\frac{3k\pi\psi}{2} + 0.868 \cos\frac{5k\pi\psi}{2}\right)\right] \quad (10)$$

where $D(\theta)$ is the pattern in the θ plane of the individually radiating elements, and $\psi = \sin\theta$. For more effective coupling in the actual array, the slot spacings were reduced so that

$$d = 0.9\lambda_g/2$$

and

$$k = \frac{0.9\lambda_g}{\lambda} = 1.26.$$

A theoretical plot of the function is shown in Fig. 5 with $D(\theta) = 1$. Fig. 6 identifies the slots and shows their positions.

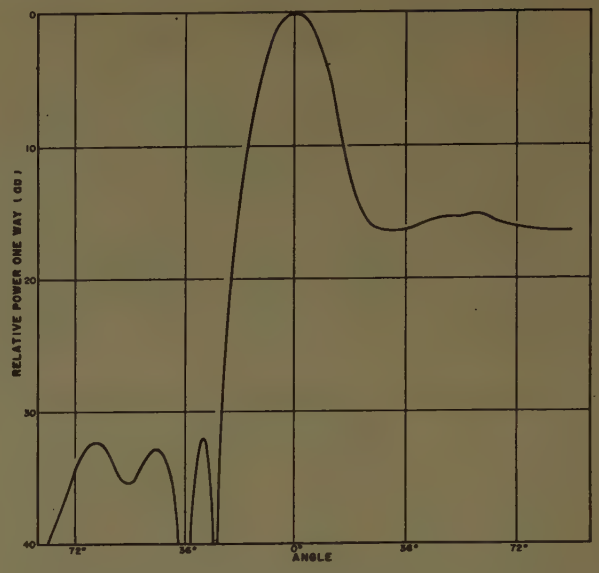

Fig. 5—Theoretical pattern of seven-slot array double-step function with $D(\theta) = 0.45\ \lambda_g$ spacing.

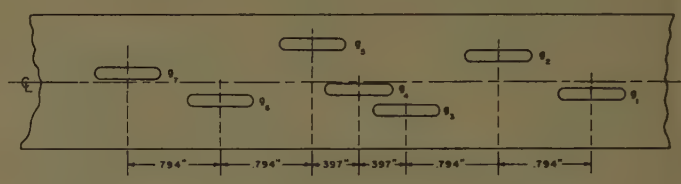

No.	g	Coupling	Slot Disp. (in.)	Slot Length (in.)	Slot Width (in.)	Remarks
g_1	0.0457	0.1953db	0.0630	0.621	0.0625	load end
g_2	0.3250	1.2222db	0.1360	0.627	0.0625	
g_3	0.5170	1.8099db	0.1980	0.632	0.0625	
g_4	0.0249	0.1072db	0.0480	0.620	0.0625	
g_5	0.8070	2.5696db	0.2580	0.637	0.0625	
g_6	0.1850	0.7372db	0.1160	0.625	0.0625	
g_7	0.0240	0.1030db	0.0475	0.620	0.0625	feed end

Fig. 6—Slot location of seven-slot array double-step function with 0.45 λ_g spacing and matched load, $\lambda = 3.2$ cm.

Method of Determining Slot Couplings

Several difficulties hinder realization of the desired feeding coefficients. First we must have room to accommodate slot no. 4 (see Fig. 6) without having to cut into slots no. 3 and no. 5. This is easy since slot no. 4 is coupled low enough to be cut beside either no. 3 or no. 5, regardless of the type of load at the terminal of the array. Slot no. 5, however, couples considerably more power than the other elements. We must be careful to achieve its relative power of 3.775 because realizable values of slot conductance g are less than 1.0. The gain of the array will be reduced if we dissipate enough power in a matched load to reduce all the couplings. It is a simple matter to find the values of g_n if we assume a matched terminal load and no reflected power at any slot. This is a good approximation on multislot arrays where individual couplings are low but a more general approach is necessary when the power to be coupled is large and the number of slots to do the job is small. Our design formulation must be general enough to allow for a change in frequency, which makes the slots reactive and effectively changes the slot spacings.

General Procedure

The general procedure (see Fig. 7) for finding the value of the nth slot admittance (y_n) is to determine the total admittance ($y_{L_{n-1}}$) at the position of the preceding radiator (aa') and reflect this admittance to position bb', by using the following expression for normalized values:

$$y_{n\,\text{in}} = \frac{y_{L_{n-1}} + j\tan\beta h}{1 + jy_{L_{n-1}}\tan\beta h}.$$

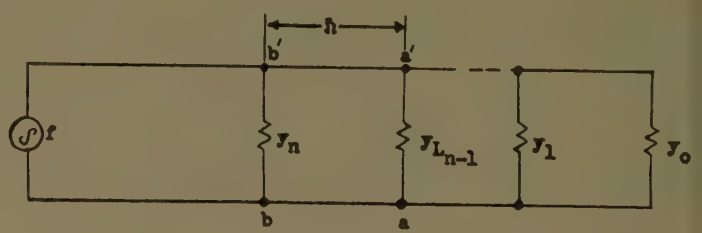

Fig. 7.

$\beta = 2\pi/\lambda_g$, h is distance between shunt elements, and the subscript *in* means the admittance looking toward the right before y_n is added. The power dissipated in y_n is

$$P_n = E^2 g_n.$$

The power dissipated to the right of y_n is

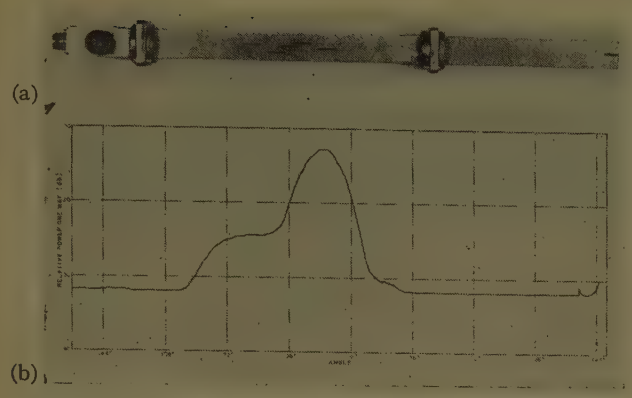

Fig. 8—(a) Five-slot array with 50 per cent of the power going into the matched load. (b) Pattern of five-slot array.

$$\sum_{i=0}^{n-1} P_i = E^2 g_{n\text{ in}}.$$

Eliminating E^2 we see

$$\frac{g_n}{g_{n\text{ in}}} = \frac{P_n}{\sum_{i=0}^{n-1} P_i}.$$

This procedure can be started at the load end of the array and repeated until all the values g_n are found. The computation of g_{in} at each junction is simplified by the use of a Smith chart.

Experimental Results

In our study of the loading problem it was seen that a short at $\lambda_g/4$ from slot no. 1 tends to establish all slots except no. 4 in regions of relatively low guide conductance. This gives maximum radiated power with minimum slot conductance (small transverse slot displacement) on the highly coupled slots but throws slot no. 4 into a region of maximum slot conductance so that its phasing in relation to the rest of the array becomes more critical. Several such models tested gave poor pattern results. A five-slot array with resonant spacings and matched load absorbing about 50 per cent of the input power produced the pattern shown in Fig. 8. Although patterns were best at $\lambda = 3.4$ cm instead of at $\lambda = 3.2$ cm, they were fairly good over a wide band of frequencies.

In order to obtain a beamwidth of approximately 20° and deliver a relatively small fraction of the power in the matched load, an array was constructed to the following specifications. A matched load was used but the spacings were $0.225\lambda_g$ and $0.45\lambda_g$. This placed slot no. 5 in a region of lower slot conductance where it was possible to get high power out of it. Fig. 9 is a photograph of the array, and Fig. 6 is a diagram of the slot locations. Fig. 10 shows the patterns obtained experimentally at $\lambda = 3.2$ cm. The agreement with the calculated pattern in Fig. 5 is good.

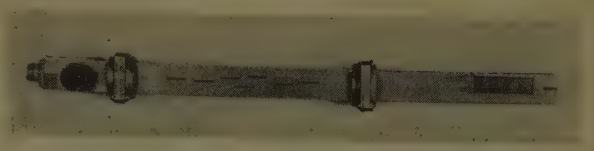

Fig. 9—Seven-slot array for double-step function.

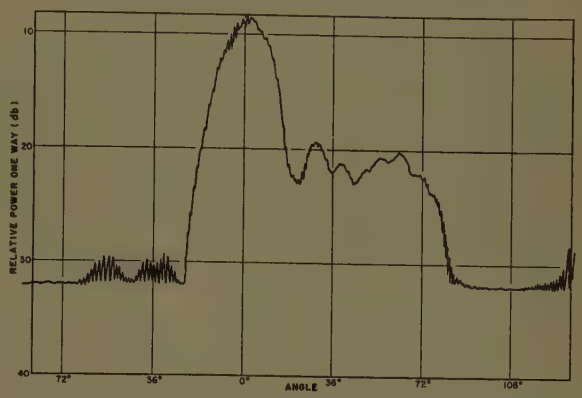

Fig. 10—*H* plane of seven-slot array with matched load on the end, 0.45 λ_g spacing.

Discussion

An important consequence of this method of array synthesis is that arbitrary patterns can be achieved by varying the amplitude of radiations at each element while maintaining fixed phase relationships between radiators.

The synthesis of complex antenna patterns by a method that utilizes the properties of transmission lines admittedly presents experimental difficulties. But these same difficulties exist in any method of pattern synthesis used to determine power and phase distribution on an array. Our method requires uniform spacings of approximately $\lambda_g/4$. The bandwidth will probably be less than with arrays having $\lambda_g/2$ spacing although experimental results indicate that 10 per cent bandwidths can be achieved.

Mutual couplings between elements create the biggest problem in realizing feeding coefficients. It is known that the curve for intercouplings between parallel electric dipoles monotonically decreases as the spacing increases.[5] Conditions at $\lambda_g/4$ are not much worse than those at $\lambda_g/2$, and it seems plausible that suitable corner reflectors behind the radiating dipoles would diminish exterior couplings.

We believe that a joint experimental and theoretical attack on the combined problem of both the exterior radiation couplings and the interior transmission line couplings will produce solutions that will enable us to maintain precise control of the radiation pattern.[6]

[5] R. W. P. King, H. R. Mimno, and A. H. Wing, "Transmission Lines, Antennas, and Waveguides," McGraw-Hill Book Co., Inc., New York, N. Y., p. 125; 1945.

[6] B. J. Starkey and E. Fitch, "Mutual impedance and self-impedance of coupled parallel aerials," *J. IEE*, pt. 111, vol. 97, pp. 129–137; May, 1950.

Convergent Representations for the Radiation Fields from Slots in Large Circular Cylinders*

L. L. BAILIN† AND R. J. SPELLMIRE‡

Summary—**Expressions are derived which will approximate the radiation fields from slots in large circular cylinders. This derivation is accomplished by applying a Watson transformation to the slowly convergent harmonic series representation and then evaluating the resulting integral to third order with the techniques of Van der Pol and Bremmer. Highly convergent representations are obtained which are valid in different azimuthal sectors around cylinders where *ka* is in the range of 10 to 1000 or more.**

I. Introduction

IT WAS pointed out in a recent report by Sensiper[1] and by others[2] that cylindrical wave representations in terms of harmonic components had very limited applicability in the case of large cylinders. The reason for this limitation upon the applicability of the harmonic representation is contained in the fact that these representations are slowly convergent series as functions of ka where $k=2\pi/\lambda$ and a is the radius of the cylinder.

The basis for this present study of more convergent representations has been described by Van der Pol and Bremmer[3] in their classic studies of terrestrial radio waves. Sensiper[1] applied their techniques to cylindrical waves and investigated the radiation fields from both axial and circumferential slots in large cylinders (see Fig. 1 for geometry). However, the mathematical techniques described therein may be applied with slight modifications to the analogous dipole and scattering problems. In the principal plane, $\theta=\pi/2$, he derived the second-order approximations (sometimes referred to as the geometrical optics representations) in the so-called optically illuminated region where the azimuthal angle $\phi<\pi/2$, and the residue series representation in the shadow region where $\pi\geq\phi>\pi/2$. Although these second-order results would prove to be adequate when compared with the harmonic series representation of the fields from slots on cylinders where $ka=100$, they would deviate noticeably for smaller values of ka or for the fields off the principal plane which depend on $ka\sin\theta$. Consequently, more accurate third-order results would be immediately useful in the calculation of element factors for linear slot arrays in a range of ka which is currently practical. These results would also be useful for a complete description of the three-dimensional field.

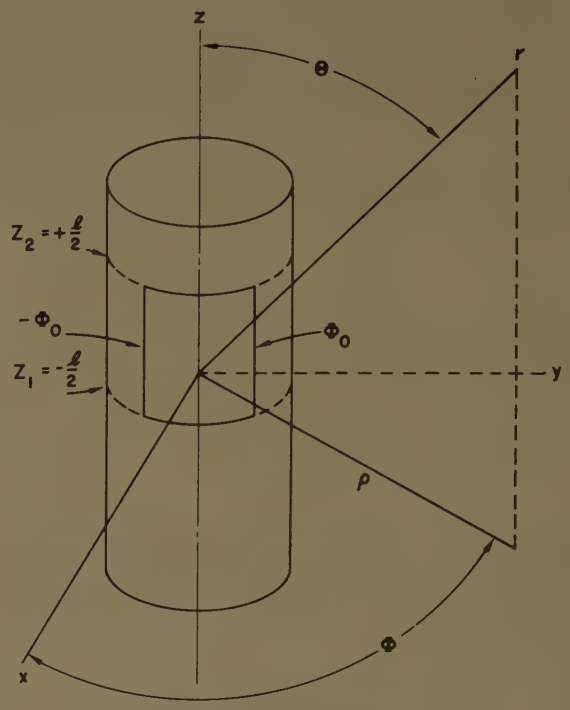

Fig. 1—Geometry of the cylinder and slot.

The general method to be used in the derivation of the third-order approximations will be to choose the principal plane so as to simplify the geometry to two dimensions (r, ϕ) (this method was used by Sensiper *et al.*[1]). This simplification is not, however, an essential feature of the procedure. The three-dimensional behavior can be obtained by replacing ka with $ka\sin\theta$ whenever it appears in the argument of a Hankel function and multiplying by a factor which is a function of θ only. Detailed descriptions of slot shapes, methods of excitation, and all but the principal field component are nonessential to this study. For instance, the convergence difficulties encountered in the cross-polarized component of the radiation field from arbitrarily shaped slots on large cylinders[4] are the same as those described in Section III

* Manuscript received by the PGAP, July 7, 1956; revised manuscript received, June 28, 1957. The work described in this report was sponsored by the Air Force Cambridge Research Center under Contract AF19(604)-262, Change C. Much of the material discussed was presented at the URSI Symposium on Electromagnetic Wave Theory, University of Michigan, Ann Arbor, Mich.; June, 1955.

† Dept. of Elec. Eng., Univ. of Southern Calif., Los Angeles, Calif.; formerly at Hughes Aircraft Co., Culver City, Calif.

‡ Hughes Aircraft Co., Culver City, Calif.

[1] S. Sensiper, W. G. Sterns, and T. T. Taylor, "A further study of the pattern of single slots on circular conducting cylinders," presented at Joint URSI-IRE Convention, NBS, Wahsington, D. C.; April, 1952.

S. Sensiper, "Cylindrical radio waves," IRE TRANS., vol. AP-5, pp. 56–70; January, 1957.

[2] W. Franz and K. Depperman, "Theories der beugung am zylinder unter berücksichtigung der kriechwelle," *Ann. Phys.*, vol. 10, pp. 361–373; 1952.

W. Franz, "On the Green's functions of the cylinder and the sphere," *Z. Natur.*, vol. 9a, pp. 705–716; September, 1954.

I. Imai, "The diffraction of electromagnetic waves by a circular cylinder," *Z. Phys.*, vol. 137, pp. 31–48; 1954.

[3] B. Van der Pol and H. Bremmer, "The diffraction of electromagnetic waves from an electrical point source round a finitely conducting sphere," *Phil. Mag.*, vol. 24, pp. 141–176; July, 1937. Also see H. Bremmer, "Terrestrial Radio Waves," Elsevier Press, Inc., New York, N. Y.; 1949.

[4] S. Silver and W. K. Saunders, "The radiation from a transverse rectangular slot in a circular cylinder," *J. Appl. Phys.*, vol. 21, pp. 745–749; August, 1950.

for the narrow half-wavelength axial slot. Thus, this paper will be concerned primarily with the principal components of half-wavelength delta slots which are parallel and perpendicular to the axis of a large cylinder. By an appropriate superposition of these results, the radiation characteristics of an arbitrary slot may be found.

II. Circumferential Slot

It can be shown[4,5] that in the principal plane the main component of the radiation characteristics from a narrow circumferential slot may be derived entirely from the electric Hertz vector given by

$$\Pi_z = K \sum_{n=-\infty}^{\infty} \frac{H_n^{(2)}(kr)}{H_n^{(2)}(ka)} \exp\left[-jn\phi\right] S(n, \phi_0) \qquad (1)$$

where $K = |E_0|/2\phi_0 k^2$ ($|E_0|$ = maximum electric field strength of a center-fed slot), and the function $S(n, \phi_0)$ depends on the source characteristics. For example, the source function for a half-wavelength ($\phi_0 = \pi/2ka$) delta slot ($l \to 0$) excited by a sinusoidal field $E(\phi) = E_0 \cos(ka\phi)$ is (see Bailin[6])

$$S(n, \phi_0) = \frac{(ka)^2 \cos\left(\frac{n\pi}{2ka}\right)}{(ka)^2 - n^2}.$$

Eq. (1) leads to the harmonic representation for the radiation fields in the principal plane. It may be modified to include the behavior of the fields off the principal plane by multiplying by $(1/\sin\theta)$ and inserting $ka \sin\theta$ as the argument of the Hankel function in the denominator. Such modifications, however, will not affect the general procedure which follows.

When the technique of Van der Pol and Bremmer[3] is used, the summation in (1) is converted to an integral by a Watson[7] transformation. Eq. (1) becomes

$$\Pi_z = \frac{K}{2j} \int_{C_1} S(\nu, \phi_0) \frac{H_\nu^{(2)}(kr) \exp\left[j\nu(\pi - \phi)\right]}{H_\nu^{(2)}(ka) \sin \nu\pi} d\nu \qquad (2)$$

where C_1 is as shown in Fig. 2. The value of this integral may be obtained in three different ways. If the integral is evaluated from the residues at the poles $\nu = n$ for $n = 0, \pm 1, \pm 2, \pm 3, \cdots$ then (2) yields the harmonic representation of (1). However, if the integral is evaluated at the poles determined from $H_\nu^{(2)}(ka) = 0$, then the residue series representation which will be discussed in Part B is obtained. The third possibility is to evaluate the integral along the path C_1 without recourse to the theory of residues. This method will lead to the geometrical optics results.

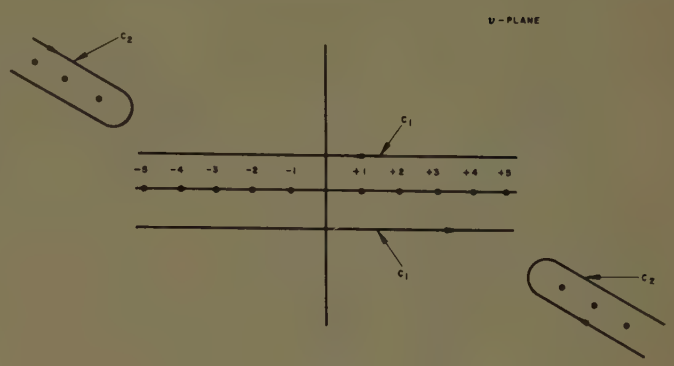

Fig. 2—ν plane with contours C_1 and C_2.

A. Third Order Geometrical Optics Representation ($|\phi| < \pi/2$)

To obtain the geometrical optics results, the contour C_1 of Fig. 2 was considered and the integrals modified as follows: since in the upper half-plane

$$\frac{1}{\sin \nu\pi} = -2j \sum_{m=0}^{\infty} \exp\left[j\nu(2m+1)\pi\right],$$

and in the lower half-plane

$$\frac{1}{\sin \nu\pi} = 2j \sum_{m=0}^{\infty} \exp\left[-j\nu(2m+1)\pi\right],$$

(2) can be written as

$$\Pi_z = K \sum_{m=0}^{\infty} \left[\begin{array}{l} \displaystyle\int_{-\infty+je}^{\infty+je} S(\nu, \phi_0) \frac{H_\nu^{(2)}(kr) H_\nu^{(1)}(ka)}{H_\nu^{(2)}(ka) H_\nu^{(1)}(ka)} \exp\left(j\nu[2(m+1)\pi - \phi]\right) d\nu \\ + \displaystyle\int_{-\infty-je}^{\infty-je} S(\nu, \phi_0) \frac{H_\nu^{(2)}(kr) H_\nu^{(1)}(ka)}{H_\nu^{(2)}(ka) H_\nu^{(1)}(ka)} \exp\left(-j\nu[2m\pi + \phi]\right) d\nu \end{array} \right] \qquad (3)$$

where the factor $H_\nu^{(1)}(ka)/H_\nu^{(1)}(ka)$ makes the denominators real and nonexponential for large ka. To obtain the geometrical optics approximation, the Hankel functions in the numerators are replaced by their Sommerfeld integral representations:

$$H_\nu^{(1)}(z) = \frac{1}{\pi} \int_{\eta - j\infty}^{-\eta + j\infty} \exp\left[jz \cos\tau_1 + j\nu(\tau_1 - \pi/2)\right] d\tau_1$$

and

$$H_\nu^{(2)}(z) = \frac{1}{\pi} \int_{-\pi+\eta-j\infty}^{\pi-\eta+j\infty} \exp\left[-jz \cos\tau_2 - j\nu(\tau_2 - \pi/2)\right] d\tau_2$$

where $-\arg z < \eta < \pi - \arg z$. When these equations are inserted into (3), the result in terms of amplitude and phase functions is

[5] L. L. Bailin and R. J. Spellmire, "Convergent Representation for the Radiation Fields from Slots in Large Circular Cylinders," Tech. Memo. No. 386, Hughes Aircraft Co. Res. Labs., Culver City, Calif., July, 1955. This report is an expanded version of the present paper and contains many of the details omitted here.

[6] L. L. Bailin, "Radiation field produced by a slot in large circular cylinders," IRE Trans., vol. AP-3, pp. 127–137; July, 1955.

[7] G. N. Watson, "The diffraction of radio waves by the earth," *Proc. Roy. Soc.*, London, vol. A., 95, pp. 83–99; 1918, and vol. A., 95, pp. 546–563; 1919.

$$\Pi_z = -\frac{K}{\pi^2}\sum_{m=0}^{\infty}\left[\int_{-\infty+je}^{\infty+je}\frac{S(\nu,\phi_0)d\nu}{H_\nu^{(2)}(ka)H_\nu^{(1)}(ka)}\int_{\eta-j\infty}^{-\eta+j\infty}d\tau_1\int_{-\pi+\eta-j\infty}^{\pi-\eta+j\infty}d\tau_2\exp\left[jS_m^{+}\right]\right.$$
$$\left.+\int_{-\infty-je}^{\infty-je}\frac{S(\nu,\phi_0)d\nu}{H_\nu^{(2)}(ka)H_\nu^{(1)}(ka)}\int_{\eta-j\infty}^{-\eta+j\infty}d\tau_3\int_{-\pi+\eta-j\infty}^{\pi-\eta+j\infty}d\tau_4\exp\left[jS_m^{-}\right]\right] \quad (4)$$

where

$$S_m^{+} = -kr\cos\tau_2 + ka\cos\tau_1 + \nu[2(m+1)\pi - \phi + (\tau_1-\tau_2)]$$

and

$$S_m^{-} = -kr\cos\tau_4 + ka\cos\tau_3 + \nu[-2m\pi - \phi + (\tau_3-\tau_4)].$$

Only the $m=0$ wave is considered, since, as Bremmer[3] points out, the $m\neq 0$ terms correspond to waves reflected from infinity and are small compared with the $m=0$ terms. It is shown[1] by a consideration of the saddle points in (4), that the integral with phase factor S_0^{+} corresponds to rays reaching the point of observation in the region of space where $2\pi\geq\phi>3\pi/2$ and that the integral with phase factor S_0^{-} corresponds to rays reaching the observation point located in the region of space where $\pi/2>\phi\geq 0$. If the source is symmetrical about $\phi=0$, then these two integrals should yield the same result for symmetrically located observation points.

Thus, to obtain the desired third-order approximation for $\pi/2>\phi\geq 0$, the second term in (4) is considered

$$\Pi_z = -\frac{K}{\pi^2}\int_{-\infty-je}^{\infty-je}\frac{S(\nu,\phi_0)d\nu}{H_\nu^{(2)}(ka)H_\nu^{(1)}(ka)}\cdot\int_{\eta-j\infty}^{-\eta+j\infty}d\tau_3\int_{\pi+\eta-j\infty}^{\pi-\eta+j\infty}d\tau_4\exp\left[jS_0^{-}\right] \quad (5)$$

and the function S_0^{-} is expanded in a Taylor series to third order in τ_3, τ_4, and ν. It can be shown[4] that the resulting integrals may be evaluated by saddle point methods to yield a far field result valid for large ka or small ϕ. Thus, (5) becomes

$$\Pi_z = 2KS(ka\sin\phi,\phi_0)\frac{\exp[-j(kr-\pi/4)]}{(kr)^{1/2}}\cdot\frac{(ka\cos\phi)Z^{1/2}H_{1/3}^{(1)}(Z)\exp\left[j\left(ka\cos\phi - Z + \frac{5\pi}{12}\right)\right]}{ZH_{1/3}^{(1)}(Z)H_{1/3}^{(2)}(Z)} \quad (6)$$

and is valid where

$$Z = \frac{ka\cos^3\phi}{3\sin^2\phi}$$

is large. Since $E_z = k^2\Pi_z$ and the form factor for a half-wavelength delta slot is given by

$$S(ka\sin\phi,\phi_0) = \frac{\cos(\pi/2\sin\phi)}{\cos^2\phi},$$

(6) becomes

$$E_z = k^2K2(ka)\left[\frac{\cos(\pi/2\sin\phi)}{\cos\phi}\right]\left[\frac{\exp -j(kr-\pi/4)}{(kr)^{1/2}}\right]\cdot\frac{Z^{1/2}H_{1/3}^{(1)}(Z)\exp\left[j\left(ka\cos\phi - Z + \frac{5\pi}{12}\right)\right]}{ZH_{1/3}^{(1)}(Z)H_{1/3}^{(2)}(Z)} \quad (7)$$

which is the principal component of the radiation field E_θ at $\theta=\pi/2$.

Eq. (7) is now the third-order geometrical optics results which should agree precisely with the second-order results as $\phi\to 0$. When $\phi\to 0$, $Z\to\infty$ and the potential tends to

$$\Pi_z = 2K\frac{\exp[-j(kr-\pi/4)]}{(kr)^{1/2}}\cdot\frac{\exp[jka\cos\phi]}{(2/\pi)^{1/2}}ka\cos\phi\,S(ka\sin\phi,\phi_0) \quad (8)$$

which leads to the second-order result[1] given by

$$E_z = k^2K(2\pi)^{1/2}ka\left[\frac{\cos(\pi/2\sin\phi)}{\cos\phi}\right]\cdot\exp[j(ka\cos\phi)]\frac{\exp[-j(kr-\pi/4)]}{(kr)^{1/2}}. \quad (9)$$

To check the accuracy of the third-order representation from (7) and the second-order values given by (9), the far field harmonic series result for the half-wave slot can be obtained from (1) and the asymptotic behavior of $H_n^{(2)}(kr)$ as

$$E_z = k^2K\left(\frac{2}{\pi}\right)^{1/2}(ka)^2\frac{\exp[-j(kr-\pi/4)]}{(kr)^{1/2}}\cdot\sum_{n=-\infty}^{\infty}\exp[jn\pi/2]\frac{\cos\frac{n\pi}{2ka}\exp[-jn\phi]}{[(ka)^2-n^2]H_n^{(2)}(ka)}. \quad (10)$$

If the common factors are canceled from (7), (9), and (10) and if they are all renormalized so that the coefficient of the series in (10) is unity, then the geometrical optics approximations are

$$E_z \sim \frac{\sqrt{2\pi}}{ka}\left[\frac{\cos(\pi/2 \sin\phi)}{\cos\phi}\right] \cdot \frac{Z^{1/2}H_{1/3}^{(1)}(Z)\exp\left[j\left(ka\cos\phi - Z + \frac{5\pi}{12}\right)\right]}{ZH_{1/3}^{(1)}(Z)H_{1/3}^{(2)}(Z)} \quad (11)$$

to third order.

$$E_z \sim \left[\frac{\pi}{ka}\right]\frac{\cos(\pi/2 \sin\phi)}{\cos\phi}\exp[j\,ka\cos\phi] \quad (12)$$

to second order, and of course the harmonic series becomes

$$E_z \sim \sum_{n=-\infty}^{\infty} \frac{\exp[jn\pi/2 - jn\phi]}{H_n^{(2)}(ka)} \frac{\cos\frac{n\pi}{2ka}}{[(ka)^2 - n^2]} \quad (13)$$

which are the results tabulated by Bailin[6] for the principal H plane ($\theta = 90°$).

Fig. 3 shows a numerical comparison for $ka = 12$ of the second- and third-order geometrical optics results with the previously computed harmonic series for both magnitude and phase in the principal H plane. For this value of ka, the harmonic series has been accurately computed for a reference. It is evident from Fig. 3 that the third-order geometrical optics values are an improvement over the second-order values since they approximate the harmonic series over a larger azimuthal sector of space in both amplitude and phase. This improvement is due to the third-order terms which were taken into account in the evaluation of the integral in (5).

For example, both amplitudes are about 97 per cent of the harmonic series amplitude at $\phi = 50°$, but at $\phi = 80°$ the second-order approximation is 58 per cent while the third-order approximation is 83 per cent of the harmonic series. In the phase, the second-order approximation is 98 per cent of the harmonic series at $\phi = 50°$ and drops to 97 per cent at $\phi = 80°$ while the third-order approximation stays above 99 per cent of the harmonic series in this range. However, both of these approximations begin to deteriorate badly, especially in amplitude, as $\phi \to \pi/2$ from below. There are several possible reasons for this deterioration. In the third-order approximation, it is thought that the primary source of difficulty lies in the saddle point evaluation of the ν-plane integration in (5). Here the technique (details are given by Bailin and Spellmire[5]) required the splitting of $H_{1/3}^{(1)}(x)$ into an amplitude and phase function. For large x, this division was accomplished with the aid of the asymptotic behavior of the Hankel function. However, it can be shown that x is large if either ka is large or ϕ is small. In the region where $\phi \to \pi/2$, x is small regardless of the value of ka. Consequently, a different method must be used in the splitting of $H_{1/3}^{(1)}(x)$ in this azimuthal sector, generally referred to as the transition region.

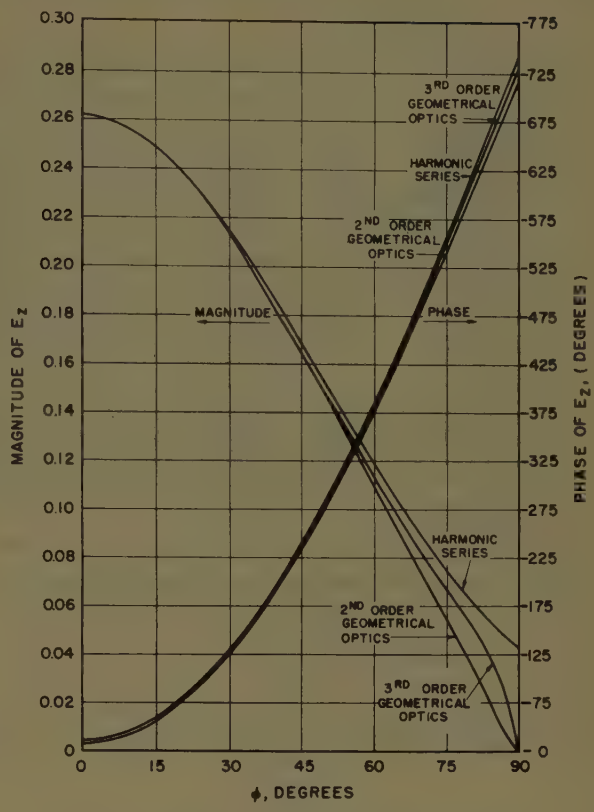

Fig. 3—E_z for circumferential slot $ka = 12$.

B. Residue Series Representation ($\pi \geq |\phi| > \pi/2$)

As stated in Section I, an evaluation of (2) at the poles, determined from $H_{\nu_m}^{(2)}(ka) = 0$, gives the residue series representation. When a Watson transformation is used on (2) in which the contour C_1 in Fig. 2 is distorted to the contour C_2 to enclose the complex poles ν_m, the following is obtained:

$$\Pi_z = -j2\pi K \sum_{m=1}^{\infty} \frac{H_{\nu_m}^{(2)}(kr)}{\exp[j\nu_m\pi/2]} \frac{\cos\nu_m(\pi-\phi)}{M_{|\nu_m|}} S(\nu_m, \phi_0) \quad (14)$$

where

$$M_{|\nu_m|} = \frac{j\sin\nu_m\pi}{\exp[j\nu_m\pi/2]}\left[\frac{\partial H_\nu^{(2)}(ka)}{\partial\nu}\right]_{\nu=\nu_m}.$$

For the far field (large r), if the asymptotic approximation

$$\frac{H_{\nu_m}^{(2)}(kr)}{\exp[j\nu_m\pi/2]} \sim \left(\frac{2}{\pi kr}\right)^{1/2} \exp[-j(kr - \pi/4)]$$

and the source function[6] for the half-wavelength delta slot are used, E_z is obtained from (14) as

$$E_z \sim -j\left(\frac{2}{\pi}\right)^{1/2}\left(\frac{1}{kr}\right)^{1/2} \exp[-j(kr - \pi/4)] \cdot \sum_{m=1}^{\infty} \frac{\cos\left(\frac{\nu_m\pi}{2ka}\right)}{\left[1 - \left(\frac{\nu_m}{ka}\right)^2\right]} \frac{\cos[\nu_m(\pi - \phi)]}{M_{|\nu_m|}}. \quad (15)$$

TABLE I

COEFFICIENTS FOR THE COMPUTATION OF v_m

m	A_{1m}	A_{2m}	A_{3m}	A_{4m}	A_{5m}	A_{6m}	B_{1m}	B_{2m}	B_{3m}	B_{4m}
1	0.9278790	0.0573973	0.0182598	0.0029389	0.0012396	0.0012127	1.6071338	0.0994151	0.0050902	0.0021471
2	1.6223057	0.1754581	0.0975930	0.0274627	0.0202530	0.0346404	2.8099161	0.3039027	0.0475667	0.0350793
3	2.1908369	0.3199841	0.2403540	0.0913382	0.0909658	0.2101110	3.7946412	0.5542293	0.1582025	0.1575575
4	2.6933084	0.4835936	0.4465596	0.2086204	0.2554220	0.7252791	4.6649475	0.8376095	0.3613413	0.4424042
5	3.1526334	0.6626059	0.7162120	0.3916574	0.5613002	1.8656465	5.4605218	1.1476682	0.6783707	0.9722010
6	3.5806434	0.8547331	1.0493115	0.6517136	1.0607993	4.0045622	6.2018571	1.4804426	1.1288013	1.8373595
7	3.9844482	1.0583875	1.4458583	0.9992755	1.8099590	7.6032218	6.9012675	1.8331829	1.7307961	3.1349431
8	4.3687383	1.2723905	1.9058524	1.4442309	2.8681905	13.2106676	7.5668775	2.2038472	2.5014816	4.9678550
9	4.7368138	1.4958256	2.4292941	1.9959871	4.2979301	21.4637892	8.2044031	2.5908486	3.4571516	7.4442385
10	5.0911066	1.7279561	3.0161831	2.6635522	6.1643701	33.0873220	8.8180562	2.9929108	4.6134084	10.6770096
11	5.4334743	1.9681744	3.6665195	3.4555958	8.5352427	48.8938486	9.4110546	3.4089815	5.9852685	14.7834842
12	5.7653767	2.2159692	4.3803035	4.3804952	11.4806429	69.7838007	9.9859265	3.8381751	7.5872415	19.8850705
13	6.0879863	2.4709030	5.1575349	5.4463702	15.0728680	96.7454525	10.5447027	4.2797338	9.4333913	26.1070066
14	6.4022640	2.7325966	5.9982137	6.6611135	19.3863367	130.8549281	11.0890478	4.7330009	11.5373888	33.5781433
15	6.7090091	3.0007177	6.9023400	8.0324133	24.4973875	173.2761977	11.6203459	5.1974007	13.9125502	42.4307491

Eq. (15) is now compared with the harmonic series of (13) by canceling the common factors and renormalizing to give

$$E_z \sim -j\frac{2\pi}{(ka)^2}\sum_{m=1}^{\infty}\frac{\cos\dfrac{\nu_m\pi}{2ka}}{\left[1-\left(\dfrac{m}{ka}\right)^2\right]}\cdot\frac{\cos\nu_m(\pi-\phi)}{M_{|\nu_m|}}. \quad (16)$$

To evaluate the residue series of (16), numerical values of the complex roots, ν_m and the associated function

$$\left.\frac{\partial H_\nu^{(2)}(ka)}{\partial\nu}\right]_{\nu=\nu_m}$$

must be obtained. The complex roots of $H_{\nu_m}^{(2)}(z)=0$, where $z=ka$ is large, can be obtained in several ways.[1] The Sommerfield integral representation for the Hankel function leads to a second-order approximation for ν_m, and the Langer[8] representation for the Hankel function of large argument leads to a third-order approximation. To facilitate computation for different values of ka, both the second- and third-order approximations for ν_m were put into the following form:

$$\nu_m = z + A_{1m}z^{1/3} - A_{2m}z^{-1/3} + A_{3m}z^{-3/3} - A_{4m}z^{-5/3} - A_{5m}z^{-7/3} + A_{6m}z^{-9/3} + \cdots - j\{B_{1m}z^{1/3} + B_{2m}z^{-1/3} - B_{3m}z^{-5/3} + B_{4m}z^{-7/3} + \cdots\} \quad (17)$$

where $z=ka$.

The third-order approximations were used in preference to the second order, because better results were obtained with the same amount of effort once the coefficients A_{nm} and B_{nm} were known. The coefficients for the third-order approximations are as accessible as those for the second order, since they depend upon the roots of the transcendental equation $J_{1/3}(x)+J_{-1/3}(x)=0$, which are tabulated.[5]

Similarly, the associated function

$$\left.\frac{\partial H_\nu^{(2)}(ka)}{\partial\nu}\right]_{\nu=\nu_m}$$

was cast into the form:

$$\left.\frac{\partial H_\nu^{(2)}(ka)}{\partial\nu}\right]_{\nu=\nu_m} = C_m z^{-2/3}\{1 + D_{1m}z^{-2/3} - D_{2m}z^{-4/3} + D_{3m}z^{-6/3} + \cdots\} - jE_m z^{-2/3}\{1 - D_{1m}z^{-2/3} + D_{3m}z^{-6/3} + \cdots\}. \quad (18)$$

Detailed methods for the numerical evaluation of the constants A_{nm}, B_{nm}, C_m, D_{nm}, and E_m which are shown in Table I and Table II are given in a previous report.[5]

To check the validity of the equations, sample computations were made using $ka=12$ and the third-order approximation for ν_m and

$$\left.\frac{\partial H_\nu^{(2)}(ka)}{\partial_\nu}\right]_{\nu=\nu_m}$$

in (16). Four terms in the residue series were found to be sufficient to approximate accurately the fields in both magnitude and phase for about 70° on either side of $\phi=180°$, compared with 25 terms in the harmonic series. The results of (16) for $1\leq m\leq 4$ and $\phi=180°(10°)90°$, expressed as a magnitude and phase, are shown in Fig. 4 and are compared with the harmonic series results of (13). The residue series curves have no noticeable deviation from the harmonic series curves for both amplitude and phase in the range $180°\geq\phi>100°$. Since the residue series begins to deteriorate as $\phi\rightarrow 90°$, check computations for $\phi=90°$ and $\phi=95°$ were made to indicate the sum of the residue series after each of fifteen terms was considered. The result is poor but recognizable for $\phi=95°$ after fifteen terms; however, for $\phi=90°$ the series did not converge sufficiently to indicate even remotely the result obtained from the harmonic series. If the sum of the series is computed using the Euler[9] transforma-

[8] R. E. Langer, "On the asymptotic solutions of differential equations with application to the Bessel functions of large complex order," *Trans. Amer. Math. Soc.*, vol. 34, pp. 447–480; 1932.

[9] K. Knapp, "Theory and Application of Infinite Series," Hofner Publishing Co., New York, N. Y., 2nd Eng. ed., pp. 244–246.

TABLE II

COEFFICIENTS FOR THE COMPUTATION OF $\left.\dfrac{\partial H_\nu^{(2)}(z)}{\partial \nu}\right]_{\nu=\nu m}$

m	C_m	D_{1m}	D_{2m}	D_{3m}	E_m
1	1.1131027	0.3711514	0.4045138	0.1269169	1.9279502
2	−1.2748603	0.6489219	1.2365613	0.6783325	−2.2081226
3	1.3734258	0.8763343	2.2551253	1.6706108	2.3788431
4	−1.4458853	1.0773228	3.4081819	3.1038693	−2.5043466
5	1.5038019	1.2610527	4.6697918	4.9781220	2.6046611
6	−1.5523556	1.4322566	6.0238305	7.2933722	−2.6887585
7	1.5943383	1.5937785	7.4591089	10.0496210	2.7614748
8	−1.6314333	1.7474944	8.9673195	13.2468689	−2.8257252
9	1.6647605	1.8947246	10.5420045	16.8851162	2.8834495
10	−1.6950300	2.0364416	12.1779711	20.9643627	−2.9358779
11	1.7228219	2.1733886	13.8709372	25.4846086	2.9840148
12	−1.7485417	2.3061495	15.6172996	30.4458543	−3.0285628
13	1.7724935	2.4351933	17.4139749	35.8480994	3.0700485
14	−1.7949326	2.5609043	19.2582913	41.6913441	−3.1089142
15	1.8160517	2.6836023	21.1479054	47.9755884	3.1454936

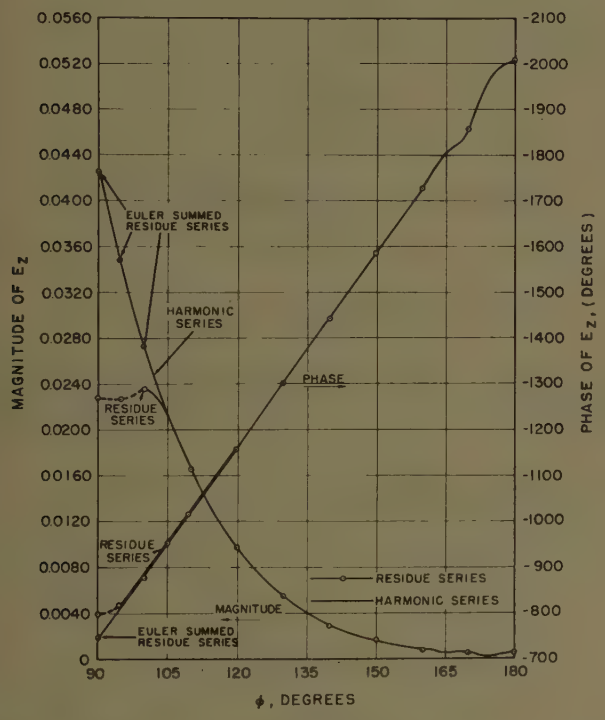

Fig. 4—E_z for circumferential slot $ka=12$.

tion, excellent results are obtained in the range $105° > \phi \geq 90°$ using four terms.

III. Axial Slot

For the radiation characteristics of an axial slot, it is also possible to start with the equation[1] for the magnetic Hertz vector

$$\Pi_z^* = \frac{'K}{2j}\int_{C'} \frac{H_\nu^{(2)}(kr)}{H_\nu^{(2)\prime}(ka)} \frac{\exp[j\nu(\pi-\phi)]}{\sin \nu\pi}\, d\nu \qquad (19)$$

where C_1 is again the contour of Fig. 2. For an infinite axial slot or the principal H-plane fields of a half-wavelength slot,

$$'K = \frac{V_0}{j2\pi\omega\mu ka}$$

where V_0 = voltage across the gap for a delta source. As in the case of the circumferential slot, this integral may be evaluated in three different ways. If the residue theorem is used at the poles $\nu = n$, then (19) becomes the harmonic representation,

$$\Pi_z^* = {'K}\sum_n \frac{H_n^{(2)}(kr)}{H_n^{(2)\prime}(ka)} \exp[-jn\phi].$$

If the integral is evaluated at the poles given by $H_{\nu_m}^{(2)\prime}(ka)=0$, then the residue series representation (which will be discussed in Part B) is obtained. Of course, the third possibility is to evaluate the integral along the path C_1, without using the residue theorem. This method, again, will lead to the geometrical optics results.

A. Third Order Geometrical Optics Representation ($|\phi| < \pi/2$)

To obtain the geometrical optics results, the contour C_1 is considered, and the integral is modified as before so that (19) can be given as

$$\Pi_z^* = {'K}\sum_{m=0}\left[\int_{-\infty+je}^{\infty+je} \frac{H_\nu^{(2)}(kr)H_\nu^{(1)\prime}(kr)}{H_\nu^{(2)\prime}(ka)H_\nu^{(1)\prime}(ka)} \exp[j\nu(2m+1)\pi-\phi]d\nu + \int_{-\infty-je}^{\infty-je} \frac{H_\nu^{(2)}(kr)H_\nu^{(1)\prime}(ka)}{H_\nu^{(2)\prime}(ka)H_\nu^{(1)\prime}(ka)} \exp[-j\nu(2m\pi+\phi)]d\nu\right] \qquad (20)$$

From a consideration of the saddle points of the integrals in (20), it can be shown[1] that the first integral gives the fields in the region of space where $2\pi \geq \phi > 3\pi/2$ and that the second integral describes the fields in the region of space where $\pi/2 > \phi \geq 0$. Thus, if again only the $m=0$ term for $\pi/2 > \phi \geq 0$ is considered, then

$$\Pi_z^* = {}'K \int_{-\infty - j\phi}^{\infty - j\phi} \frac{H_\nu^{(2)}(kr) H_\nu^{(1)\prime}(ka)}{H_\nu^{(2)\prime}(ka) H_\nu^{(1)\prime}(ka)} \exp\left[-j\nu\phi\right] d\nu. \quad (21)$$

This integral may be evaluated to third order by the techniques described by Bailin and Spellmire[10] and yields a far-field result which is valid for large ka or small ϕ. Thus (21) becomes

$$\Pi_z^* = \frac{j2'K}{\pi} \frac{\exp\left[-j(kr - \pi/4)\right]}{(kr)^{1/2}} A(\nu_s) \cdot \exp\left[jf(\nu_s) - j\left(\frac{2\beta^3}{27\alpha^2} - \frac{5\pi}{12}\right)\right] \frac{\pi}{3\sqrt{3}} \frac{\beta}{\alpha} H_{1/3}^{(1)}\left(\frac{2\beta^3}{27\alpha^2}\right) \quad (22)$$

where

$$\cos \gamma_s = \frac{\nu_s}{ka}$$

$$A(\nu_s) = \left(\frac{\sin \gamma_s}{ka}\right)^{1/2} \frac{\left[1 + (1/2ka)^2\right]^{1/2}}{H_{\nu_s}^{(1)\prime}(ka) H_{\nu_s}^{(2)\prime}(ka)}$$

and

$$f(\nu_s) = \left[(ka)^2 - (\nu_s)^2\right]^{1/2} + \nu_s \sin^{-1}\left(\frac{\nu_s}{ka}\right) - \nu_s\phi + \left[\frac{1}{2ka} + \frac{13\nu_s^2}{12(ka)^3}\right].$$

The value of ν_s is determined from

$$f'(\nu_s) = \sin^{-1}\left(\frac{\nu_s}{ka}\right) + \frac{13\nu_s}{6(ka)^3} - \phi = 0$$

and

$$\alpha = \tfrac{1}{6} f'''(\nu_s) \qquad \beta = \tfrac{1}{2} f''(\nu_s).$$

It can be shown[4] that to third order

$$H_{\nu_s}^{(1)\prime}(ka) H_{\nu_s}^{(2)\prime}(ka) = \frac{\sin \gamma_s}{ka} (A^2 + B^2)$$

where

$$A = \frac{X^{1/2}}{\cos^2 \gamma_s}\left[J_{-2/3}(X) - \frac{2}{\sqrt{3}} \sin^2 \gamma_s J_{1/3}(X) + \frac{\sin^2 \gamma_s}{\sqrt{3}} J_{1/3}(X)\right]$$

$$B = \frac{X^{1/2}}{\cos^2 \gamma_s}\left[\frac{1}{\sqrt{3}} J_{-2/3}(X) - \sin^2 \gamma_s J_{1/3}(X) + \frac{2}{\sqrt{3}} J_{2/3}(X)\right] \quad (23)$$

with

$$X = \frac{ka}{3} \frac{\sin^3 \gamma}{\cos^2 \gamma}.$$

Since the far-field components are obtained from the Hertz vector

$$E_\phi = j\omega\mu \frac{\partial \Pi_z^*}{\partial r}$$
$$H_z = k^2 \Pi_z^*, \quad (24)$$

then to third order as $r \to \infty$

$$E_\phi = \left(\frac{V}{2\pi a}\right)\left(\frac{2}{\pi}\right)^{1/2}\left(\frac{2}{\pi kr}\right)^{1/2} \exp\left[-j(kr - \pi/4)\right] A(\nu_s) \cdot \exp\left[jf(\nu_s) - j\left(\frac{2\beta^3}{27\alpha^2} - \frac{5\pi}{12}\right)\right] \times \frac{\pi}{3\sqrt{3}} \frac{\beta}{\alpha} H_{1/3}^{(1)}\left(\frac{2}{27} \frac{\beta^3}{\alpha^2}\right). \quad (25)$$

Now as $\phi \to 0$, $\nu_s \to 0$ and

$$\left(\frac{2\beta^3}{27\alpha^2}\right) \to \infty,$$

$$H_{1/3}^{(1)}(z) \to \sqrt{\frac{2}{\pi z}} \exp\left[j\left(z - \frac{5\pi}{12}\right)\right]$$

and

$$H_{\nu_s}^{(1)\prime}(ka) H_{\nu_s}^{(2)\prime}(ka) \to \frac{2}{ka\pi}.$$

When these asymptotic behaviors are used, (25) reduces to

$$E_\phi \sim \left(\frac{V}{2\pi a}\right)\left(\frac{2}{\pi kr}\right)^{1/2} \cdot \exp\left[-j(kr - \pi/4)\right] \pi ka \left[1 - \frac{13}{12(ka)^2}\right] \cdot \exp\left[j\left(ka \cos \phi + \frac{1}{2ka}\right)\right] \quad (26)$$

which is a better approximation in both amplitude and phase than the second-order result[1] given by

$$E_\phi \sim \left(\frac{V}{2\pi a}\right)\left(\frac{2}{\pi kr}\right)^{1/2} \exp\left[-j(kr - \pi/4)\right](\pi ka) \cdot \exp\left[j(ka \cos \phi)\right].$$

To make a numerical comparison of the results from these approximate equations and of the harmonic series for the far field which can be obtained from (20) as

$$E_\phi = \left(\frac{V}{2\pi a}\right)\left(\frac{2}{\pi kr}\right)^{1/2} \exp\left[-j(kr - \pi/4)\right] \cdot \exp\left[-j\pi/2\right] \sum_n \frac{\exp\left[jn\pi/2 - jn\phi\right]}{H_n^{(2)\prime}(ka)}, \quad (27)$$

the common factors are canceled out, and the harmonic series is renormalized to give

[10] *Op. cit.*, Appendix B.

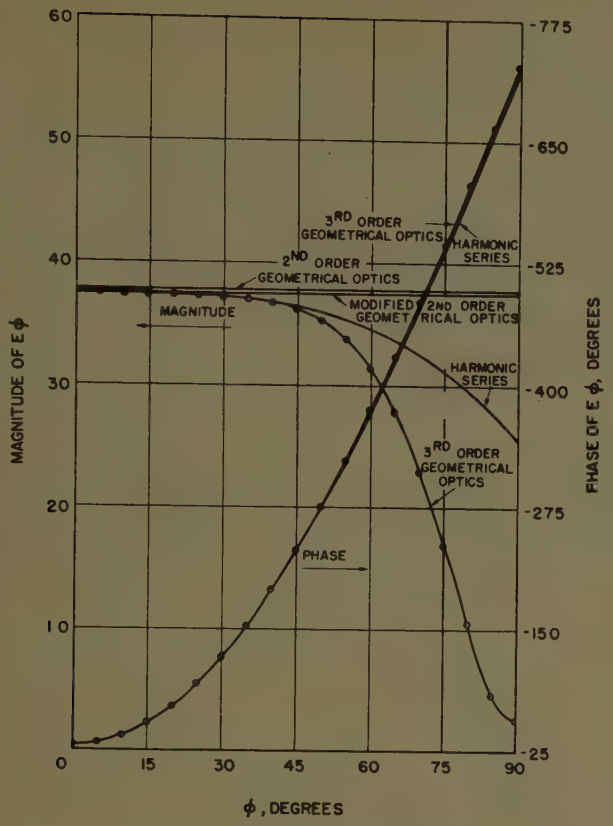

Fig. 5—E_ϕ for axial slot $ka=12$.

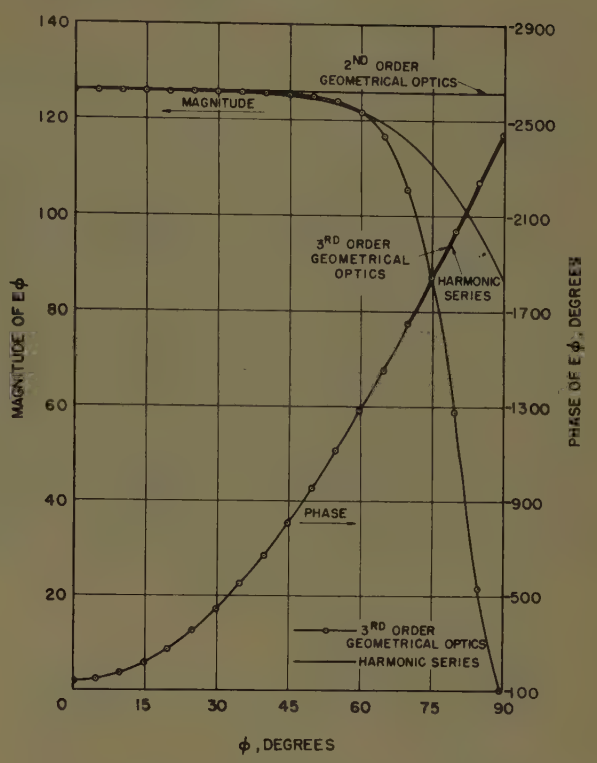

Fig. 6—E_ϕ for axial slot $ka=40$.

$$E_\phi = \exp\left[-j\pi/2\right] \sum_n \frac{\exp\left[in\pi/2 - jn\phi\right]}{H_n^{(2)\prime}(ka)}. \quad (28)$$

Then the modified second-order geometrical optics approximation becomes

$$E_\phi = \pi ka\left[1 - \frac{13}{12(ka)^2}\right]\exp\left[j(ka\cos\phi + 1/2ka)\right] \quad (29)$$

and the third-order geometrical optics approximation becomes

$$E_\phi = \left(\frac{2}{\pi}\right)^{1/2} A(\nu_s)\exp\left[jf(\nu_s) - j\left(\frac{2\beta^3}{27\alpha^2} - \frac{5\pi}{12}\right)\right]$$
$$\cdot\frac{\pi}{3\sqrt{3}}\,\frac{\beta}{\alpha}\,H_{1/3}^{(1)}\left(\frac{2}{27}\,\frac{\beta^3}{\alpha^2}\right). \quad (30)$$

Numerical results of (28) (harmonic series)[11], (29) (modified second-order geometrical optics approximation), (30) (third-order geometrical optics approximation), and Sensiper's second-order approximation are shown in Fig. 5 for $ka=12$ and in Fig. 6 for $ka=40$. The gain of accuracy of the third-order geometrical optics approximations over the second-order geometrical optics approximations is negligible for the phase; however, the third-order approximations give better values for $\phi>0°$, since the amplitude curves for the second-order approximations are constant (that is, independent of ϕ) while the amplitude curves for the third-order approximation tend to follow the harmonic series curves.

[11] The numerical results for the harmonic series for $ka=12$ were taken from Bailin, *op. cit.*, and those for $ka=40$ from computations by the NBS Computation Lab. presented to us in a private communication from Dr. W. Saunders of the Diamond Ordinance Fuze Laboratory.

B. Residue Series Representation

When the method of the circumferential slot is followed (19) becomes

$$\Pi_z^* = -j2\pi' K \sum_{m=1}^{\infty} \frac{H_{'\nu_m}^{(2)}(kr)}{\exp\left[j'\nu_m\pi/2\right]}\,\frac{\cos{}'\nu_m(\pi-\phi)}{M_{|'\nu_m|}} \quad (31)$$

where

$$M_{|'\nu_m|} = \frac{j\sin{}'\nu_m\pi}{\exp\left[j'\nu_m\pi/2\right]}\,\frac{\partial H_\nu^{(2)\prime}(ka)}{\partial\nu}\Bigg]_{\nu='\nu_m}.$$

Since

$$E_\phi = j\omega\mu\,\frac{\partial\Pi_z^*}{\partial r},$$

then in the far field ($r\to\infty$), E_ϕ becomes

$$E_\phi = -\frac{V}{2\pi a}\left(\frac{2}{\pi kr}\right)^{1/2}\exp\left[-j(kr-\pi/4)\right]$$
$$\cdot 2\pi\sum_{m=1}^{\infty}\frac{\cos{}'\nu_m(\pi-\phi)}{M\,|\,'\nu_m\,|}. \quad (32)$$

For comparison purposes, the common factors of (27) and (32) were canceled, and (32) now becomes

$$E_\phi \sim 2\pi\exp\left[j\pi\right]\sum_{m=1}^{\infty}\frac{\cos{}'\nu_m(\pi-\phi)}{M\,|\,'\nu_m\,|}. \quad (33)$$

TABLE III

COEFFICIENTS FOR COMPUTATION OF $\frac{'\nu_m}{ka}$

M	K_{0m}	K_{1m}	K_{2m}	K_{3m}	K_{4m}	K_{5m}
1	1	0.40430823 $(1-j\sqrt{3})$	0.07273174 $(-1-j\sqrt{3})$	0.06525312	0.01188593 $(-1+j\sqrt{3})$	0.00105769 $(-1-j\sqrt{3})$
2	1	1.28904796 $(1-j\sqrt{3})$	0.13017057 $(-1-j\sqrt{3})$	0.10353615	0.04777835 $(-1+j\sqrt{3})$	0.05356433 $(-1-j\sqrt{3})$
3	1	1.91285748 $(1-j\sqrt{3})$	0.25700457 $(-1-j\sqrt{3})$	0.21435659	0.10779227 $(-1+j\sqrt{3})$	0.15174500 $(-1-j\sqrt{3})$
4	1	2.44590997 $(1-j\sqrt{3})$	0.40905317 $(-1-j\sqrt{3})$	0.38878826	0.21188267 $(-1+j\sqrt{3})$	0.34684651 $(-1-j\sqrt{3})$
5	1	2.92565024 $(1-j\sqrt{3})$	0.57917419 $(-1-j\sqrt{3})$	0.62669711	0.37421154 $(-1+j\sqrt{3})$	0.63461976 $(-1-j\sqrt{3})$
6	1	3.36865792 $(1-j\sqrt{3})$	0.76394571 $(-1-j\sqrt{3})$	0.92806346	0.60700924 $(-1+j\sqrt{3})$	1.11126040 $(-1-j\sqrt{3})$
7	1	3.78414515 $(1-j\sqrt{3})$	0.96125758 $(-1-j\sqrt{3})$	1.29288129	0.92138696 $(-1+j\sqrt{3})$	1.81438363 $(-1-j\sqrt{3})$
8	1	4.17790446 $(1-j\sqrt{3})$	1.16964384 $(-1-j\sqrt{3})$	1.72114855	1.32768068 $(-1+j\sqrt{3})$	2.80118528 $(-1-j\sqrt{3})$
9	1	4.55387890 $(1-j\sqrt{3})$	1.38801180 $(-1-j\sqrt{3})$	2.21286439	1.83563957 $(-1+j\sqrt{3})$	4.13218591 $(-1-j\sqrt{3})$
10	1	4.91490612 $(1-j\sqrt{3})$	1.61550800 $(-1-j\sqrt{3})$	2.76802826	2.45454479 $(-1+j\sqrt{3})$	5.87087372 $(-1-j\sqrt{3})$
11	1	5.26311466 $(1-j\sqrt{3})$	1.85144325 $(-1-j\sqrt{3})$	3.38664078	3.19329156 $(-1+j\sqrt{3})$	8.08345789 $(-1-j\sqrt{3})$
12	1	5.60015281 $(1-j\sqrt{3})$	2.09524661 $(-1-j\sqrt{3})$	4.06869950	4.06044434 $(-1+j\sqrt{3})$	10.83502643 $(-1-j\sqrt{3})$
13	1	5.92733011 $(1-j\sqrt{3})$	2.34643577 $(-1-j\sqrt{3})$	4.81420662	5.06428846 $(-1+j\sqrt{3})$	14.20739296 $(-1-j\sqrt{3})$
14	1	6.24570886 $(1-j\sqrt{3})$	2.60459678 $(-1-j\sqrt{3})$	5.62316141	6.21285803 $(-1+j\sqrt{3})$	18.26292494 $(-1-j\sqrt{3})$
15	1	6.55616578 $(1-j\sqrt{3})$	2.86939695 $(-1-j\sqrt{3})$	6.49556373	7.51396679 $(-1+j\sqrt{3})$	23.08049493 $(-1-j\sqrt{3})$

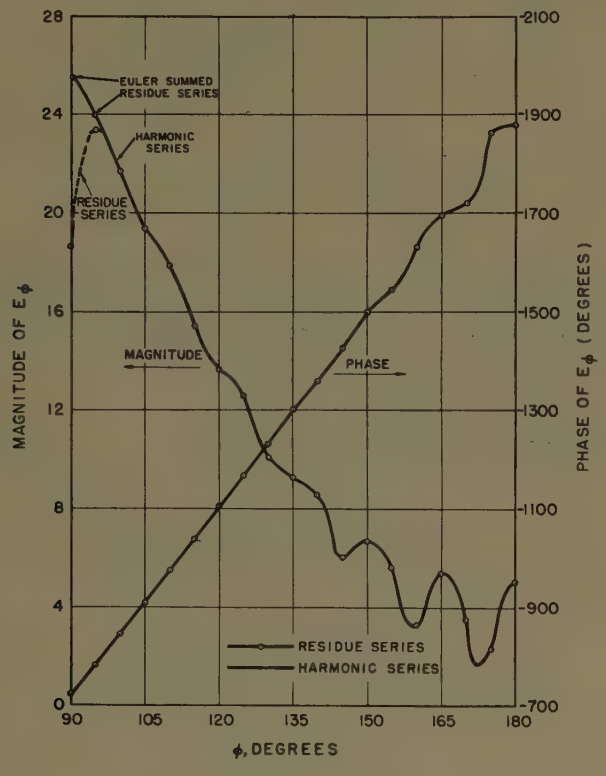

Fig. 7—E_ϕ for axial slot $ka=12$.

Again the Langer representation of the Hankel function was used to determine a third-order approximation for for $'\nu_m$.[12] As before, $'\nu_m$ was cast in the form

$$\frac{'\nu_m}{ka} = \sum_{p=0}^{\infty} K_{pm}(1/ka)^{2p/3} \tag{34}$$

where the coefficients K_{pm} are given in Table III. The associated function

$$\frac{\partial H_\nu^{(2)\prime}(z)}{\partial \nu}\Bigg]_{\nu='\nu_m}$$

[12] Details of the numerical techniques involved are shown by Bailin and Spellmire, *op. cit.*

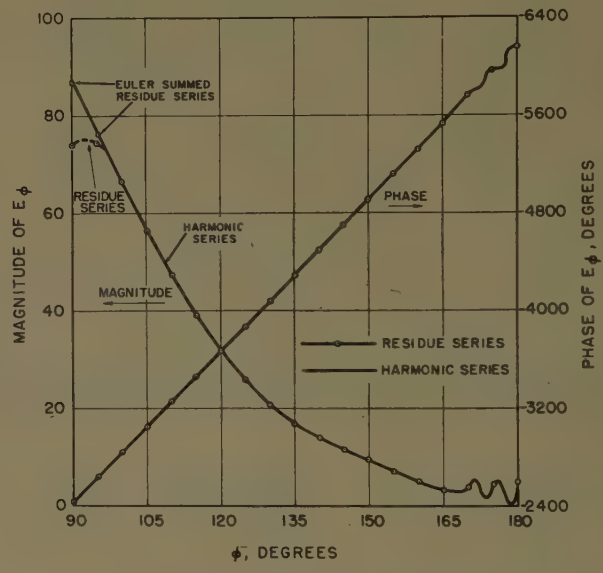

Fig. 8—E_ϕ for axial slot $ka=40$.

can be found from the functional equation

$$\frac{\partial H_\nu^{(2)\prime}(z)}{\partial \nu}\Bigg]_{\nu='\nu_m} = \frac{[1-('\nu_m/z)^2]H_{'\nu_m}^{(2)}(z)}{d'\nu_m/dz} \tag{35}$$

where $d'\nu_m/dz$ is found from (34) to be

$$\frac{d'\nu_m}{dz} = \sum_{p=0}^{\infty}(1-2p/3)K_{pm}(1/ka)^{2p/3} \tag{36}$$

and $H_{'\nu_m}^{(2)}(z)$ is obtained from the Langer representation

$$H_{'\nu_m}^{(2)}(z) = \left(\frac{\tan{}'\alpha_m - {}'\alpha_m}{\tan{}'\alpha_m}\right)^{1/2} \cdot \exp[-j\pi/6]H_{1/3}^{(2)}['\nu_m(\tan{}'\alpha_m - {}'\alpha_m)] \tag{37}$$

where $'\nu_m = z\cos{}'\alpha_m$.

Results of (33) and (28)[11] are shown in Fig. 7 for $ka=12$ and in Fig. 8 for $ka=40$. For $ka=12$ up to fifteen terms ($m=15$) were used, but for $ka=40$ the use of only

four terms was considered adequate. The residue series curves have no noticeable deviation from the harmonic series curves in both amplitude and phase in the range $180° > \phi > 100°$. In the range $100° > \phi > 90°$ the residue series curves for amplitude deviate quite noticeably from the harmonic series curves, while the residue series curves for phase are well within graphical accuracy. If, however, the Euler summation technique is used on the residue series in the region around $\phi = 90°$, good results are obtained. It is worth noting that the residue series can be summed, in the Euler sense, in the geometric optics region $90° \geq \phi \geq 80°$ using eight terms.

IV. Conclusion

The approximation formulas described present a tractable, and in some cases simple, representation for the radiation fields from slots on cylinders. The accuracy of the various approximations discussed varies with the type of slot and with the region of space which is of interest. In the geometrical optics region, for the circumferential slot, the third-order values are an improvement over the second-order values, since they approximate better the true field over a larger azimuthal sector of space in both amplitude and phase. For the axial slot, the third-order approximation is the lowest order that can be used to obtain the magnitude, unless one is willing to accept a constant (that is, independent of ϕ).

In the shadow region, where the residue series is applicable for both the circumferential and axial slots, it is easier to compute from the third-order approximation formulas than from the second-order formulas if the tables in this paper are used. Unfortunately, no computations using second-order approximation formulas were made to test the gain in accuracy.

In general, the third-order approximations are adequate to approximate the fields except in the transition region (that is, the region around 90°). In this region, the approximations involved in the geometrical optics formulas are no longer valid, and the residue series requires too many terms to be practical when ordinary summation is used. However, the Euler transformation gives good results with the residue series even into the geometric optics region around $\phi = 90°$. Further study is being given to extending the range of the residue series by using a generalized Euler transformation.[13]

V. Acknowledgment

The authors wish to thank Dr. S. Sensiper for his many helpful suggestions during the course of this work and Miss Carol Hasson for her aid in computing the numerical results. We also wish to extend our thanks to N. A. Logan for suggesting the use of the Euler transformation at the point $\phi = 90°$.

[13] G. H. Hardy, "Divergent Series," Oxford University Press, New York, N. Y.; 1949.

Some Observations on Scattering by Turbulent Inhomogeneities*

MARTIN BALSER†

Summary—**Several topics in the theory of radio wave scattering by dielectric inhomogeneities due to turbulence are discussed. A corrected derivation of the scattering formula is presented (which does not change the result), using the proper dyadic Green's function and examining the terms in the wave equation caused by the nonvanishing divergence of the scattered field. The statistics (distribution and correlation functions) of the received signal are considered. In particular, the significance of the space correlation function in testing some theoretical results is questioned. It is suggested that the frequency dependence of the time correlation function may give more information about the nature of the turbulence.**

Introduction

THE process of scattering radio waves by dielectric inhomogeneities has been of interest for some time in connection with the anomalous long-distance propagation of vhf and uhf (and higher frequency) waves. Despite this, a number of points about the electromagnetic theory involved seem to have never been adequately considered. It is the purpose of this paper to examine critically some of the assumptions and steps in the development of the formalism of scattered fields, as well as to discuss some inferences pertaining to these formulas that may be made from elementary observations on the nature of turbulence.

* Manuscript received by the PGAP, July 25, 1956; revised manuscript received, January 29, 1957. The research in this document was supported jointly by the Army, Navy, and Air Force under contract with the Massachusetts Institute of Technology.

† Lincoln Lab., Mass. Inst. Tech., Cambridge, Mass.

Derivation of the Scattered Field

The Quasistatic Approximation

The wave equation for the electric field, $E(r)$, is easily derived from the pair of Maxwell's equations connecting the electric and magnetic fields, and may be written

$$\nabla \times \nabla \times E + \mu_0 \frac{\partial^2}{\partial t^2} (\epsilon E) = -\mu_0 \frac{\partial J}{\partial t} \cdot \qquad (1)$$

It is already assumed that the magnetic susceptibility has its free-space value, μ_0, everywhere in the region to which (1) applies.

The basic assumption we shall make (in various forms) several times in the derivation is what we may call the quasistatic approximation; that is, since one variation takes place very slowly compared with another, we regard the problem as though the first variation did not exist and simply add its effect to the solution of the "static" problem. The justification for such an approximation must, of course, be drawn from observations (whether theoretical or experimental) of the physical situation.

In this case, the approximation is actually applied twice. Firstly, since the highest frequency with significant power in the spectrum of $\epsilon(t)$ is very small compared with ω, the radio frequency, we approximate

$$\frac{\partial^2}{\partial t^2}(\epsilon E) \approx \epsilon \frac{\partial^2 E}{\partial t^2}. \tag{2a}$$

Further, we assume that there are no impressed currents in the region, so

$$\frac{\partial J}{\partial t} \sim \sigma \frac{\partial E}{\partial t}. \tag{2b}$$

The "static" (or monochromatic) problem may now be solved by replacing $\partial/\partial t$ by $-i\omega$ (this convention will be used throughout), so that (1) may now be written

$$\nabla \times \nabla \times E - \omega^2 \mu_0 \epsilon E = 0 \tag{3}$$

where by ϵ we now mean the effective (generally complex) dielectric constant $\epsilon + i\sigma/\omega$.

There is abundant theoretical and experimental evidence that dielectric configurations in the atmosphere do not change in the order of microseconds or less, so this first assumption is easily accepted. At this point, however, a second assumption is made. We are ordinarily interested in the statistical properties of the scattered field, and hence in the statistics of the turbulent field which causes it. These properties are studied by taking time averages, such as the average power, distribution of signal level, and correlation functions. The assumption made is that the statistics themselves are not changing while the measurement is being made, or in other words, that the process is what we might call "locally stationary." Thus we may solve the statistical problem as though the process were truly stationary, then account for the slowly changing statistics afterward. As an example, we note that the received signal level is expected to vary (cf. our first assumption) according (as will be shown) to a Rayleigh distribution about a fixed mean determined by $\langle \Delta\epsilon^2 \rangle$. $\langle \Delta\epsilon^2 \rangle$ must, however, remain constant during the measurement or the observed distribution will be changed. It is, in fact, observed that for periods of the order of a minute the distribution of signal level is Rayleigh, but over many minutes it is not.[1,2] Thus we may expect that our assumption of "local stationarity" may apply as long as the time required for our statistical analysis is not more than a minute or two. (In cases of doubt, more involved statistical tests may have to be applied to determine, for instance, the confidence we may place in the hypothesis that the mean of the process has not changed during our measurement.)

Discussion of the Wave Equation

Letting $k_0^2 = \omega^2 \mu_0 \epsilon_0$ and $\epsilon(r) = \epsilon_0 + \Delta\epsilon(r)$, we can rewrite (3) as

$$-\nabla \times \nabla \times E + k_0^2 E = -k_0^2 \frac{\Delta\epsilon}{\epsilon_0} E. \tag{4}$$

When we expand the left side of (4), we get a term $\nabla(\nabla \cdot E)$ which, we must note, does not vanish for the very reason that we get scattering; *i.e.*, ϵ is not constant. Thus,

$$(\nabla^2 + k_0^2)E = -k_0^2 \frac{\Delta\epsilon}{\epsilon_0} E - \nabla\left(\frac{1}{\epsilon} \nabla\epsilon \cdot E\right). \tag{5}$$

The last term in (5) has been considered in a recent paper[3] and neglected on the grounds that $|\nabla\epsilon| \sim \Delta\epsilon/L_0$, where L_0 is the "scale length" of the turbulence; whereas the term with which it is compared is $k_0 \Delta\epsilon = 2\pi\Delta\epsilon/\lambda$. It is, however, not these gross characteristics of the turbulence which are relevant, but rather particular Fourier amplitudes [see, for instance, (17)]. These Fourier amplitudes, as we shall see, are of the same order of magnitude for the two terms, but for an entirely different reason the contribution of the additional term to the first-order scattered field is not small, but precisely zero.

We wish now to solve the vector (5) and at the same time to satisfy certain auxiliary conditions on E. To do this, it is not adequate to use a scalar Green's function. We require rather a dyadic Green's function; *i.e.*, a solution of

$$(\nabla_2 + k_0^2)\Gamma(r, r') = -\varepsilon\delta(r - r') \tag{6}$$

where ε is the unit dyadic, with the property that $\varepsilon \cdot A = A \cdot \varepsilon = A$ for an arbitrary vector, A. The standard solution to (6) is

$$\Gamma(r, r') = \left(\varepsilon - \frac{1}{k_0^2} \nabla\nabla'\right) \frac{e^{ik_0|r-r'|}}{4\pi|r - r'|} \tag{7}$$

[1] J. H. Chisholm, P. A. Portmann, J. T. deBettencourt, and J. F. Roche, "Investigations of angular scattering and multipath properties of tropospheric propagation of short radio waves beyond the horizon," PROC. IRE, vol. 43, pp. 1317–1335; October, 1955.

[2] R. A. Silverman and M. Balser, "Statistics of electromagnetic radiation scattered by a turbulent medium," *Phys. Rev.*, vol. 96, pp. 560–563; November 1, 1954.

[3] A. D. Wheelon, "Near-field corrections to line-of-sight propagation," PROC. IRE, vol. 43, pp. 1459–1466; October, 1955.

which automatically gives, at large distances from the sources, transverse outgoing spherical waves. The temptation is now simply to write the usual solution for the scattered field

$$E_{sc}(r) = E(r) - E_{inc}(r) = \int \Gamma(r, r') \cdot \left[k_0^2 \frac{\Delta\epsilon(r')}{\epsilon_0} E(r') + \nabla\left(\frac{1}{\epsilon} \nabla\epsilon(r') \cdot E(r')\right)\right] dr'$$

where the integral is taken over all space, but in effect only where $\Delta\epsilon \neq 0$. This solution clearly satisfies (5), but is not the solution we seek. The reason is that the solution for Γ, (7), has the additional property $\nabla \cdot \Gamma = 0$, which it imparts to the solution for E_{sc}. As we have seen, $\nabla \cdot E_{sc} \neq 0$. We may now either seek another Green's function which gives the proper divergence or, more simply, use the same Green's function to solve the wave equation for D, which is divergenceless. This latter equation can easily be seen to be

$$(\nabla^2 + k_0^2) D = -\epsilon \left[k_0^2 \frac{\Delta\epsilon}{\epsilon_0} E + \nabla\left(\frac{1}{\epsilon} \nabla\epsilon \cdot E\right) + 2\left(\nabla \frac{1}{\epsilon} \cdot \nabla\right) D + D\nabla^2 \frac{1}{\epsilon}\right] \equiv -F(r) \tag{8}$$

and the solution of (8) is

$$D_{sc}(r) = \int \Gamma(r, r') \cdot F(r') dr'. \tag{9}$$

Finally, in still another quasistatic approximation, we may separate $\Delta\epsilon$, hence $F(r)$, into the sum of two terms. The first describes the deviations of ϵ from ϵ_0 which are fairly constant in time, in effect the average over, say, many minutes or an hour. It thus includes the normal lapse rate of air density in the troposphere or electron density in the ionosphere, as well as meteorological effects such as persistent elevated layers and ducts. The second term, which is the one we consider, describes the short term fluctuations in ϵ, which we ascribe to turbulence. The solution of (9) is just the sum of the individual solutions. Since turbulence theories imply that the characteristics of the turbulent flow do not depend on the boundary conditions, we may conclude that these contributions will be incoherent.

The Far-Field and Single-Scattering Approximations

We may immediately simplify (9) by substituting the far-field approximation

$$\Gamma(r, r') \sim (\varepsilon - \hat{u}\hat{u}) \frac{e^{ik_0 R_1}}{4\pi R_1} \tag{10}$$

where $R_1 = |r - r'|$ and $\hat{u} = (r - r')/R_1$. ($\hat{u}$ is the unit vector from the source to the field point.) Eq. (10) neglects terms $0(\lambda/R)$ compared with the term retained. As already noted, the form of Γ insures that the far-field contribution from each scatterer is transverse. Thus (8) becomes

$$D_{sc}(r) \sim \int (\varepsilon - \hat{u}\hat{u}) \cdot F(r') \frac{e^{ik_0 R_1}}{4\pi R_1} dr'. \tag{11}$$

The principal difficulty in the mathematical analysis is the solution of this integral equation. Fortunately we do not have to solve (11) in full generality. Rather, we use the fact that $F(r) \alpha \Delta\epsilon(r) \ll \epsilon_0$ and assume that the scattered field may be adequately represented by

$$D_1(r) = \int \Gamma(r, r') \cdot F_0(r') dr' \tag{12}$$

where $F_0(r)$ is the function $F(r)$ in which we neglect terms $0(\Delta\epsilon^2)$. In particular, D and E are replaced by the incident fields. This is the single-scattering approximation. If desired, we may iterate the process to find the result of n scatterings,

$$D_n(r) = \int \Gamma(r, r') \cdot F_{n-1}(r') dr' \tag{13}$$

where F_{n-1} comprises terms $0(\Delta\epsilon^n)$ and is determined by the previous solutions.

It should be emphasized that the adequacy of the single-scattering approximation is an assumption and does not follow from the statement that $\Delta\epsilon \ll \epsilon_0$. For ionospheric scattering, it appears quite clearly justified since the inhomogeneities involved are fairly well restricted to the height of the common volume of the two antennas. Thus, radiation can arrive at the receiver only from this region. In the troposphere the case is not so clear-cut, but rough considerations support the adequacy of the approximation. A more detailed study of the relative importance of single and multiple scattering is being carried out.[4] We shall henceforth assume that (12) is an adequate approximation in the cases of interest.

Since the incident fields we shall be interested in are due to a transmitting antenna, $F_0(r)$ will be of the form

$$F_0(r) = f_0(r) \frac{e^{ik_0 R_0}}{R_0} \tag{14}$$

where R_0 is the distance of the scattering point from the antenna. The space dependence of the incident field, except for the (relatively) slow variations as the direction from the radiating antenna changes, is thus explicitly exhibited. It is to be understood that the operator ∇ in $f_0(r)$, when operating on the incident field, is to be replaced by ik_0, where k_0 is the propagation vector of magnitude k_0 and direction perpendicular to the wave front (here a sphere). Let us pick an arbi-

[4] H. Feshbach, private communication.

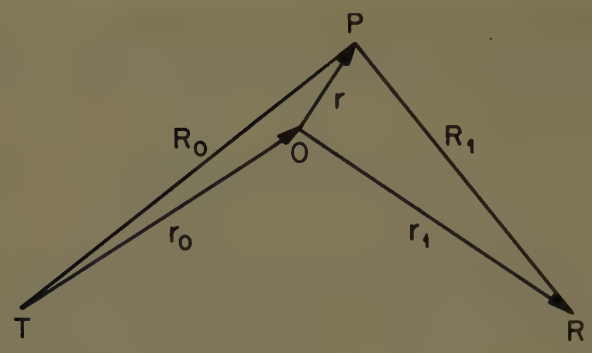

Fig. 1.

trary origin, 0, in the scattering region (see Fig. 1) and rewrite

$$k_0(R_0 + R_1) = k_0(r)\cdot r_0 + k_1(r)\cdot r_1 + K(r)\cdot r \quad (15)$$

where k_0 and k_1 are the propagation vectors from the transmitter, T, to the scattering point, P, and from P to the receiver, R. $K(r) = k_0(r) - k_1(r)$ and $|K(r)| = 2k_0 \sin\theta/2$, where θ is the scattering angle. Combining (15) with the far-field and single-scattering approximations, we find

$$D_1 = \int (\varepsilon - \hat{u}\hat{u})\cdot f_0(r') \frac{e^{i[k_0(r')\cdot r_0 + k_1(r')\cdot r_1]}}{4\pi R_0 R_1} e^{iK(r')\cdot r'} dr'. \quad (16)$$

For the case of a very limited scattering region, far removed from both transmitter and receiver, the propagation vectors can be considered constant over the region; *i.e.*, the rays are parallel. This is the plane wave, or Fraunhofer, limit. Eq. (16) then takes on the simple form

$$D_1 = \frac{e^{i(k_0\cdot r_0 + k_1\cdot r_1)}}{4\pi r_0 r_1} (\varepsilon - \hat{u}\hat{u})\cdot \int f_0(r') e^{iK\cdot r'} dr'. \quad (17)$$

It can now be shown (see Appendix) that the contributions to the first-order scattered field of all but the first term in $F(r)$ [see (8)] are strictly zero. Using this result, we may finally write

$$E_1 = \frac{e^{i(k_0\cdot r_0 + k_1\cdot r_1)}}{4\pi r_0 r_1} (\varepsilon - \hat{u}\hat{u})\cdot E_0 \frac{k_0^2}{\epsilon_0} \int \Delta\epsilon(r') e^{iK\cdot r'} dr' \quad (18)$$

where E_0 is defined by

$$E_{\text{inc}} = E_0 \frac{e^{ik_0 R_0}}{R_0}. \quad (19)$$

$(\varepsilon - \hat{u}\hat{u})\cdot E_0$ is, of course, that component of E_0 perpendicular to k_1. Eq. (18) is the familiar result that the scattered field is proportional to the component of the Fourier transform of $\Delta\epsilon$ corresponding to the wave number K. The polarization of the incident field is preserved (to first order) since the unpolarized term gives no contribution.

The approximation to Fraunhofer scattering is appliable as long as the length L of the wavefront over the scattering region (see Fig. 2) as seen by either the transmitter or receiver is plane, say to within a quarter

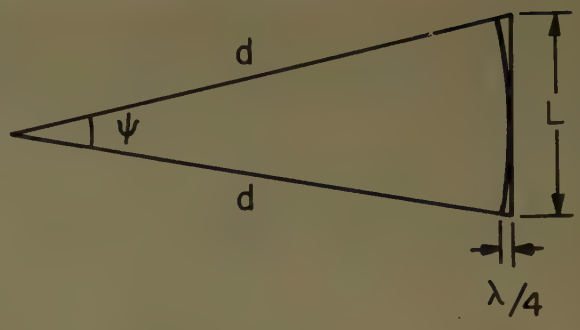

Fig. 2.

wavelength. This implies (since ψ is a small angle)

$$\frac{L^2}{2d\lambda} = \frac{\psi^2 d}{2\lambda} < 1. \quad (20)$$

For a reasonable ionospheric circuit, $\lambda = 6$ m and $d = 800$ km, and for a tropospheric circuit we may have $\lambda = 1$ m and $d = 150$ km. Both cases require $\psi \sim 0.25°$ or less. Present antenna patterns are not so narrow. Taking $\psi \sim \lambda/a$, where a is the relevant dimension of the antenna, (20) becomes

$$\frac{\lambda d}{2a^2} < 1. \quad (21)$$

Thus for the 150-km troposphere case with a 20-m dish, we would need $\lambda < 5$ mm to satisfy the Fraunhofer condition.

In general then, an accurate solution requires consideration of Fresnel scattering, characterized by nonplane wavefronts or, in another way, by differing angles of arrival. Let us suppose that the transmitting antenna causing the incident field radiates P_T watts with a vector voltage gain function $g_T(r)$, which has the magnitude of the voltage gain and the direction of the electric vector in the far field. $g_T(r)$ is actually a function of two angular variables only and is taken to be normalized; *i.e.*,

$$\frac{1}{4\pi}\int_0^{\pi}\int_0^{2\pi} |g_T(\theta, \phi)|^2 \sin\theta d\theta d\phi = 1. \quad (22)$$

If we now assume that the receiving antenna has a voltage gain function $g_R(r)$ and a radiation resistance R, then it can easily be shown using (16) or (18) that the current in a load matched to the receiving antenna is

$$I = \frac{k_0}{4\pi}\sqrt{\frac{P_T}{2R}} \int \frac{\Delta\epsilon(r')}{\epsilon_0} \frac{g_T(r')\cdot g_R(r')}{R_0 R_1} \cdot e^{i(0k\cdot r_0 + 1\cdot r_1)} e^{iK(r_k')\cdot r'} dr'. \quad (23)$$

The scalar product of the gain functions picks out just that component of the effective incident field [see (18)] which is accepted by the receiving antenna.

In a final application of the quasistatic approximation, we note that the quantities in the integrand of (23), with the exception of $\Delta\epsilon$ and exp $[iK\cdot r]$, vary only slightly in distances which are large compared with the

correlation distance of $\Delta\epsilon$. The scattering volume may thus be broken up into smaller volumes, many correlation distances on a side in each of which the Fraunhofer approximation, (18), applies. We may, in fact, completely neglect the term exp $\{i[k_0 \cdot r_0 + k_1 \cdot r_1]\}$ since the phases in different subvolumes are uncorrelated in any case. The contributions of the subvolumes to the received current are, of course, incoherent.

Statistical Considerations

Distribution of Received Signal

We have assumed that the scattering is taking place in a region which is large compared to the largest eddies, which are roughly regions with dimensions the size of a correlation distance of $\Delta\epsilon$. (These largest eddies are the "blobs" of heuristic turbulence theories.) We have also seen, at the end of the last section, that the other factors in the received field (or current) change slowly over many correlation distances, insuring that there are many eddies in the same region having the same characteristics. It is further reasonable to conclude from turbulence theories[5] that, since the motions well within the large eddies do not depend on the boundary conditions, the states of similar largest eddies, though statistically identical, are statistically independent.

The received signal may thus be thought of as the sum of a large number of independent electrical signals (each corresponding to a different part of the scattering volume) with the same statistics. If we consider the (mn)-dimensional random variables consisting of the values of the independent signals at m different points at each of n arbitrary times, the generalized Central Limit Theorem[6] states that the sum (*i.e.*, the received signal at those points and times) is asymptotically normally distributed. Stated differently, the received signal is a Gaussian process in space and time. (The process is, in fact, a narrow-band Gaussian noise, since the variations in amplitude and phase are slow compared to the rf.)

If the scattering region has several subvolumes differing in some characteristic such as intensity of turbulence or antenna pattern, the signal from each subvolume is Gaussian, as above. The total signal is therefore also Gaussian and its spectrum is the sum of the individual spectra. The characteristics of the received signal are thus completely determined by the mean power and correlation functions (or spectra) in space and time.

As already noted, an immediate implication of this conclusion is that the one-dimensional distribution of the signal is Gaussian and that of its envelope is Rayleigh. Considerably more complex statistical tests would entail finding joint distributions at a number of different times and places, all of which must conform to the Gaussian character of the signal. A note of caution may be required in that the signal is not strictly a Gaussian process for any finite number of components, and a sufficiently fine analysis of the received signal will produce some departure from the Gaussian character.

Mean Received Power

Using the approximations already stated, and defining a (normalized) correlation function of $\Delta\epsilon$ by

$$\langle \Delta\epsilon(r')\Delta\epsilon(r'')\rangle = \langle \Delta\epsilon^2(r')\rangle R(r' - r''), \tag{24}$$

we find from (22) that the mean received power

$$P_R = \frac{\langle |I|^2\rangle R}{2}$$

$$= \frac{k_0^2 P_T}{64\pi^2} \int \frac{(g_T(r)\cdot g_R(r))^2}{R_0^2 R_1^2} \frac{\langle \Delta\epsilon^2(r)\rangle}{\epsilon_0^2} S(K(r))dr \tag{25}$$

where

$$S(K) = \int R(u) e^{iK\cdot u} du. \tag{26}$$

$S(K)$ is thus the component of the spectrum of $\Delta\epsilon$ corresponding to the wave number K (which may be a function of position). These expressions could be somewhat generalized by including a dependence on position of the correlation function (hence the spectrum). It is however, precisely the conclusion of the dimensional theories of tubulence that the spectrum is a universal function in the inertial range to which the theory applies. The only dependence on position to be expected in the correlation function of $\Delta\epsilon$ is the normalizing parameter, related to the intensity of turbulence, shown explicitly in (24).

The expression for P_R exhibits the contributions from different regions and, in particular, the factors which effectively limit the "region of integration;" *i.e.*, the region from which most of the power is scattered into the reciever. The first term in the integrand gives the common region of illumination of the two antennas (together with the attenuation due to the expansion of the wavefronts with distance). The case where this factor limits the region of integration is treated by Booker and de Bettencourt[7] and implicitly by Villars and Weisskopf[8] and other Fraunhofer treatments. The last term gives the decrease of scattered power with increasing angle of scattering (recall that K is determined geometrically by the angle of scattering). This may be the limiting factor if the antenna beam is fairly wide. Finally, $\langle \Delta\epsilon^2(r)\rangle$ may be effectively nonzero only in a limited region of space; *e.g.*, a layer of turbulence. The extent to which the region of integration is deter-

[5] See for instance C. F. v. Weizsäcker, "Das spectrum der turbulenz bei grossen reynoldsschen zahlen," *Z. Phys.*, vol. 124, pp. 614–627; 1948.

[6] H. Cramér, "Mathematical Methods of Statistics," Princeton University Press, Princeton, New Jersey, p. 316; 1946.

[7] H. G. Booker and J. T. deBettencourt, "Theory of radio transmission by tropospheric scattering using very narrow beams," Proc. IRE, vol. 43, pp. 281–290; March, 1955.

[8] F. Villars and V. F. Weisskopf, "The scattering of electromagnetic waves by turbulent atmospheric fluctuations," *Phys. Rev.*, vol. 94, pp. 232–240; April 15, 1954.

mined by these three (or four) factors must, of course, be determined in each case. Obviously, if one factor strongly predominates, the others may be taken to be constant, thus simplifying (25) still further.

The scattering process can, alternatively, be described by the mean scattering cross section per unit volume; *i.e.*, the average power scattered per unit volume into a unit solid angle when the incident field has unit power per unit area (thus the dimensions are those of inverse length). This formulation has the advantage of depending only on the characteristics of the scattering region, and not on the antenna patterns, transmitted power, etc. (The received power is then determined by the incident power, scattering volume, and receiving antenna gain, so that these quantities must, of course, be known to extract the scattering cross section from any experimental data.) Note that the introduction of a quantity which, when multiplied by the relevant volume, gives the total power scattered in a given direction presumes that the process is incoherent.

From (25) we can see that the mean cross section per unit volume is

$$\sigma(r, K) = \frac{k_0^4}{16\pi^2} \frac{\langle \Delta\epsilon^2(r) \rangle}{\epsilon_0^2} S(K(r)) = \frac{\pi^2}{\lambda^4} \frac{\langle \Delta\epsilon^2(r) \rangle}{\epsilon_0^2} S(K(r)). \quad (27)$$

Finally, in a volume V, in which $\langle \Delta\epsilon^2(r) \rangle$ and $K(r)$ are effectively constant, (27) may be rewritten for any point in V as

$$\sigma(K) = \frac{\pi^2}{\lambda^4} \frac{1}{V\epsilon_0^2} \langle | \Delta\epsilon(K) |^2 \rangle \quad (28)$$

where

$$\Delta\epsilon(K) = \int_V \Delta\epsilon(r) e^{iK \cdot r} dr.$$

V in this case need not be identified with any physically significant volume. It may be picked arbitrarily, as long as its dimensions are large compared with a correlation distance of $\Delta\epsilon$, yet small enough for the indicated conditions.

Correlations of the Received Signal

For a given (fixed) transmitter, we note that the only quantities in (23) which are at our disposal to vary are the time in $\Delta\epsilon(r, t)$ and the vector $K(r)$. The general (normalized) correlation function between the currents resulting from two such situations is

$$\rho = \frac{\langle I_1 I_2^* \rangle}{\langle | I |^2 \rangle}$$

$$\alpha \int \langle \Delta\epsilon(r', t_1) \Delta\epsilon(r'', t_2) \rangle \frac{(g_T(r') \cdot g_R(r'))}{R_0^2 R_1^2} e^{iK_1(r') \cdot (r' - r'') + i\Delta K(r'') \cdot r''} dr' dr'' \quad (29)$$

where $\Delta K = K_1 - K_2$. The assumption made is that the change between the two conditions is so slight that I_1 and I_2 have the same mean amplitude, and the scattering volume is substantially the same for both cases. (Insofar as the volumes are different, those contributions are clearly uncorrelated, but the effect is negligible for practical systems.)

The expression in (29) (actually only the real part of it) is the rf correlation of the received signals. It may be related to the correlations ordinarily measured; *i.e.*, those of amplitude and phase.[9] In particular,

$$R_A = \frac{\pi}{4 - \pi} \left(\frac{1}{4} \rho^2 + \frac{1}{64} \rho^4 \cdots \right) \quad (30)$$

is the expression for the amplitude correlation function R_A.

If the correlation is simultaneous, $t_1 = t_2$, and (29) may be rewritten

$$\rho\alpha \int \frac{(g_T(r) \cdot g_R(r))^2}{R_0^2 R_1^2} \langle \Delta\epsilon^2(r) \rangle S(K(r)) e^{i\Delta K(r) \cdot r} dr. \quad (31)$$

In particular, for frequency correlation

$$\Delta K(r) = \frac{\Delta\omega}{\omega} K(r) \quad (32)$$

and for space correlation it can easily be seen that

$$\Delta K(r) = -\Delta K_1(r) = -\frac{K_0}{R_1} \hat{a} \times (\hat{a} \times s) \quad (33)$$

where s is the vector displacement of the second receiver from the first.

In effect then, these correlation functions are Fourier transforms of the distribution of power contributed by different parts of the scattering volume. Equivalently, they may be thought of in terms of an "angular spectrum."[10] In any case, the significant feature of (31) is that only insofar as the scattering volume is controlled by the falloff of the spectrum is the correlation function any indication of the characteristics of the turbulence. Insofar as the other factors affect this volume (for instance, by using high-gain antennas), the correlation function is determined by geometrical considerations.

In evaluating (31) (even assuming the scattering volume is determined completely by the spectrum), one cannot expect more than order-of-magnitude agreement with experimental correlation functions unless one uses much greater accuracy than is ordinarily done. Al-

[9] R. Price, "A note on the envelope and phase-modulated components of narrow band Gaussian noise," IRE TRANS, vol. IT-1, pp. 9–13; September, 1955.

[10] H. G. Booker and P. C. Clemmow, "The concept of an angular spectrum of plane waves, and its relation to that of polar diagram and aperture distribution," *Proc. IEE*, pt. III, vol. 97, pp. 11–17; January, 1950.

so, the spectrum $S(K)$ is itself still a matter of much conjecture, so a verification of a hypothesis which depends to some extent on a particular form of $S(K)$ must, at least to that extent, be considered uncertain. A case in point is a recent attempt[11] to show that experimental space correlation curves, which are broader than expected, could be explained by assuming that atmospheric turbulence is anisotropic. In that derivation, a more refined volume integration would have produced a broader correlation curve without the assumption of anisotropy. Some effect would also be obtained by taking a spectrum which falls off more rapidly than the assumed one. It is also pertinent to note that one of the fundamental observations of the statistical turbulence theories[12] is that over distances much smaller than the dimension of the largest eddies, the dynamic laws are universal and isotropic despite the particular large-scale anisotropic source of the turbulence. (A reservation is required for the ionosphere, where the magnetic field continues to affect the dynamics of the flow of electrons on all scales and may well produce anisotropy.)

A test of theory is desirable which does not depend so critically on exact evaluation of complicated integrals or dubious approximations of antenna patterns. Such tests as frequency or angle dependence of received power have been proposed and are suitable, but difficulties of one sort or another have limited the accuracy with which such results can be stated. Another test which has thus far been largely neglected holds some promise not only of giving some insight into the mechanism of turbulence, but of distinguishing scattering by turbulence-induced fluctuations from all other proposed mechanisms for producing the fields we are attempting to explain. This test involves the frequency dependence of the time correlation function.

In analogy with (24) we might write

$$\langle \Delta\epsilon(r', t_1)\Delta\epsilon(r'', t_2)\rangle = \langle \Delta\epsilon^2(r')\rangle R(r' - r'', t_1 - t_2).$$

We should note, however, that this function is not the correlation function of the turbulent field since we have neglected the drift velocity of the entire field. The relation between the fixed coordinates and the moving coordinate system of the turbulent field is, of course, $r_f = r_m + Vt$, where V is the drift velocity, so that the proper analogy with (24) is

$$\langle \Delta\epsilon(r', t_1)\Delta\epsilon(r'', t_2)\rangle = \langle \Delta\epsilon^2(r')\rangle R(r' - r'' - V(t_1 - t_2), t_1 - t_2) \quad (34)$$

where the function $R(\Delta r, \Delta t)$ is the correlation function of $\Delta\epsilon$ in space and time in the moving coordinate system of the field and is the one normally discussed in papers on turbulence.

It is clear from the geometry [or from an expression such as (9)] that a receiver moving with an appropriate velocity ($2V$ if the reciever and transmitter are equidistant from the scattering volume) has approximately the same effect as if there were no drift in the turbulent field. Thus the time correlation function at a fixed location has two influencing factors. First, the space pattern is being swept by at the drift velocity,[13] causing, among other things, the maxima of cross correlations between spaced antennas to be displaced from the origin. The effect of this motion on the autocorrelation function, as well as the effect of all models in which waves of all frequencies are reflected or scattered from the same obstacles, is that of a Doppler effect and hence proportional to frequency. The other influence is the change actually occurring in the turbulent field, exhibited by (34). The crux of the matter here is that the "correlation time" (or, equivalently, the fading rate, defined either as the reciprocal of a "correlation time" or in terms of mean crossings) for a given frequency is determined by the length of time required for inhomogeneities involved in scattering that frequency to change their configuration. The fading at any frequency can still be thought of as a Doppler effect from the moving eddies, but the eddies of different sizes involved in scattering different frequencies may move at different speeds.[14] In particular, the von Weizsäcker-Heisenberg theory concludes that eddies of length L move with speeds proportional to $L^{1/3}$. Thus we can expect that the fading rate would be proportional to the $\frac{2}{3}$ power of the frequency. (This result is the same whether we attribute the fading to changes in position due to the random motions or to the actual decay in the turbulent field. The dimensional theory states that the lifetime of an eddy is the time required to move its own length.)

The observed fading rate may thus be expected, if this picture is correct, to depend on a power of frequency somewhere between $\frac{2}{3}$ and 1, closer to the latter if the "correlation time" due to the drift velocity is much less than that due to the turbulence, close to the former if the reverse is true. Actually, the frequency dependence is somewhat clouded by the fact that the eddies involved are those of the effective wavelength $1/|K|$. Since the off-center scattering effectively takes place at a higher frequency, the observed correlation function is a weighted average of correlation functions corresponding to slightly different frequencies.

Two recent papers[15,16] have presented data on fading rates at different frequencies in tropospheric scatter

[11] H. Staras, "Forward scattering of radio waves by anisotropic turbulence," PROC. IRE, vol. 43, pp. 1374–1380; October, 1955.

[12] G. K. Batchelor, "The Theory of Homogeneous Turbulence," Cambridge University Press, Cambridge, Eng., p. 110; 1953.

[13] This is the model of H. G. Booker, J. A. Ratcliffe, and D. H. Shinn, "Diffraction from an irregular screen with applications to ionospheric problems," *Phil. Trans.*, vol. 242, pp. 579–607; September, 1950.

[14] This observation has been made independently by A. D. Wheelon (private communication).

[15] L. G. Trolese, "Characteristics of tropospheric scattered fields," PROC. IRE, vol. 43, pp. 1300–1305; October, 1955.

[16] K. A. Norton, P. L. Rice, H. B. Janes, and A. P. Barsis, "The rate of fading through a turbulent atmosphere," PROC. IRE, vol. 43, pp. 1341–1353; October, 1955.

experiments. In each case the author attempted to fit the data to the linear dependence predicted by the simple Doppler picture but found that the increase in fading rate appeared to be too slow, as expected from the model just presented.

To verify this hypothesis, experiments should be undertaken at widely spaced frequencies (consistent with the requirement that the eddies involved be in the inertial turbulence range) so that a power law may be more critically tested. The records should be taken simultaneously since the fading rate changes markedly in time[16] (although in the ionosphere the fading rate seems to be remarkably constant).[17] The relative fading times of drift and decay patterns could be judged by cross-correlating two antennas separated by a space correlation distance in the direction of drift. If the maximum correlation (at the displaced time, of course) is large, the fading at a point is due mainly to the drift and the turbulent effect will be masked. If the correlation is very small, the main effect is turbulent decay. (In theory, of course, the turbulent effect can always be measured by running along with the drift.) Finally, the antenna patterns should be as narrow as possible to keep the correlation function as free of dissimilar contributions as possible.

Appendix

According to (17), the received first-order scattered field is proportional to the Fourier transform of $f_0(r)$ corresponding to the wave number K. (We shall use the notation $T_K\{f_0(r)\}$ for this quantity in this Appendix.) Thus the statement leading to (18) will be proved if we can show [see (8)] that

$$(\varepsilon - \hat{u}\hat{u})\cdot T_K\left\{\nabla\left(\frac{1}{\epsilon}\nabla\epsilon\cdot E_0\right)\right\} = 0 \tag{35}$$

and

$$(\varepsilon - \hat{u}\hat{u})\cdot T_K\left\{2\left(\nabla\frac{1}{\epsilon}\cdot\nabla\right)D_0 + D_0\nabla^2\frac{1}{\epsilon}\right\} = 0. \tag{36}$$

We shall retain only first order terms in $\Delta\epsilon$ and replace ∇ by ik_0 when it operates on E_0 or $D_0=\epsilon_0 E_0$.

To prove (35), we write

$$\nabla\left(\frac{1}{\epsilon}\nabla\epsilon\cdot E_0\right)$$

$$\sim\frac{1}{\epsilon_0}[(E_0\cdot\nabla)\nabla\epsilon + (\nabla\epsilon\cdot ik_0)E_0 + \nabla\epsilon\times(ik_0\times E_0)]. \tag{37}$$

It is easily shown that

$$T_K\{\nabla f(r)\} = -iKT_K\{f(r)\} \tag{38}$$

so that

$$T_K\left\{\nabla\left(\frac{1}{\epsilon}\nabla\epsilon\cdot E_0\right)\right\}$$

$$\sim\frac{1}{\epsilon_0}[-(E_0\cdot K)K + (K\cdot k_0)E_0 + K\times(k_0\times E_0)]T_K\{\Delta\epsilon\}$$

$$=\frac{1}{\epsilon_0}T_K\{\Delta\epsilon\}(E_0\cdot K)(k_0 - K)$$

$$=\frac{1}{\epsilon_0}T_K\{\Delta\epsilon\}(E_0\cdot K)k_1. \tag{39}$$

But by definition of $\hat{u}$, $k_1=k_0\hat{u}$, and since $(\varepsilon-\hat{u}\hat{u})\cdot\hat{u}=0$, (35) is proved. It appears then that the additional term in $F(r)$, due to the fact that $\nabla\cdot E\neq 0$, corresponds to a longitudinal excitation in the direction of scattering and gives no far field. Note, however, that the magnitude of this excitation is not small compared with the one which does produce a far field, hence cannot be neglected on these grounds.

The proof of (36) is similar and does not even require the use of the dyadic.

$$T_K\left\{2\left(\nabla\frac{1}{\epsilon}\cdot\nabla\right)D_0 + D_0\nabla^2\frac{1}{\epsilon}\right\}$$

$$\sim -\frac{1}{\epsilon_0}T_K\{2(\nabla\epsilon\cdot ik_0)E_0 + E_0\nabla^2\epsilon\}$$

$$= -\frac{1}{\epsilon_0}T_K\{\Delta\epsilon\}[2(K\cdot k_0) - K^2]E_0$$

$$= 0$$

since $K=k_0-k_1$ and $|k_0|=|k_1|=k_0$.

Acknowledgment

The author would like to express his appreciation to Dr. R. A. Silverman for many helpful suggestions and discussions on the subjects herein discussed.

[17] G. R. Sugar, "Some fading characteristics of regular vhf ionospheric propagation," Proc. IRE, vol. 43, pp. 1432–1436; October, 1955.

Scanning Characteristics of Microwave Aplanatic Lenses*

G. G. CLOUTIER† AND G. BEKEFI‡

Summary—**The imaging properties of two types of solid dielectric, circularly symmetric lenses were studied at a wavelength of 1.25 cm. One of these was a wide-angle aplanat proposed some time ago by Martin; the other was a modification of the two-point corrected lens recently discussed by Sternberg. The work was carried out for the purpose of finding their scanning characteristics and to compare their ability to produce good pencil beams of radiation. Measurements disclosed that in these lenses (having focal number of 1.5), a beam, of half-power width 1.25°, could be scanned up to about 20° of arc from the optical axis by displacement of the source. The presence of astigmatism prevented either lens from being employed for wider scanning angles. In view of this fact, there appears to be little advantage in this case in using the two-point corrected lens over the simple aplanat which can be more easily designed.**

Introduction

THE RANGE over which a pencil beam of radiation can be scanned by displacing the primary source transversely to the principal axis of a lens depends upon the degree to which the lens can be corrected for the off-axis aberrations. The amount of correction that can be achieved is governed by the number of optical surfaces available to the designer. A simple lens with two appropriately shaped surfaces can at best be free from spherical aberration and ordinary coma. Astigmatism, which becomes prominent at the larger angles of displacement, cannot be eliminated from a single thin lens having an aperture stop coincident with its plane; this is so, whether the lens consists of a number of cemented components or whether it has spherical or aspheric surfaces. Elimination of astigmatism requires more complex optical systems such as an extremely thick lens,[1] a system of separated lenses, or a lens with an aperture stop displaced away from it.[2] Due to certain difficulties, little use has been made to date of these methods of correcting for astigmatism at microwave frequencies;[3,4] most workers limit themselves to the simple two-surface lens. Of the latter there are two distinct types which have found much application. There are the wide-angle aplanats (that is, lenses corrected for spherical aberration and coma) based on the design of Martin[1] and Friedlander.[5] They are characterized by the fact that they are free from axial spherical aberration and that they fulfil the Abbe sine condition. Satisfaction of the latter condition implies that the optical system is free from ordinary coma;[2] that is, from all those types of coma which vary as the first power of the source displacement from the optic axis. By ignoring all higher powers of displacement, other than the first, it is indicated that coma will only be corrected for small displacements of the source. The answer as to how large these can be without causing bad deterioration of the diffraction image is best found by experiment.

Aplanatism in the above sense, namely the satisfaction of axial stigmatism and of the sine condition, may be expected to give insufficient correction when the source is displaced through quite large angles and if the lens has a small focal number. Higher orders of coma could then become significant. This fact led Ruze[6] to develop another type of lens system with which we shall also be concerned here. He designed two-dimensional metal plate lenses corrected exactly for spherical aberration and coma—astigmatism being absent in two-dimensional lenses illuminated by line sources—at two extra-axial object points. These foci are well displaced from the axis of the lens and are situated symmetrically on either side of it, *e.g.*, at angular distances $\pm\theta_0$. To insure good behavior of the lens over the whole region lying within $-\theta_0<\theta<\theta_0$, Ruze refined his design by requiring that a third, namely an axial point, also be corrected exactly. This he did by varying the refractive index across the lens.

A generalization of Ruze's method was given recently by Sternberg[7] for the design of two-point corrected solid dielectric lenses. Several three-dimensional circularly symmetric models were made by him from solid polystyrene and were found to have good scanning properties over the range of source positions contained within the two extra-axial foci. By keeping to homogeneous dielectric material of constant refractive index, Sternberg could not insure *a priori* good correction for his lens at and close to the axis in a manner similar to that used by Ruze in the three-point corrected systems. Hence, the scanning properties of this lens, if it is to be used in scanning, are left somewhat to chance and its good behavior outside the two focal points is somewhat fortuitous. Bekefi[4] reexamined Sternberg's method of design;

* Manuscript received by the PGAP, November 5, 1956; revised manuscript received May 28, 1957. This work forms part of a project on microwave optics that is supported at McGill University, in the Eaton Electronics Research Laboratory, by the USAF, Cambridge Res. Ctr., Cambridge, Mass. on Contract AF 19(122)-81.

† Dept of Physics, McGill University, Montreal, P. Q., Can.

‡ Mass. Inst. Tech., Cambridge, Mass., formerly at McGill University, Montreal, P. Q., Can.

[1] L. C. Martin, "Wide aperature aplanatic single lenses," *Proc. Phys. Soc.*, vol. 56, pp. 104–113; 1944.

[2] H. H. Hopkins, "Wave theory of aberrations," Clarendon Press, Oxford, England, pp. 132–136; 1950.

[3] R. C. Gunter, Jr., "On the two-element separated doublet," paper no. 36, Symposium on Microwave Optics, McGill University, Montreal, Can.; June, 1953.

[4] G. Bekefi, McGill University, Eaton Electronics Res. Lab., Final Report to the USAF Cambridge Res. Ctr., Contract AF 19(122)-81; March, 1957.

[5] F. G. Friedlander, "A dielectric lens aerial for wide-angle beam scanning," *J. IEE*, p. 111A, vol. 93, pp. 658–662; 1946.

[6] J. Ruze, "Wide-angle metal plate optics," PROC. IRE, vol. 38, pp. 53–59; January, 1950; also see "Correction," vol. 39, p. 697; June, 1951.

[7] R. L. Sternberg, "Elementary Methods in the Numerical Design of Microwave Dielectric Lenses," Lab. Electronics Rep., Boston, Mass.; 1954. Also see, *J. Math. Phys.*, vol. 34, pp. 209–235; January, 1956.

by permitting the presence of small errors in the two extra-axial object points and by examining the magnitude of the various aberrations, he was able to choose that design which appeared to give good correction not only at the extra-axial foci but also at a third axial point. The method of design, in many respects similar to Sternberg's, will be outlined below.

On comparing the two types of design discussed above, there appears little doubt that an antenna engineer, interested in a two-dimensional lens giving a fan shaped beam and irradiated by a line source, should turn to the latter design in preference to the ordinary aplanat if wide angle scanning is desired. The two- or three-point corrected lens will give two good extra-axial images; in the intermediate region of the scan, errors are also not too large. If the design is applied to constructing a three-dimensional circular lens with a view to obtaining a pencil beam, the question arises: due to the presence of astigmatism, can much improvement be achieved through the use of this system in place of the aplanat? Astigmatism causes a very bad deterioration of the image;[8] it is virtually independent of the shape of the lens surfaces and it increases as the square of the source displacement and inversely as the focal length. Hence the two lens types, if of equal size and the same focal length, would be afflicted by about the same amount of astigmatism. Although the aplanat may at the same time suffer from higher orders of coma at fairly large source displacements, an error which would be absent in the two- or three-point corrected lens, effects due to these lens errors may be completely overshadowed by astigmatism. Whether or not this happens it was one of the main considerations which prompted our investigations. The two types of lenses were constructed and designed to be of equal size and focal length. Measurements of the respective radiation patterns, made in such a way as to insure a pencil beam of radiation, showed that the range of scanning angles of the two lenses was about the same and that astigmatism was the major factor which limited their performance. It was therefore concluded that in the design of lenses having focal numbers in the range of 1.5, nothing is gained by employing the laborious methods required in the design of the two- or three-point corrected systems in place of the much more easily designed aplanats.

The procedures used in the design of the above types of lenses are outlined briefly below. For the sake of brevity, the Martin type of wide angle aplanat will be denoted as Lens A; the modified form of Sternberg's design as Lens B.

Lens A—Wide-Angle Aplanat

Let S_1 and S_2 be the two lens surfaces whose shape is to be determined [Fig. 1(a)]. A general ray proceeds at an angle γ from the paraxial focus F_0 which is situated

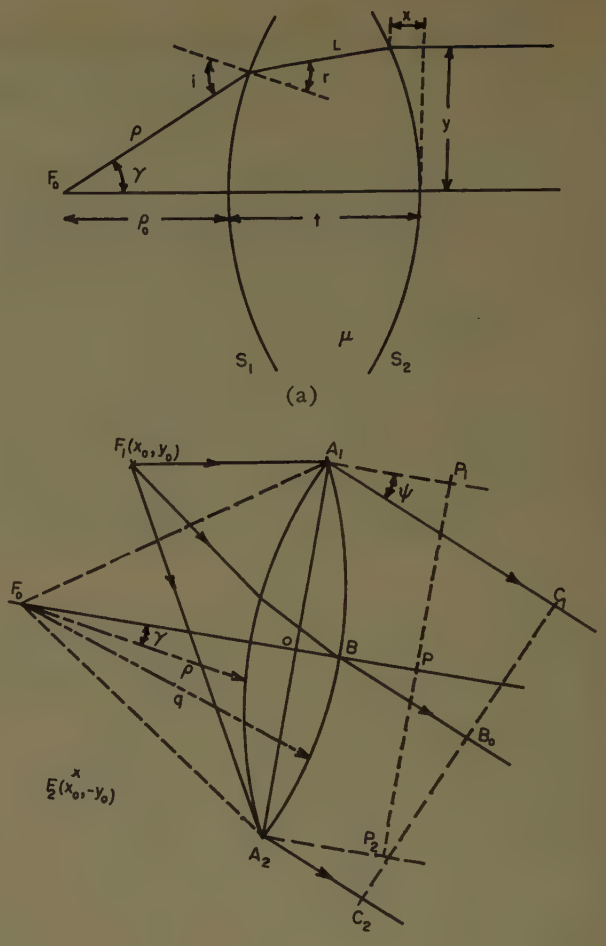

Fig. 1.

at some distance ρ_0 from the apex of surface S_1. The lens is made from a homogeneous material of refractive index μ and has a thickness t; i and r are the angles of incidence and refraction, respectively, at the first surface S_1, and (x, y) are the coordinates of the point of intersection of the ray with surface S_2. Freedom from axial spherical aberration requires path equality between all rays proceeding from F_0, namely

$$-x + \mu l + \rho = t(\mu - 1). \tag{1}$$

Freedom from ordinary coma is obtained by satisfying the sine condition which states that

$$y = F_p \sin \gamma \tag{2}$$

for an image at infinity. F_p is the paraxial focal length. From equations above, from Snell's law of refraction and from the lens geometry, one finds that the differential form of the equation for the first surface S_1 is given by[6]

$$\frac{1}{\rho}\frac{d\rho}{d\gamma} = \frac{\mu \sin \beta}{\mu \cos \beta - 1}$$

where $\beta = (i - r)$; the angles β and γ are found to be related through

$$\frac{(F_p - \rho) \sin \gamma}{t(\mu - 1) + \rho(\cos \gamma - 1)} = \frac{\sin (\gamma - \beta)}{\mu - \cos (\gamma - \beta)}.$$

[8] M. P. Bachynski and G. Bekefi, McGill University, Eaton Electronics Res. Lab., Tech. Rep. No. 35, February, 1955; also see, "Aberrations in circularly symmetric microwave lenses," IRE Trans., vol. AP-4, pp. 412–421; July, 1956.

An elimination of β between the two equations results in a differential equation for ρ in terms of the angle γ and the lens constants μ, F_p, t, and ρ_0. Martin[1] solved the equation by a power series expansion

$$\rho = \rho_0(1 + a_2\gamma^2 + a_4\gamma^4 + a_6\gamma^6 + \cdots) \qquad (3)$$

and evaluated the coefficients a_2, a_4, etc., in general form in terms of the lens constants.[9] Once these have been determined, the shape of the other surface is found by numerical ray tracing.

In the above design procedure, numerical values must be assigned eventually to the parameters μ, F_p, t, ρ_0. For a given refractive index and focal length the choice of values to be assigned to ρ_0 and t still remains open. This leaves room for some judicious guessing and several trial designs must be made to discover where the surfaces S_1 and S_2 meet, before one arrives at a lens having the correct aperture dimensions. The degree to which the final system is truly aplanatic depends on the angular size

TABLE I

Lens Parameters (All lengths normalized to one meter as unit of length)	Lens A (Wide-angle aplanat)	Lens B (Triple-point corrected lens)
Diameter $2a$	App. 1.00	1.00000
Paraxial focal length F_p	1.53533	1.53533
Refractive index of material μ	1.58900	1.58900
Lens thickness t (as measured along the principal axis)	0.14432	0.14432
Position of extra-axial foci F_1:		
x_0	—	1.00000
y_0	—	0.50000
f number	1.53533	1.53533
ρ_0	1.44733	1.44050
a_2	0.52638	0.45799
a_4	0.15832	0.07785
a_6	0.23960	—
q_0	—	1.58482
b_2	—	−0.41961
b_4	—	0.33074
Shape factor $X=-(R_1+R_2)/(R_1-R_2)$ (R_1 and R_2 are the paraxial radii of curvature of the two surfaces)	—	1.10585

TABLE II

γ in radians	0	0.05	0.10	0.15	0.20	0.25	0.30	0.325
Path length error (in units of 10^{-6} meter)	0	− 1	0	0	1	0	0	− 1 (equals −200 for Lens B)
osc$\times 10^6$	0	−59	+0.7	+11	+21	−29	−113	−235 (equals 12700 for Lens B)

subtended by the lens at the focus. If the maximum value of γ, say γ_0, does not exceed about 25°, coefficients higher than a_6 are not needed. Difficulties arise if the lens is wider than this; higher order coefficients are then required, which are not available due to difficulties in their evaluation. Trial and error methods of estimating such coefficients are discussed by Martin. However, in such a case, it is preferable and more accurate to determine the equation of the surface by direct numerical integration of the differential equation as was done by Friedlander.

A lens 50 cm in diameter having a focal number of about 1.5 was made from solid polystyrene plastic. The design parameters are given in the first column of Table I. All lengths are normalized to a unit of one meter. A check on the accuracy of the lens design was made in the following manner: the departure from axial stigmatism (*i.e.*, freedom from axial spherical aberration) was found by calculating the path length difference between rays proceeding from the focus at various angles γ and the axial ray. This path length difference in meters is given in the first row of Table II. The errors are seen to be extremely small. Departures from the exact fulfilment of the sine condition (known as the offense against the sine condition, or osc) was obtained from the relation[10]

$$\text{osc} = 1 - \frac{F_\gamma}{F_p}\left(1 + \frac{Y}{\rho_0}\right). \qquad (4)$$

This expression is a dimensionless quantity; F_γ is the "focal length" at an angle γ and is defined as $y/\sin\gamma$ where y is the height of the ray above the axis and parallel to it. Y is a quantity which determines the amount of spherical aberration in the system; it is given in terms of the distance between the paraxial focus and the point where some incident ray at height y will cross the axis after passing through the lens. If the lens is stigmatic or very nearly so, as in the present case, then the contribution from the term Y/ρ_0 is negligible. It will be seen from the second row of Table II that the osc is very small. In fact, both the errors tabulated lie well within the accuracy to which microwave lenses can be machined.

Lens B—The Two-Point Corrected Lens

As was mentioned previously, the Sternberg method of design which corrects exactly for two off-axis object points was modified somewhat in order to insure good correction also at an axial point. Consider a symmetrical lens [Fig. 1(b)] of size $A_1A_2=2a$ again made from a material of refractive index μ. F_1 and F_2 are the two extra-axial foci situated at the coordinate points (x_0, y_0), $(x_0, -y_0)$ with respect to the origin o. With the source at F_1, the plane wave whose wave front is C_1C_2, is required to emerge at some angle ψ to the optic axis. Having chosen the position of $F_1(x_0, y_0)$, the requirement of path

[9] Martin set F_y equal to unity and took this value as his unit of length.

[10] A. E. Conrady, "Applied Optics and Optical Design," Oxford University Press, New York, N. Y.; 1929.

equality of the rays $[F_1A_1C_1]=[F_1A_2C_2]$ determines the angle (ψ) which the emergent plane wave will make with the axis. The slopes of the surfaces at A_1 and A_2 are found next. This is done by considering each apex as a small prism and by using Snell's Law for the two rays $C_1A_1F_1$ and $C_2A_2F_1$ assumed to traverse the prisms infinitesimally close to the apices A_1 and A_2. By invoking symmetry conditions of the two halves of the lens about the principal axis, a unique answer for the slope of the surfaces at A_1 and A_2 results. From this knowledge the marginal focus F_0 is chosen as the center of the polar coordinates (ρ, γ), (q, γ) of the two lens surfaces. The equation of these surfaces is expressed as a power series in γ. To reduce the complexity of the calculations, it is assumed that three terms of the series suffice to define the surface,

$$\rho = \rho_0(1 + a_2\gamma^2 + a_4\gamma^4)$$
$$q = q_0(1 + b_2\gamma^2 + b_4\gamma^4). \tag{5}$$

The lens thickness, t, is then given by $(q_0-\rho_0)$. Six parameters, namely $\rho_0, q_0, a_2, a_4 b_2, b_4$, must be determined. Four quantities which can be substituted into (5) are known already: when γ has its maximum value γ_0, $\rho=q=F_0A_1$. The knowledge of the slopes at the surfaces A_1 and A_2 determines the values of

$$\frac{1}{\rho}\frac{d\rho}{d\gamma} \text{ and } \frac{1}{q}\frac{dq}{d\gamma} \text{ at } \gamma = \gamma_0.$$

A complete solution of the unknown parameters requires the tracing of one more ray through the system. For reasons of simplicity a ray B_0BF_1 passing through the center of the second surface was chosen. In place of satisfying exact path equality between this ray and the ray $C_1A_1F_1$, a small path error Δ_2 was allowed to be present. It is defined by

$$\Delta_2 = [C_1A_1F_1 - B_0BF_1]. \tag{6}$$

It was then found convenient to study variations of this path error as a function of another path error (Δ_1) which is allowed to exist between the marginal and axial rays, namely

$$\Delta_1 = [P_1A_1F_0 - PBF_0]. \tag{7}$$

If the latter error were zero, the system would be free from spherical aberration for the axial and marginal rays. However, the paraxial rays could still deviate from path equality and this would depend on the radii of curvature of the surfaces near the axis.

For a given preassigned path error Δ_1, Δ_2 and all the lens parameters were evaluated. The amount of spherical aberration and the offense against the sine condition were then computed. This was repeated for various values of Δ_1 and the design chosen resulted in the most reasonable combination of lens errors. A lens was designed in this manner, and the final parameters are given in the second column of Table I. All physical distances are normalized to twice the aperture size

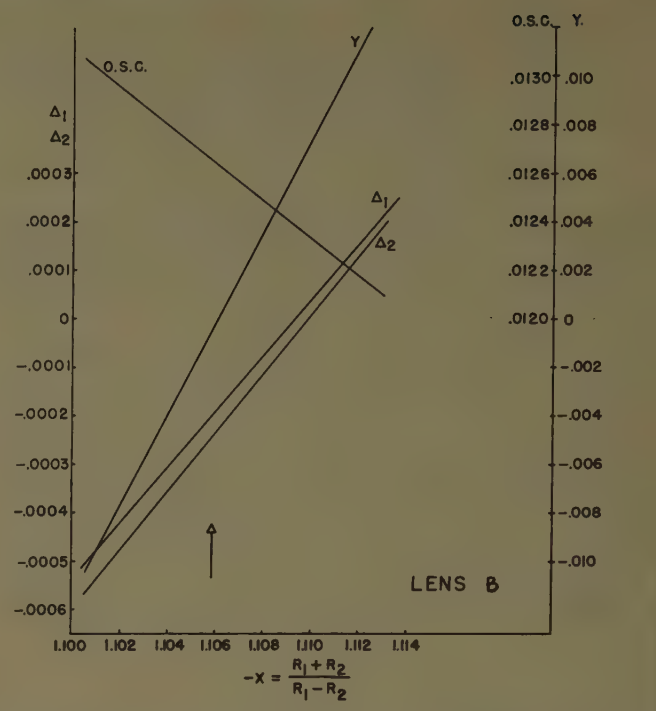

Fig. 2—Aberrations in the "three-point" corrected lens B as function of small variations in the shape factor X. The arrow indicates the most promising design, details of which are given in Table I [osc is the offense against the sine condition; Y is the magnitude of spherical aberration Δ_1 and Δ_2 defined by (6) and (7); all lengths normalized to the unit length of one meter].

($2a=A_1A_2$) which is taken as the unit of distance of one meter. The variations of the lens errors as a function of the design are shown in Fig. 2. All lengths are expressed in units of one meter. It was found convenient to plot these variations vs the shape factor of the lens defined as

$$X = -\frac{R_1 + R_2}{R_1 - R_2},$$

where R_1 and R_2 are the paraxial radii of curvature of the two surfaces. The graphs denoted by Δ_2 and Δ_1 are the path length errors as defined by (6) and (7), respectively. Y is the spherical aberration expressed as the distance between the positions of the paraxial and marginal foci; it is taken to be positive when the marginal focus lies between the lens and the paraxial focus and negative when it lies outside this region. It should be remarked that this time Y has been calculated only for the marginal ray in contrast to the previous case where it was computed for intermediate rays also. A reference to the last column of Table II will also show that the present lens has about 200 times as much spherical aberration as the Martin aplanat. The offense against the sine condition (for the marginal ray only) is also depicted in Fig. 2. It is seen to vary little with change in the shape factor and it is nearly 55 times greater than in the previous lens (see Table II). However, it must be stressed that despite the considerably greater aberrations this lens shows on and near the axis as compared with the Martin aplanat, the errors remain

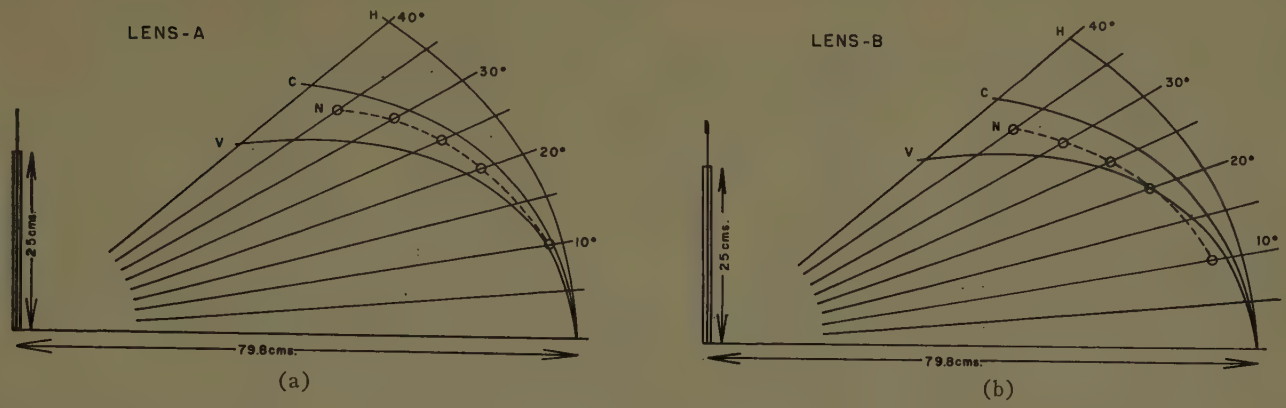

Fig. 3—The scanning arc followed by a primary source irradiating lenses A and B, respectively. *V* and *H* are the planes containing the vertical and horizontal focal lines, respectively; *C* is the central plane and represents the arc followed by the source thus insuring a pencil beam of radiation; *N* is the line followed by the source and giving a symmetrical image that is sensibly free of coma.

very small when dealing with centimeter waves.

While the offense against the sine condition varies little with the shape factor, the spherical aberration changes very rapidly. It will also be noted that when the extra-axial image becomes "free" of image errors ($\Delta_2=0$), as is the case in Sternberg's design, the axial spherical aberration Y is fairly significant. This was found to be particularly so when lenses having a smaller f number were designed by this method. Hence it would appear that in order to insure a good axial focus, it is advantageous to allow some residual error Δ_2 to remain in the extra-axial focus. When lenses with very small f numbers are desired with greatly displaced extra-axial foci, the present method of design is too crude and more terms are required in the series expansion (5). The computational work, however, increases immensely and such refinements in design are discussed by Sternberg.

A polystyrene lens was constructed according to the design data given in the second column of Table I. The lens is a shallow miniscus with its concave side facing the source. This can be compared with the previous lens, which is found to be doubly convex.

Radiation Patterns of the Lenses

The radiation patterns of the lenses were measured on an outdoor site at a wavelength of 1.25 cm. The lenses were mounted in a large metal screen which acted as the aperture stop and prevented energy other than that traversing the lens from reaching the image space. The primary source was an open waveguide; this insured virtually constant illumination over the lens surface. Radiation patterns were then obtained for various angular displacements θ of the source from the principal axis. That path traced out by the primary source was chosen [Figs. 3(a), 3(b)] which gave in each case a pencil beam of radiation. In order that this may be achieved, the source must be moved along a line lying midway between the astigmatic focal lines, namely along an arc in the central plane of the optical system. This is the arc C shown in Fig. 3(a) and 3(b). Departures from this arc will cause an elongation of the radiation pattern in a plane corresponding to the particular focal line which the source approaches. Corrections for coma can only be made for a conjugate pair of object and image distances. Hence, with the image distance fixed, there must exist an arc in a coma corrected system along which a displacement of the source will produce a symmetrical image sensibly free from coma. Such an arc [denoted by N in Fig. 3(a) and 3(b)], was found experimentally. If the source is displaced on either side of this arc, the image becomes asymmetrical and these asymmetries are nearly mirror images of each other. The reason for this is, of course, that coma changes sign when the source crosses the arc N. If these arcs (N and C) are widely removed from each other, one is faced with the problem as to which arc to choose for purposes of scanning. If path N is chosen, the radiation pattern will be free from coma but elongated in one plane; if path C is chosen, the main lobe is almost rotationally symmetrical but asymmetry of the side lobe levels appears in the plane of scanning due to the presence of coma. For the purposes of comparing the scanning characteristics of lenses A and B, it was found necessary to move the source along the arc C since this arc was identical in both systems, astigmatism being the same. Since in Lens B the arc N lies further away from the central plane than in Lens A, asymmetries in the pattern of this lens are somewhat greater.

In Fig. 4(a) and 4(b) are shown radiation patterns of the two lenses for several angular source displacements θ. Both lenses behave equally well on axis and computations show that the patterns approach very closely the ideal aberration-free image obtained from a perfect uniformly illuminated lens. As the angle of scan increases, slight asymmetries, mainly in Lens B, are observed; they are due to coma. The filling in of the minima, the broadening of the main lobe, and the increase in side lobe levels at the greater angles θ, is the result of astigmatism.[8] At an angle of 30° these effects are so bad that the pattern would not be usable in most applications. The circles shown in the graphs represent data computed from the diffraction theory of optical

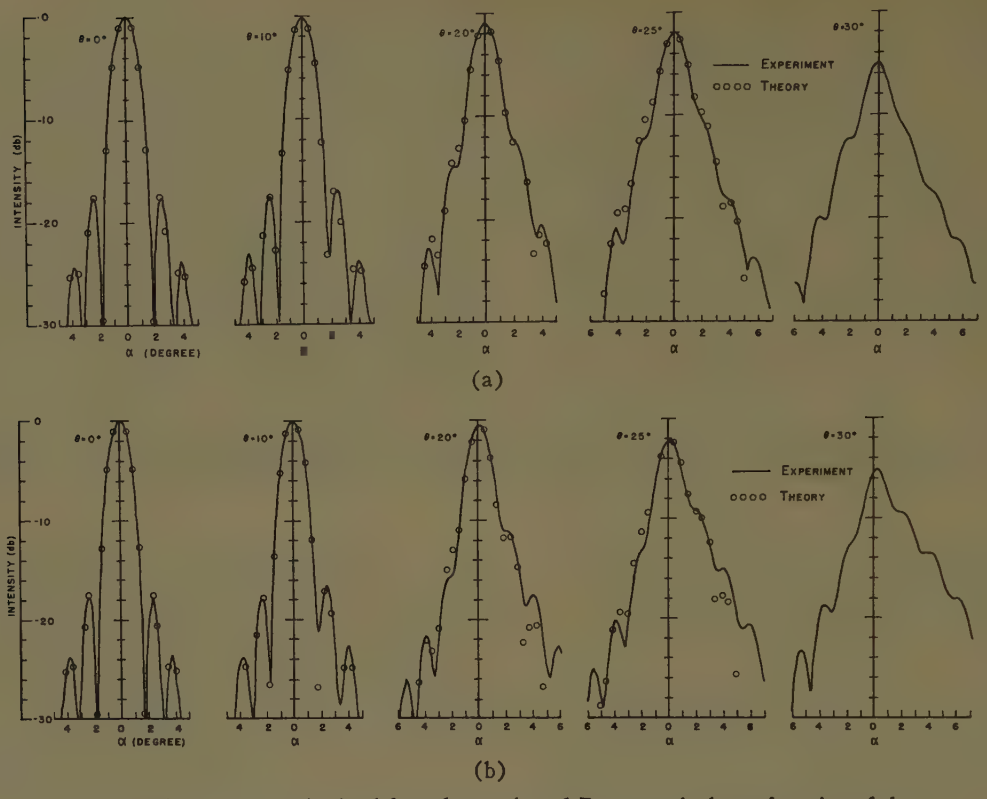

Fig. 4—Radiation patterns obtained from lenses A and B, respectively, as function of the scanning angle θ; α is the angle of diffraction; the source was displaced along the central plane.

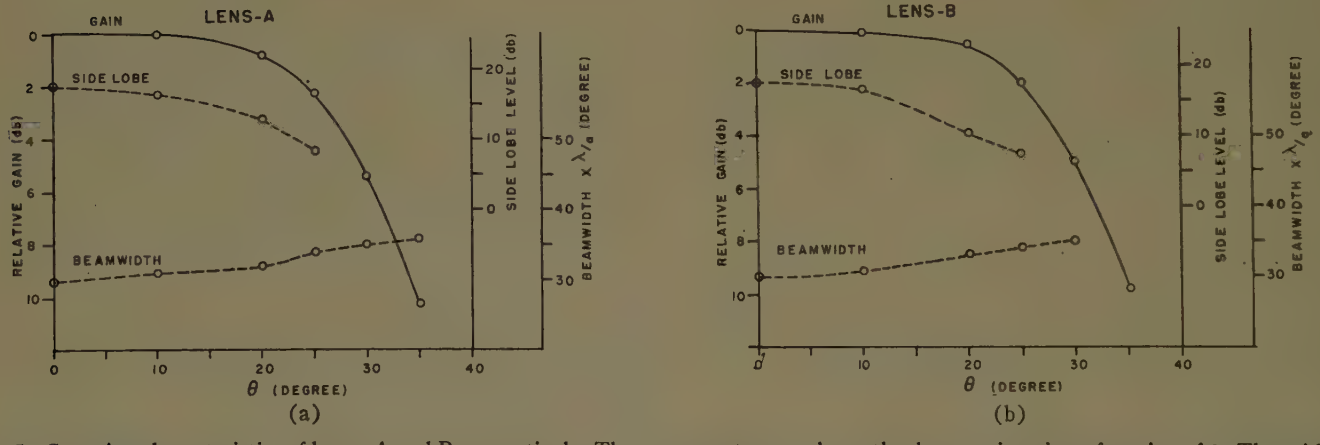

Fig. 5—Scanning characteristics of lenses A and B, respectively. The uppermost curve shows the decrease in gain as function of θ. The middle curve gives the variation of the first side lobe levels relative to the central maximum, and the bottom curve is that of the half-power beam widths.

aberrations.[11] The predictions from theory are seen to be extremely good except at the large angles of source displacement.

The measured loss in gain relative to that when the source is on axis, the variations of the height of the first side lobes, and the change in the half-power beam width of the main lobe are shown graphically in Fig. 5(a) and 5(b), as a function of the scanning angle θ. These and previous results indicate that there is little to choose between the actual performance of the lenses. As mentioned before, astigmatism is the predominant factor which limits the degree of scanning that can be obtained; in fact, it is so pronounced at the larger angles that it is impossible to tell whether the more elaborate design of Lens B results in a system which is better corrected for coma than is the simple aplanat.

[11] G. G. Cloutier, "Scanning characteristics of some microwave aplanatic lenses," M.S. thesis, McGill University; 1956.

Acknowledgment

The authors are greatly indebted to Miss M. E. Dougherty who carried out many of the computations; they also wish to acknowledge their appreciation to Professor G. W. Farnell for the many interesting discussions and to Professor G. A. Woonton for his interest in this work. G. G. Cloutier was assisted by a bursary, a studentship, and a summer supplement from the National Research Council of Canada.

communications

The Long Distance Horizontal Radiation Pattern of a High-Frequency Antenna*

RICHARD SILBERSTEIN†

TESTS were conducted in 1953, at the National Bureau of Standards, to compare the radiation pattern of a directive high-frequency antenna observed at a great distance with that determined locally. The array consisted of two three-element vertical yagis spaced a half wavelength apart with the center of the array about a half wavelength above ground. The horizontal beamwidth of the array was 50° and the operating frequency near 13.7 mc.

In the first series of tests, transmissions were made from Sterling, Va., at various azimuths in accordance with a prearranged schedule with reception by a number of foreign and domestic laboratories. The antenna array was rotated through 340° in steps of 10° once each day for two weeks. At the distant stations records were made of the field strengths of these emissions and simultaneous emissions on a vertical doublet. Data for each day were scaled and smoothed and the field strength values on each azimuth expressed as a ratio of amplitude for the array to amplitude for the doublet. Medians for the test period were then taken for each azimuth and normalized to the value for the axis of structural symmetry of the array. These data were then plotted and compared with the local radiation pattern.

In the second series of tests the antenna was used for reception of a distant station and rotated once a minute for about an hour in each test. Medians were taken of the data on each azimuth and the values normalized.

In both series of tests there was no appreciable distortion of the median pattern by the ionosphere as judged by comparison with the pattern measured locally, even under poor propagation conditions. Fig. 1 illustrates the long-distance pattern at 3650 km compared with the local pattern.

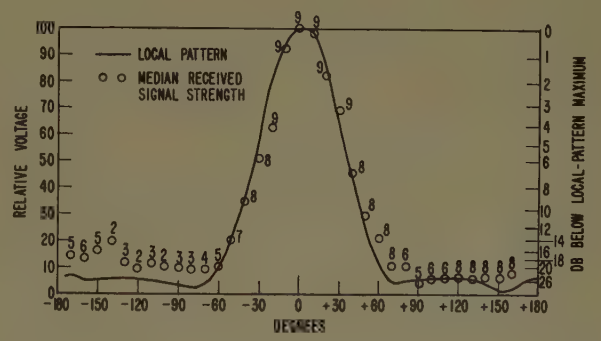

Fig. 1—Sterling, Va., yagi radiation pattern for reception at San Diego, Calif., February, 1953.

It is concluded that many instances of unexpected station interference attributed to differences between the distant and local patterns of an antenna may be more properly interpreted as instances of unusually high values of field strength, which is a time-distributed quantity. Unusually low values of field strength from the station it is desired to receive would also be a factor.

Details of the experiment and the analysis are to be found in a report.[1] The report also gives some information on instrumentation problems under the severe requirement of minimizing interference in the reception tests.

* Manuscript received by the PGAP, June 23, 1956; revised manuscript received, May 22, 1957.

† Natl. Bureau of Standards, Boulder, Colo.

[1] R. Silberstein, "The Long Distance Horizontal Radiation Pattern of a High-Frequency Antenna," Natl. Bureau of Standards Rep. No. 3538; July 6, 1955.

Surface Fields Produced by a Slot on a Cone*

G. HELD† AND G. HASSERDJIAN†

THIS paper presents an experimental study of the field distribution on the surface of a cone excited by a slot, and the degree of interaction between the slot and the tip of the cone.

In order to measure the field distribution on the cone surface, a small rod scatterer was supported perpendicular to the cone surface. By measuring the "secondary" field radiated by the scatterer, placed at desired points, the field distribution was determined. The field intensity at a point can be measured by detecting a "secondary" field caused by a small scatterer placed at the field point.[1] The experimental setup for these measurements is shown in Fig. 1.

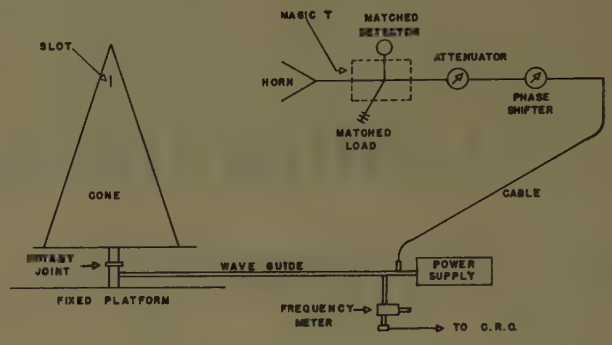

Fig. 1—Measurement setup.

As a source of excitation on the cone surface, two types of resonant slots were considered. First, a slot of length $\lambda/2$ was studied which was cut along an element of the cone. Fig. 2 shows the measured distribution of the normal electric field along various elements of the cone for such a slot. Since the electric field distribution along the elements between the slot and the tip indicated no standing waves, it was concluded that a longitudinal slot did not interact with the tip.

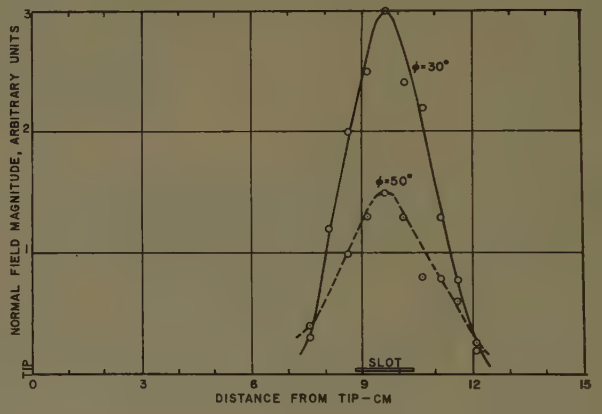

Fig. 2—Field distribution due to elemental slot excitation.

Second, a $\lambda/2$ slot was cut circumferentially and the field distribution on the cone surface was measured. Fig. 3 shows the measured distribution along various elements of the cone for such a slot located 2.81λ from the tip. The $\phi=0°$ curve represents the distribution along the element passing through the center of the slot. These curves show standing waves which indicate interaction between the tip of the cone and the slot.

In order to present the experimental results in the form of tip to slot interaction, the cone surface was unfolded into a planar surface with the $\phi=180°$-element of the cone constituting the edge of this plane. It was assumed then, that the normal electric field on this surface could be represented by the expression

$$E_n = f(\theta')G_1(kr) + AG_2(kr_0) \qquad (1)$$

where the first term represents the radiation from the slot and the second term, the reflection from the tip. For a half-wavelength slot the coefficient of G_1 would be

$$\frac{\cos\left[\pi/2\cos\theta'\right]}{\sin\theta'},$$

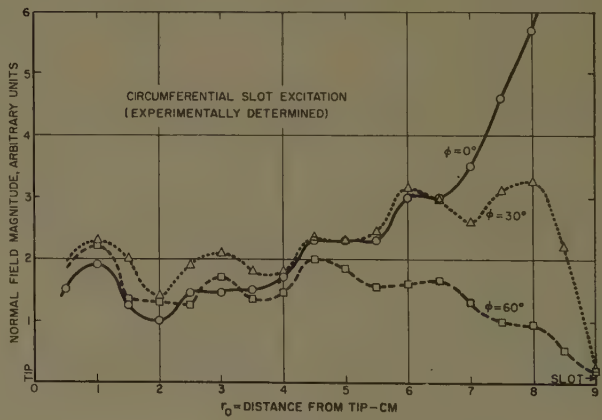

Fig. 3—Field distribution along elements of cone.

θ' being the angle that the radius would make with the slot. In (1) r is the distance from the slot and r_0 the distance from the tip. It was deduced further, that the coefficient of G_2 could be defined as $A=\Gamma G_1(kd)$, with Γ representing the reflection coefficient of the tip (d = the distance between the slot and the tip).

Theoretical evaluation of the fields of a cone excited by sources on the surface has yielded expressions consisting of the sum of an infinite seriess of Hankel func-

* Manuscript received by the PGAP, January 15, 1957.
† University of Washington, Seattle, Wash.
[1] R. Justice, "A Reflection Method of Measuring Near Field Distribution," Ohio State Univ., Antenna Lab. Rep. No. 486–28; September 30, 1954.

tions.[2] However, such series are slowly convergent, thus quite difficult to evaluate, particularly on the surface of the cone. Assuming that one could represent the sum of such series by single functions, combinations of Hankel functions of fractional and integer order were tried for G_1 and G_2 to fit the experimental data. The best fit to the experimental distribution was obtained with $G_1 = H_3^2(kr)$ and $G_2 = H_0^2(kr_0)$. Fig. 4 shows a comparison between an experimental curve along the $\phi = 0°$ and the assumed analytic expression. The choice for the coefficient A was arrived at by a number of trials. With this value for A and the definition of the reflection coefficient, Γ was found to be equal to $0.725e^{-j(3\pi/4)}$. Using this same value of the reflection coefficient, computed values of the field distribution along different elements were compared with the data of several other slot-to-tip distances. The agreement between the assumed expression and the experimental results was good.

[2] L. L. Bailin and S. Silver, "Exterior electromagnetic boundary value problems for spheres and cones," IRE TRANS., vol. AP-4, pp. 5–16; January, 1956.

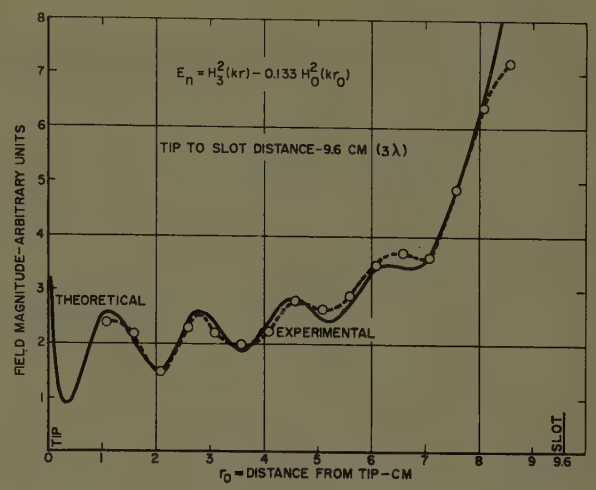

Fig. 4—Field distribution along element $-\phi = 0°$.

It should be noted that these measurements were made on a 28° cone. However, the outlined method can be applied to cones of any angle.

On the Simulation of Fraunhofer Radiation Patterns in the Fresnel Region*

DAVID K. CHENG†

Summary—**Physical limitations on the size of obstacle-free test sites give rise to the need of making radiation-pattern measurements on high-gain antennas at a reduced distance. The general practice is to defocus the primary source along the principal axis of the antenna reflector by a small distance so that Fraunhofer patterns may be simulated in the Fresnel region. This note summarizes and compares three different approaches with which the proper amount of defocus may be determined.**

THE PERFORMANCE of an antenna is usually specified in terms of the characteristics of its radiation pattern in the Fraunhofer region. This is because of the fact that Fraunhofer radiation patterns do not change with the distance from the antenna as long as the far-zone approximations are satisfied. Radiation patterns in the Fresnel region tend to be very complex, and they change considerably with distance.

While there is no clear-cut boundary between the Fraunhofer and the Fresnel regions, a common and acceptable criterion is that $2D^2/\lambda$ represents a safe far-zone distance, where D is the maximum dimension of the antenna aperture and λ is the operating wavelength. At a distance of $2D^2/\lambda$ the maximum path-length difference between the contribution from the edge of the aperture and that from the center corresponds to $\lambda/16$ or $\pi/8$ radians. In practice, an unobstructed, open space with a dimension of $2D^2/\lambda$ is often not available for testing high-resolution antennas. For example, the $2D^2/\lambda$ distance for a 20-foot antenna at 3 cm would be about 1.53 miles. Higher gain requirements would demand even larger test sites. Unfortunately, calculation of Fraunhofer radiation patterns from measurements in the Fresnel region is not of practical value at the present time both because of the difficult and laborious process of extrapolation and because of the inherent difficulties in making accurate amplitude and phase measurements.[1] The need for the technique of testing microwave antennas at reduced ranges is, therefore, both real and urgent.

A commonly used practice is to displace the primary source of the antenna assembly slightly from the focal position in a direction away from the reflector. The

* Manuscript received by the PGAP, February 27, 1956; revised manuscript received February 4, 1957. This work was supported by the Rome Air Development Center, USAF, under Contract No. AF 30(602)-1360.

† Elec. Eng. Dept., Syracuse Univ., Syracuse, N. Y.

[1] A. F. Kay, "Far Field Data at Close Distances," Final Rep. for Contract No. AF 19(604)-1126, Tech. Res. Group, New York, N. Y.; October, 1954.

present note summarizes three different methods with which the required amount of defocus may be determined.[2] The results are plotted and compared.

The Geometrical Approach

It is a well-known fact that for an effective point source of excitation, the best radiation pattern will be obtained from a paraboloidal reflector at a field point in the far zone when the source is located at the focal point of the reflector. Geometrically, this may be explained by equal path length from the source to all points in an aperture plane by virtue of the inherent property of a focused paraboloid. If the field point is far enough away from the reflector, the path lengths from the aperture points to the field point will be again approximately equal, resulting in an optimum additive effect. When the field point lies in the quasi-near zone (Fresnel region), the path-length differences from the points in an aperture plane to the field point must be compensated in some way in order that the measured radiation pattern may approach the true far-zone (Fraunhofer) pattern. This is done by slightly defocusing the source along the reflector axis in the direction away from the reflector. Since the amount of on-axis defocus is the only adjustable variable here, one cannot expect to achieve equal path length for all points in the aperture plane. For simplicity, the conventional approach is to make the path length from the source to the field point by way of the apex of the paraboloid equal to that by way of the points on the edge of the reflector.

Refer to Fig. 1, which represents a cross section of a symmetrical paraboloidal reflector with focal length $\overline{OF}=f$ and defocused point source at F', the above requirement is equivalent to making

$$\overline{F'O}+\overline{OO'}=\overline{F'A}+\overline{AB}. \tag{1}$$

Call $\overline{AA'}=D$ (aperture diameter), $\overline{O'P}=\overline{BP}=R$ (distance of measurement), $\overline{FF'}=\epsilon$ (defocus distance). Eq. (1) can be reduced to give

$$\epsilon=\frac{f^2}{R}\left[\left(\frac{R}{R-f}\right)+\left(\frac{D}{4f}\right)^2\right]. \tag{2}$$

When $(f/R)^2\ll 1$, it is accurate enough to write (2) as

$$\epsilon=\frac{f^2}{R}\left[1+\frac{f}{R}+\left(\frac{D}{4f}\right)^2\right]. \tag{3}$$

Normalizing all quantities with respect to the focal length and introducing new notations $\epsilon'=\epsilon/f$, $R'=R/f$, and $D'=D/f$, one can rewrite (3) as

$$\epsilon'=\frac{1}{R'}\left[1+\frac{1}{R'}+\left(\frac{D'}{4}\right)^2\right]. \tag{4}$$

The normalized amount of defocus needed is seen to increase when R' decreases and when D' increases. As R' approaches infinity, ϵ' correctly goes to zero.

[2] D. K. Cheng, "Microwave aerial testing at reduced ranges," *Wireless Eng.* vol. 33, pp. 234–237; October, 1956.

Fig. 1—Geometry of on-axis defocusing arrangement for paraboloidal reflector.

The Aperture-Phase Approach

The defocusing problem can also be approached from a consideration of the phase distribution in an aperture plane of the reflector together with the diffraction integral for the field at a point in space. When the point under consideration is in the quasi-near zone of a paraboloidal reflector, the normalized diffraction integral which gives the field pattern in a horizontal plane can be approximated as[3]

$$I(u)=\int_0^1 F(r)^{-jkD^2r^2/8R}rJ_0(ur)dr. \tag{5}$$

In (5), r is the radial dimension of the aperture plane normalized with respect to $D/2$; $u=(\pi D/\lambda)\sin\theta$, θ being the azimuth angle; $k=2\pi/\lambda$; and $F(r)$ is the circularly symmetrical amplitude illumination function over the aperture. The explicit exponential term is the Fresnel-region contribution; terms above the second order are neglected. When R is very large, (5) reduces to the far-zone pattern function

$$I_0(u)=\int_0^1 F(r)rJ_0(ur)dr. \tag{6}$$

When the primary source is displaced from the focus of a paraboloidal reflector along the reflector axis in the direction away from the reflector with a view to simulating far-zone patterns in the quasi-near zone, there will be a relative phase variation over the aperture. It has been found that this phase variation referred to the center point can be approximated satisfactorily by[4]

$$\delta\cong -2\epsilon\left[1-\frac{r^2}{\left(\frac{4f}{D}\right)^2+1}\right]. \tag{7}$$

Eq. (7) is exact for $r=0$ (center) and $r=1$ (edge of aperture). For other values of r, the $|\delta|$ given by (7) is slightly too large; the error decreases when the (f/D)

[3] S. Silver, "Microwave Antenna Theory and Design," M.I.T. Rad. Lab. Ser., McGraw-Hill Book Co., Inc., New York, N. Y., vol. 12, ch. 6; 1949.

[4] D. K. Cheng and S. T. Moseley, "On-axis defocus characteristics of the paraboloidal reflector," IRE Trans., vol. AP-3, pp. 214–216; October, 1955.

ratio of the reflector increases. The diffraction integral now becomes

$$I(u) = \int_0^1 F(r)e^{jk[\delta - D^2r^2/8R]}rJ_0(ur)dr. \tag{8}$$

In order to simulate Fraunhofer radiation patterns in the Fresnel region, the exponent under the integral sign in (8) should be made to vanish. This yields

$$\frac{\epsilon}{f} = \frac{f}{R}\left[1 + \left(\frac{D}{4f}\right)^2\right]$$

or

$$\epsilon' = \frac{1}{R'}\left[1 + \left(\frac{D'}{4}\right)^2\right] \tag{9}$$

which checks with (4) when $R' = R/f \gg 1$. If it is desirable to write

$$R' = nD'^2/\lambda' \tag{10}$$

with $\lambda' = \lambda/f$, n a numeric, then (9) reduces to

$$\frac{\epsilon'}{\lambda'} = \frac{\epsilon}{\lambda} = \frac{1}{n}\left[\left(\frac{1}{D'}\right)^2 + \left(\frac{1}{4}\right)^2\right]. \tag{11}$$

Eq. (11) shows that for a given value of D', (ϵ/λ) plotted vs n gives a hyperbola in linear scales, and a straight line in log-log scales.[4] It is noted that for $n = 2$ $(R = 2D^2/\lambda)$, appreciable defocus is still necessary.

The Ellipsoidal-Reflector Approach

The purpose of defocusing the primary source in the case of a paraboloidal reflector is to simulate far-zone radiation patterns at points in the quasi-near zone. In terms of geometrical optics, it is quite easy to see that this could be achieved by means of an ellipsoidal reflector. If the primary source is placed at one of the two foci of an ellipsoidal reflector, the reflected rays will converge at the other.

The equation in the xz plane of a cross section of an ellipsoidal reflector with focal lengths f_1 and f_2 is

$$z = \frac{f_1 + f_2}{2}\left[1 - \sqrt{1 - \frac{x^2}{f_1 f_2}}\right]. \tag{12}$$

Subject to the condition

$$\sqrt{1 - \frac{x^2}{f_1 f_2}} \cong 1 - \frac{x^2}{2f_1 f_2} \tag{13}$$

(13) can be approximated as

$$z = \frac{f_1 + f_2}{4f_1 f_2}x^2 \tag{14}$$

which is the equation for a parabola of focal length

$$f = \frac{f_1 f_2}{f_1 + f_2} \tag{15}$$

or

$$\frac{1}{f} = \frac{1}{f_1} + \frac{1}{f_2}. \tag{16}$$

Hence, for reflected rays to converge at $R = f_2$, the primary source should be placed at $z = f_1$, and

$$\epsilon = f_1 - f = \frac{f^2}{R - f} \tag{17}$$

or, in normalized form,

$$\epsilon' = \frac{1}{R' - 1} = \frac{1}{R'}\left[1 + \frac{1}{R'} + \frac{1}{(R')^2} + \cdots\right]. \tag{18}$$

Eq. (18) should be compared with both (4) and (9). ϵ' can also be expressed in terms of the focal lengths as

$$\epsilon' = \frac{f_1}{f_2} \tag{19}$$

which is extremely simple.

The basis of the ellipsoidal-reflector approach lies in the fact that an ellipsoidal reflector of focal lengths f_1 and f_2 approximates a paraboloidal reflector of focal length f as given by (15) or (16). An examination of (13) shows that it implies the condition $(1/8)(x^2/f_1 f_2)^2 \ll 1$. Now the maximum value of x is $D/2 \leq 2f_1$. This reduces the condition to

$$\frac{f_2}{f_1} \gg \sqrt{2} \tag{20}$$

which is undoubtedly true in practice. An ellipsoidal reflector with focal lengths f_1 and f_2 has its semimajor and semiminor axes equal to $(f_1 + f_2)/2$ (arithmetical mean) and $\sqrt{f_1 f_2}$ (geometrical mean), respectively; it approaches very closely a paraboloidal reflector when (20) is satisfied. As an example, with $f_2 = R = 50f_1$ the maximum error is less than 0.09 per cent.

Comparison of Defocusing Methods

Curves plotting ϵ' vs R' based upon (4), (9), and (19) from the three different approaches discussed above are shown in Fig. 2. It is seen that except for small values of R', the required ϵ' from the geometrical approach is nearly the same as that from the aperture-phase approach, both of which increase with increasing D'. The required ϵ' from the ellipsoidal-reflector approach is the smallest of the three methods and is independent of D'.

A review of the geometrical approach reveals that there is really no plausible justification in requiring equal path length from the source to the field point by way of the apex and by way of the points on the edge of the paraboloidal reflector only; the path lengths by way of the intermediate points on the reflector would then all be longer. Besides, there is no guarantee that the rays emanating from F' will be reflected to pass through the point P except the ray along the principal axis. The approximation (7) used in the aperture-phase approach is

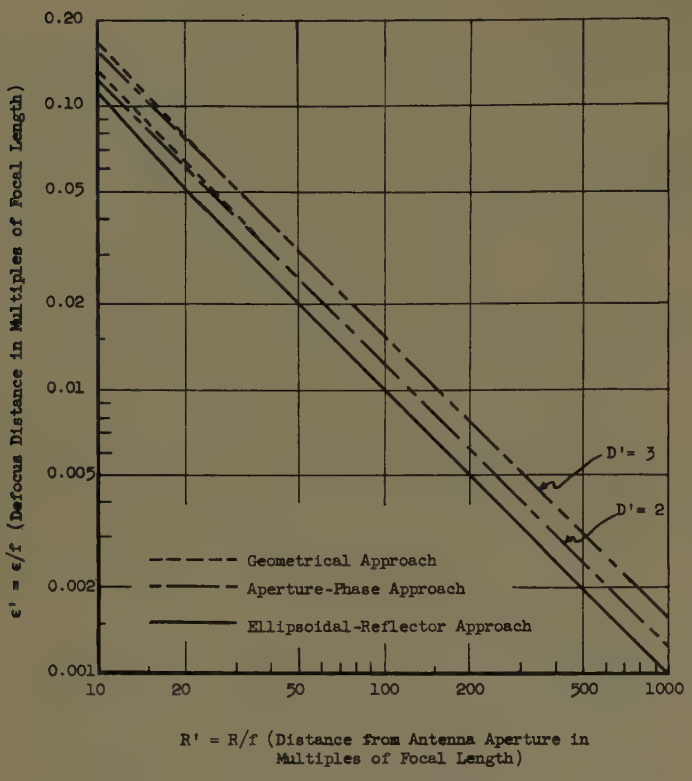

Fig. 2—Comparison of defocusing methods.

exact for $r=0$ and $r=1$ only; for $0<r<1$, δ, given by (7), is numerically too large resulting in an ϵ' which is also too large. It can be shown that the maximum error in δ introduced by (7) is

$$1-\frac{1}{\sqrt{1+q}}\left(2-\frac{1}{\sqrt{1+q}}\right) \tag{21}$$

where $q=(D/4f)^2$. For a reflector with $q=0.35$ or $D'=2.36$, the maximum error is about 5 per cent.

Although the geometrical approach and the aperture-phase approach yield approximately the same results, the aperture-phase approach makes it clear that this method would not be useful when R is too small because it would then be necessary to include terms higher than the second order in the exponent that appears in (5); the geometrical approach gives no indication of this resctriction. It is believed that ϵ' in (18) derived from the ellipsoidal-reflector approach gives the most nearly correct results because the approximation implied by (13) is very good; it does not restrict its correctness only to the edge of the reflector.

It should be noted that in all three methods the required amount of defocus is not a function of the operating wavelength and that diffraction phenomena are neglected.

Asymptotic Expansion of the Diffracted Wave for a Semi-Infinite Cone*

L. B. FELSEN†

IN a previous paper,[1] an asymptotic expression for the wave scattered by the tip of a semi-infinite cone has been obtained to first order in $(1/kr)$, where k is the free-space wave number and r is the distance from the cone tip (see Fig. 1, opposite). It is shown in this note how one may obtain higher order terms in $(1/kr)$.

I. Scalar Problem (Neumann Type)

In the domain $(\theta+\theta')<(2\theta_0-\pi)$, which excludes the rays reflected from the cone surface according to geometrical optics, the Neumann type Green's function $G'(\mathbf{r}, \mathbf{r}')$ satisfying the inhomogeneous wave equation,

$$(\nabla^2+k^2)G'(\mathbf{r}, \mathbf{r}')=-\delta(\mathbf{r}-\mathbf{r}'), \tag{1}$$

with $\partial G'/\partial\theta=0$ at $\theta=\theta_0$, radiation condition at $r\to\infty$ finiteness at $r=0$, can be represented exactly as[2]

$$G'(\mathbf{r}, \mathbf{r}')=\frac{e^{ik|\mathbf{r}-\mathbf{r}'|}}{4\pi|\mathbf{r}-\mathbf{r}'|}+G_s'(\mathbf{r}, \mathbf{r}'). \tag{2a}$$

A time dependence $\exp(-i\omega t)$ is assumed throughout. The diffracted wave term G_s' arising from the scattering by the cone tip is given by

$$\sqrt{rr'}G_s'=-\frac{1}{4\pi}\sum_{m=0}^{\infty}\epsilon_m\cos m(\phi-\phi')\cdot\int_{-\infty}^{\infty}dx\,x\,H_{ix}^{(1)}(kr)H_{ix}^{(1)}(kr')G_{\theta s}', \tag{2b}$$

$$G_{\theta s}'=\frac{\pi}{2}\frac{K_x^{-m}(\cos\theta)K_x^{-m}(\cos\theta')\Gamma(ix+m+\frac{1}{2})}{(-1)^{m+1}\cosh\pi x\,\Gamma(ix-m+\frac{1}{2})}\cdot\frac{(d/d\theta_0)K_x^{-m}(-\cos\theta_0)}{(d/d\theta_0)K_x^{-m}(\cos\theta_0)}, \tag{2c}$$

* Manuscript received by the PGAP, April 26, 1957. This work was performed in connection with a subcontract with Univ. Michigan on Purchase Order No. 154700.

† Microwave Res. Inst., Polytech. Inst. of Brooklyn, Brooklyn, N. Y.

[1] L. B. Felsen, "Plane-wave scattering by small-angle cones," IRE Trans., vol. AP-5, pp. 121–129; January, 1957. See (24) and (48).

[2] *Ibid.*, see (8).

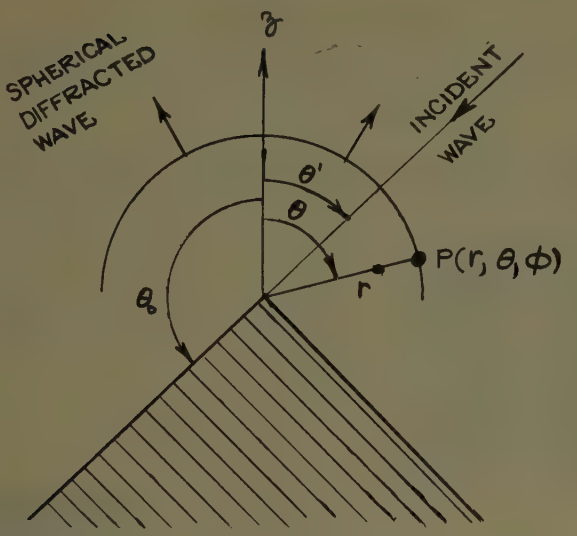

Fig. 1—Cone geometry.

$$K_x^{-m} = P_{-1/2+ix}^{-m};\ \epsilon_m = 1,\ m > 0;\ \epsilon_0 = \tfrac{1}{2}. \quad (2d)$$

For plane-wave incidence, $r' \to \infty <$, and we may employ the asymptotic formula[3]

$$H_{ix}^{(1)}(kr') \sim \sqrt{\frac{2}{\pi kr'}}\, e^{i(kr'-\pi/4)+x\pi/2}, \quad kr' \to \infty. \quad (3a)$$

If the wave is to be observed far from the cone tip so that kr is allowed to become very large, the complete asymptotic expansion for $H_{ix}^{(1)}(kr)$ is appropriate in the range $|kr| \gg |x|$:

$$H_{ix}^{(1)}(kr) \sim \sqrt{\frac{2}{\pi kr}}\, e^{i(kr-\pi/4)} e^{x\pi/2} \sum_{n=0}^{\infty} \frac{(ix, n)}{(-2ikr)^n}, \quad (3b)$$

$$(ix, n) \equiv (-1)^n \frac{(4x^2+1^2)(4x^2+3^2)\cdots[4x^2+(2n-1)^2]}{2^{2n} n!} \quad (3c)$$

$$= \frac{(-1)^n}{n!} (x^2+\tfrac{1}{4})(x^2+\tfrac{1}{4}+2)\cdots(x^2+\tfrac{1}{4}+n(n-1));$$

$$(ix, 0) \equiv 1. \quad (3d)$$

The integrand in (2b) decays exponentially with increasing $|x|$ in the domain $(\theta+\theta') < (2\theta_0 - \pi)$, so that the error incurred by employing the expansion (3b) over the entire range in x is exponentially small as $kr \to \infty$ and therefore, may be ignored. One then obtains the following asymptotic representation for the diffracted wave:

$$G_s' \sim \frac{i}{2\pi^2 k} \frac{e^{ik(r+r')}}{rr'} \sum_{n=0}^{\infty} \frac{A_n(\theta, \theta'; \phi, \phi')}{(-2ikr)^n}, \quad (4a)$$

where the coefficients A_n are given by

$$A_n = \sum_{m=0}^{\infty} \epsilon_m \cos m(\phi - \phi') \int_{-\infty}^{\infty} dx\, x\, e^{x\pi} (ix, n) G_{\theta s}'. \quad (4b)$$

[3] W. Magnus and F. Oberhettinger, "Special Functions of Mathematical Physics," Chelsea Pub. Co., New York, N. Y., p. 22; 1949.

Since the coefficients (ix, n) and $(ix, n-1)$ are related via (3d) by

$$(ix, n) = \frac{-1}{n} [x^2 + \tfrac{1}{4} + n(n-1)](ix, n-1),$$

$$n = 1, 2, \cdots, \quad (5)$$

and the K_x^m functions satisfy the differential equation

$$[L_m(\theta) - (\tfrac{1}{4} + x^2)] K_x^m(\cos\theta) = 0,$$

$$L_m(\theta) = \frac{1}{\sin\theta} \frac{d}{d\theta} \sin\theta \frac{d}{d\theta} - \frac{m^2}{\sin^2\theta}, \quad (6)$$

one may construct the coefficient A_n in (4b) from a knowledge of A_{n-1} by means of the formula

$$A_n = -\frac{1}{n}\left[\mathfrak{L}_0(\theta) + \frac{1}{\sin^2\theta} \frac{\partial^2}{\partial\phi^2} + n(n-1)\right] A_{n-1},$$

$$n = 1, 2 \cdots \quad (7)$$

$$\mathfrak{L}_0(\theta) = \frac{1}{\sin\theta} \frac{\partial}{\partial\theta} \sin\theta \frac{\partial}{\partial\theta}. \quad (7a)$$

It is assumed that the interchange of the order of differentiation and summation (integration) necessary to deduce (7) from (4b) is permissible. Thus, all coefficients in the asymptotic formula in (4a) can be obtained from successive application of (7) if A_0 is known. For small-angle cones ($\theta_0 \approx \pi$), the coefficient A_0 in (4b) previously has been evaluated approximately to $0[(\pi-\theta_0)^2]$ as[4]

$$A_0 \approx \pi \left[\frac{\pi - \theta_0}{2}\right]^2 \left[\frac{1 + \cos\theta\cos\theta'}{(\cos\theta + \cos\theta')^3} + \frac{2\sin\theta\sin\theta'}{(\cos\theta + \cos\theta')^3} \cos(\phi - \phi')\right]. \quad (8)$$

II. Vector Problem (Electromagnetic)

The dyadic electric and magnetic Green's functions $z(r, r')$ and $y(r, r')$, respectively, for a perfectly conducting semi-infinite cone can be expressed in terms of two scalar functions $S_1'(r, r')$ and $S_1''(r, r')$[5]. In the domain $(\theta+\theta') < (2\theta_0 - \pi)$, the total Green's functions can be represented analogously to (2a) as the sum of the free-space Green's function plus a diffracted wave term. The diffracted wave portions S_{1s}' and S_{1s}'' of S_1' and S_1'' contain a "residue contribution" which is 0(1) in kr and (kr'), plus an additional term to be denoted by $\bar{S}_{1s}'$ and $\bar{S}_{1s}''$, respectively:[6]

$$\bar{S}_{1s}''(r, r') = \sqrt{rr'}\, \frac{1}{4\pi} \sum_{m=0}^{\infty} \epsilon_m \cos m(\phi - \phi') \cdot \int_{-\infty}^{\infty} dx\, \frac{x}{x^2 + \tfrac{1}{4}} H_{ix}^{(1)}(kr) H_{ix}^{(1)}(kr') G_{\theta s}', \quad (9a)$$

[4] Felsen, *op. cit.*, see (24).
[5] *Ibid.*, see (32).
[6] *Ibid.*, see (35).

$$\bar{S}_{1s}'(r, r') = \sqrt{rr'}\,\frac{1}{4\pi}\sum_{m=0}^{\infty}\epsilon_m \cos m(\phi-\phi') \cdot \int_{-\infty}^{\infty} dx\,\frac{x}{x^2+\frac{1}{4}}\,H_{ix}^{(1)}(kr)H_{ix}^{(1)}(kr')G_{\theta s}, \quad (9b)$$

where $G_{\theta s}'$ is given in (2c). $G_{\theta s}$ has the same form as $G_{\theta s}'$ except that one replaces

$$\frac{(d/d\theta_0)K_x^{-m}(-\cos\theta_0)}{(d/d\theta_0)K_x^{-m}(\cos\theta_0)} \text{ by } \frac{K_x^{-m}(-\cos\theta_0)}{K_x^{-m}(\cos\theta_0)}. \quad (9c)$$

As $r'\to\infty$ and subsequently $kr\gg 1$, the asymptotic expansion of $\bar{S}_{1s}'$ and $\bar{S}_{1s}''$ can be carried out as in Section I to yield

$$\bar{S}_{1s}'' \sim \frac{-i}{2\pi^2 k}\,e^{ik(r+r')}\sum_{n=0}^{\infty}\frac{B_n''(\theta,\theta';\phi,\phi')}{(-2ikr)^n}, \quad (10a)$$

$$B_n'' = \sum_{m=0}^{\infty}\epsilon_m \cos m(\phi-\phi')\int_{-\infty}^{\infty} dx\,x\,e^{x\pi}\,\frac{(ix,n)}{x^2+\frac{1}{4}}\,G_{\theta s}', \quad (10b)$$

and

$$\bar{S}_{1s}' \sim \frac{-i}{2\pi^2 k}\,e^{ik(r+r')}\sum_{n=0}^{\infty}\frac{B_n'(\theta,\theta';\phi,\phi')}{(-2ikr)^n}, \quad (11a)$$

B_n' = same as B_n'' except that $G_{\theta s}'$ is replaced by $G_{\theta s}$. (11b)

The coefficients B_n'' and B_n' in (10b) and (11b) respectively, satisfy a recurrence relation identical with that for A_n in (7):

$$\begin{matrix} B_n' \\ B_n'' \end{matrix} = -\frac{1}{n}\left[\mathfrak{L}_0(\theta)+\frac{1}{\sin^2\theta}\,\frac{\partial^2}{\partial\phi^2}+n(n-1)\right]\begin{matrix} B_{n-1}' \\ B_{n-1}'' \end{matrix} \qquad n = 1, 2\ldots \quad (12)$$

In fact, the B_n coefficients are the more basic since one may derive the A_n coefficients from them through the relation [cf. (10b), (4b), and (6)]

$$\left[\mathfrak{L}_0(\theta)+\frac{1}{\sin^2\theta}\,\frac{\partial^2}{\partial\phi^2}\right]B_n'' = A_n, \quad n = 0, 1, 2\ldots \quad (13)$$

For the special case of an incident-plane wave polarized so that the electric vector is directed perpendicular to the cone axis, it can be shown that the $m=0$ term in the representation of B_n' [see (11b)] does not contribute to the scattered field. An approximate evaluation of the contributing portion of B_0' and B_0'' for small-angle cones has previously been shown to yield the following expressions to $0[(\pi-\theta_0)^2]$:[7]

$$B_0' \approx -\pi\left[\frac{\pi-\theta_0}{2}\right]^2\frac{\tan\frac{\theta}{2}\tan\frac{\theta'}{2}}{\cos\theta+\cos\theta'}\cos(\phi-\phi'), \quad (14a)$$

$$B_0'' \approx \frac{\pi}{2}\left[\frac{\pi-\theta_0}{2}\right]^2\cdot\frac{1}{\cos\theta+\cos\theta'} - B_0'. \quad (14b)$$

The coefficients for $n\geq 1$ are obtained then, from successive application of (12).

It is appropriate to point out at this time an error in algebraic sign which occurs in (45) of Felsen.[1] The first term on the right-hand side of (14b) corresponds to the above-cited reference and carries the correct algebraic sign. As a consequence of this error, (45), (48b), and (51) of Felsen must be corrected as follows:

(45): multiply right-hand side by -1.

(48b): multiply the ϕ-independent term by -1.

(51): replace

$$\left(\sin^4\frac{\theta}{2}+\cos\theta\cos^2\frac{\theta}{2}\right) \text{ by } \left(\sin^4\frac{\theta}{2}+\cos^2\frac{\theta}{2}\right).$$

[7] *Ibid.*, see (44) and (46).

Contributors

For a photograph and biography of M. G. Andreasen, see page 333 of the July, 1957 issue of these TRANSACTIONS.

❖

L. L. Bailin (SM'53) was born in Chicago, Ill. on May 28, 1922. He received the B.A. degree in physics from U.C.L.A. in 1943, and remained there for a year as a teaching assistant before joining the technical staff of the Naval Ordnance Laboratory in Washington, D. C. He returned to U.C.L.A. in 1945 for graduate study in physics and received the M.A. degree in 1946 and the Ph.D. degree in 1949.

L. L. BAILIN

In 1948 Dr. Bailin was employed as a mathematician by the Institute for Numerical Analysis of the National Bureau of Standards. From 1949 to 1955, he was engaged in microwave propagation and antenna studies as a member of the technical staff of Hughes Aircraft Company. In 1953 he joined the faculty of the University of Southern California, where he is now Professor of electrical engineering.

Dr. Bailin is a member of the American Physical Society, Sigma Xi, RESA, Pi Mu Epsilon, and Eta Kappa Nu.

❖

Martin Balser was born in Brooklyn, N. Y., on May 23, 1927. He served in the Army from 1945 to 1947. He then received the B.S. degree, summa cum laude, from Brooklyn College in 1948, and the M.A. degree and the Ph.D. degree in theoretical physics in 1949 and 1953 respectively, both from Harvard University. He was a Teaching Fellow at Harvard from 1950 to 1952.

M. BALSER

Mr. Balser is currently affiliated with the Lincoln Laboratory at the Massachusetts Institute of Technology where he is working in radio wave propagation and communication theory.

He is a member of Pi Mu Epsilon and Sigma Xi.

George Bekefi was born in 1925 in Prague, Czechoslovakia. He received the B.S. degree from the University of London in 1948 and the M.S. and Ph.D. degrees from McGill University in 1950 and 1952, respectively. He was assistant professor at McGill University where he also carried out research in the field of microwave optics. In 1957 he joined the Micro wave Gas Discharge Group at the Massachusetts Institute of Technology, Cambridge, Mass.

G. BEKEFI

Mr. Bekefi is a member of the Canadian Association of Physicists.

❖

Philipp Blacksmith, Jr. (S'48–A'50–M'54) was born in Liebling, Romania, October 12, 1921. He received the Bachelor of Science degree in physics from Carnegie Institute of Technology in 1949. He completed course requirements for the Master's degree in electrical engineering at the Air Force Institute of Technology in 1954 and has continued graduate work at Northeastern University.

P. BLACKSMITH

He was employed as a research engineer by AMP, Inc., working on dielectric materials and pulse forming networks. As an Air Force officer, he was assigned as a research engineer to the Antenna Laboratory at Air Force Cambridge Research Center, where he now serves as a civilian scientist. He has done original work on electromagnetic scattering and array scanning.

Mr. Blacksmith is a member of the American Institute of Physics.

❖

Erik V. Bohn (A'54) was born in Klintum auf Foehr, Germany, on March 13, 1924. He received the Dipl. Math. degree in 1948 and the Dr. Rer. Nat. degree in applied mathematics and physics in 1951, from the University of Goettingen, Germany. In 1951 he joined the Canadian Marconi Company, Montreal, Can., where he was engaged in the design and development of broad-band antenna arrays. In 1952 he joined the Canadian Aviation Electronics Company, Montreal, as a project supervisor, working on the design and development of servo-mechanisms and analog computers used in flight and fire control simulation. Since 1954 he has been a member of the Department of Electrical Engineering, University of British Columbia, Vancouver.

E. V. BOHN

❖

G. G. Cloutier was born on June 29, 1928, in Quebec City, Can. He studied at Laval University, Quebec, where he received the B.A. degree in 1949 and the B.S. degree in physics in 1953. Mr. Cloutier was employed in the research laboratories of the Defence Research Board of Canada from the spring of 1953 to the fall of 1954. He received the Master of Science degree in physics in 1956 from McGill University, Montreal, Canada, where he is presently carrying out his graduate studies.

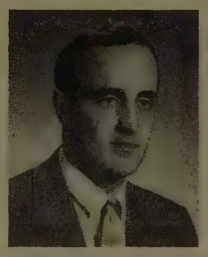

G. G. CLOUTIER

Mr. Cloutier is a member of the Canadian Association of Physicists and Sigma Xi.

❖

George R. Forbes, Jr. was born in Boston, Mass., May 22, 1920. He attended Oshkosh Wisconsin State Teachers College and Northeastern University. Mr. Forbes joined the U. S. Army Air Force in 1942 where he specialized in radar counter measure and became an instructor. In 1946, Mr. Forbes joined the Air Force Cambridge Research Center in the Radar Countermeasure Laboratory. In 1947, he transferred into the Antenna Laboratory where he has done basic research on metal plate lens, reflectors, and new type radiators from waveguide and other transmission media.

G. R. FORBES

Louis A. Kurtz (S'44–A'46–M'55) was born on March 13, 1923 in Long Beach, Calif. He received the B.S. degree in 1945 and the M.S. degree in 1951 from the University of California in Berkeley. He was a teaching assistant at the University of California from 1947 to 1949, as well as a research engineer for the U. S. Navy Antenna Project at the University.

L. A. KURTZ

In 1949, Mr. Kurtz was employed by the Dalmo Victor Company as a development engineer. Following this, he became a member of the technical staff of the Microwave Laboratory, Hughes Aircraft Company, where he was engaged in the development of linear and two-dimensional slot arrays, phase shifters, hybrid junctions, and other microwave antennas and components. He is presently head of the Microwave Antenna Department of Rantec Corporation.

Mr. Kurtz is an associate member of Sigma Xi.

❖

Edward K. Proctor (SM'51) was born in Lumberton, N.C., on July 11, 1922. He received the B.S. degree from North Carolina State College in 1943, and the M.S. degree from Harvard University in 1947. In addition he has completed one year of graduate study in applied mathematics at New York University and is presently attending Stanford University on a part-time basis under the Honors Cooperative Program.

E. K. PROCTOR

Following completion of his undergraduate studies, Mr. Proctor worked with the General Electric Company as a test engineer on several radar projects, and with the Tennessee Eastman Corporation at Oak Ridge, Tennessee, on the design of electronic controls. Upon finishing his graduate work following World War II, he accepted a position as a project engineer and, later, senior project engineer at the Sperry Gyroscope Company, where he was engaged in the development and design of microwave antennas. He was then appointed Engineering Section Head for Microwave Component Engineering at the Sperry Gyroscope Company, in which position he was responsible for the development and production of microwave circuit elements for a wide variety of microwave systems. Since February, 1955, he has been a member of the technical staff at the General Electric Microwave Laboratory in Palo Alto, Calif.

Mr. Proctor is a member of Eta Kappa Nu.

❖

Manfred H. Rees was born in Nuernberg, Germany. He received the Bachelor of Science degree in electrical engineering in 1948 from West Virginia University and the Master of Science degree in physics in 1956 from the University of Colorado where he is now completing his dissertation for the Ph.D. degree in physics.

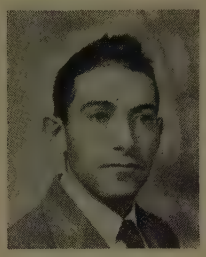

M. H. REES

Mr. Rees worked on a telemetering project for the NACA at Langley Field, Va., and on several antenna development projects for the Sperry Gyroscope Company, Great Neck, N.Y. He has also worked as a research assistant in biophysics at the University of Colorado Medical School. At present, he is an instructor in physics at the University of Colorado and is engaged in research on upper atmosphere physics with the Boulder Laboratories of the National Bureau of Standards.

Mr. Rees is a member of the American Physical Society and of RESA.

❖

Carlyle J. Sletten (A'51–M'56) was born in Chetek, Wis., on January 13, 1922. He received the Bachelor of Science degree with honors in physics from the University of Wisconsin in 1947, and the Master's degree in applied physics from Harvard University in 1949.

C. J. SLETTEN

Mr. Sletten served for more than three years in the Air Corps during World War II as a Meteorologist and Radar Weather Officer. He has been with the Antenna Laboratory of the Air Force Cambridge Research Center since 1948. During that time he has published several papers on antennas and electromagnetic scattering.

Mr. Sletten is a member of Phi Beta Kappa, the American Optical Society, and the Scientific Research Society of America

Robert J. Spellmire (M'56) was born on March 8, 1926, in Santa Monica, Calif. He received the Bachelor of Science degree in mathematics from the University of San Francisco in 1950.

R. J. SPELLMIRE

Since 1950 he has been associated with the Research Laboratories of Hughes Aircraft Company, Culver City, Calif., where he is working in the field of antenna research.

❖

Robert E. Webster (A'53) was born in Montgomery, Ala., on January 11, 1928. He received the B.E. degree from Vanderbilt University, Nashville, Tenn., in 1950 and the M.S. degree from the Ohio State University in 1951.

R. E. WEBSTER

Since 1951, he has been a research associate at the Antenna Laboratory of Ohio State University. His major interests have been in vehicular antennas and radomes.

Mr. Webster is a member of Tau Beta Pi and Sigma Xi.

❖

James S. Yee was born in Canton, China on October 24, 1927. He received the B.S. degree in physics in 1952, and the M.Sc. degree in electrical engineering in 1956, both from the University of Washington, Seattle, Wash.

J. S. YEE

From 1952 to 1953, he was with the U. S. Geological Survey, Sacramento, Calif.; from 1953 to 1954, he was a research fellow, Electrical Engineering Department, University of Washington; from 1954 to 1955, he was with Boeing Airplane Co., working on radar tracking error problems; from 1955 to 1957, he was at Hughes Aircraft Co., engaged in linear and two-dimensional slot array designs, surface wave research, and electromagnetic diffraction problems. He is presently with the Boeing Airplane Co.

Mr. Yee is a member of Phi Beta Kappa and an associate member of Sigma Xi.

Index to

IRE TRANSACTIONS

ON

ANTENNAS AND PROPAGATION

Volume AP-5, 1957

IRE Transactions on Antennas and Propagation

Index to Volume AP-5, 1957

Contents

Index to Authors

Numbers refer to index numbers in contents listing

Index to Technical Subjects

Index to Nontechnical Subjects

Chapter News

Group News

Meetings

People

PROCEEDINGS OF THE SYMPOSIUM ON ELECTROMAGNETIC WAVE THEORY

Because of continued demand, consideration is being given to reprinting the Proceedings of the URSI Symposium on Electromagnetic Wave Theory, held at the University of Michigan in June, 1955, and published in the IRE TRANSACTIONS ON ANTENNAS AND PROPAGATION, Vol. AP-4, No. 3, July, 1956.

This 400-page volume contains 45 invited papers and five panel discussions, representing an unusually valuable and comprehensive cross-section of the latest theories of the world's foremost authorities. Because of exceptionally heavy demand, stock copies were exhausted immediately after publication.

To help assess the need for a reprint edition, your help is requested. If you would like to purchase a copy at a cost consistent with the size of the edition, please so indicate by writing to:

DR. K. M. SIEGEL
Dept. of Electrical Engineering
University of Michigan
Ann Arbor, Michigan.

The reprinting would be made possible through the cooperation and support of the University of Michigan Press and Engineering Research Institute.

ANTENNA PROBLEMS?

Ask Kennedy!

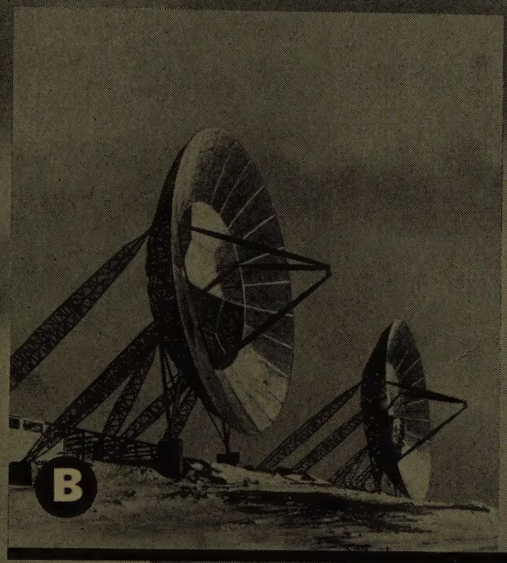

A *60′ Radio Telescope*
Harvard University

B *60′ Trans-horizon Antennas*
Northern Europe

C *120′ Radar Antenna*
Maine

D *28′ Trans-horizon Antennas*
Cape Cod

E *28′ Trans-horizon Antenna*
Texas Tower

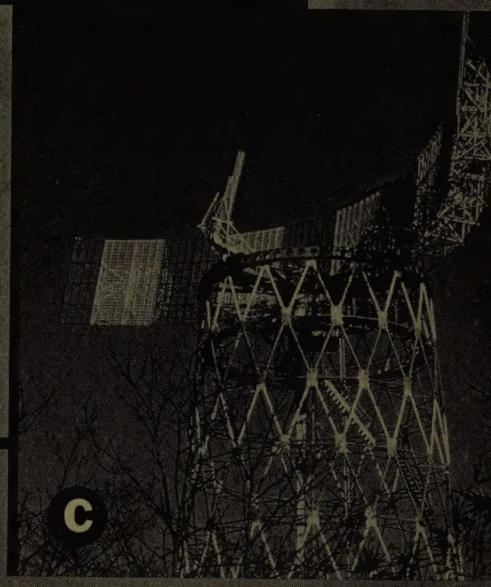

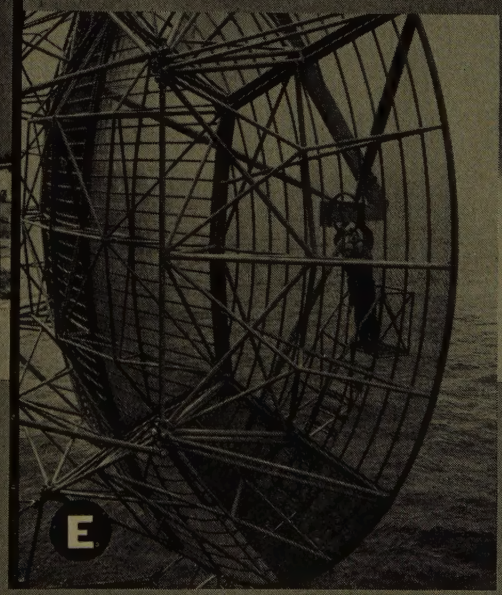

The solution to antenna problems begins when someone says: "Let's ask Kennedy!"

A few of the many reasons why are shown on this page. These Kennedy antennas are setting new standards for all-weather reliability and versatility wherever they serve throughout the free world.

Kennedy antennas come in many shapes, many sizes (the world's largest scatter antenna is being built here). But whatever the type, and whatever the conditions under which it must serve, Kennedy can offer a design that fully measures up to specifications. And there are additional advantages in Kennedy's advanced construction techniques — like the extra ease in shipping and handling made possible by sectionalized aluminum construction, for example.

Kennedy engineers are available to supervise installations anywhere in the world. It's a part of the complete, integrated service that is still another reason why more and more people in communications are "asking Kennedy" about antenna problems.

ANTENNA EQUIPMENT

D. S. KENNEDY & CO.

COHASSET, MASS. — TEL: CO4-1200

Down-To-Earth **SOLUTIONS** *to*
Out-Of-This-World **PROBLEMS**

Tracking Antennas
Radio Telescopes
Radar Antennas
Tropospheric Scatter
Ionospheric Scatter

INSTITUTIONAL LISTINGS

The IRE Professional Group on Antennas and Propagation is grateful for the assistance given by the firms listed below, and invites application for Institutional Listing from other firms interested in the field of Antennas and Propagation.

ANDREW CORPORATION, 363 E. 75th St., Chicago 19, Ill.
Antennas, Antenna Systems, Transmission Lines, Development and Production.

ANTLAB, 4950 North High St., Columbus 14, Ohio
Antenna Pattern Range Systems—Recorders & Mounts.

BLAINE ELECTRONETICS, INC., 14757 Keswick St., Van Nuys, Calif.
Antennas, Paraboloids, Scale Models, Antenna Radiation Pattern Measurement Towers

COLLINS RADIO COMPANY, Cedar Rapids, Iowa
Antenna Design and Propagation Research Related for Airborne and Ground Communication Systems.

DEVELOPMENTAL ENGINEERING CORP., 1001 Conn. Ave. N.W., Washington, D. C. and Leesburg, Va
Research, Development, Installation of Antennas and Antenna Equipment for Super Power Stations.

THE GABRIEL LABORATORIES, Div. of the Gabriel Co., 135 Crescent Road, Needham Heights 94, Mass
Research and Development of Antenna Equipment for Government and Industry.

HUGHES AIRCRAFT COMPANY, Culver City, Calif.
Research, Development, Mfr.: Radar, Missiles, Antennas, Radomes, Tubes, Solid State Physics, Computers.

I-T-E CIRCUIT BREAKER CO., Special Products Div., 601 E. Erie Ave., Philadelphia 34, Pa.
Design, Development and Manufacture of Antennas, and Related Equipment.

JANSKY & BAILEY, INC., 1339 Wisconsin Ave. N.W., Washington 7, D. C.
Radio & Electronic Engineering; Antenna Research & Propagation Measurements; Systems Design & Evaluation

MARYLAND ELECTRONIC MANUFACTURING CORPORATION, College Park, Md.
Antenna and System Development and Production for Civil and Military Requirements.

THE RAMO-WOOLDRIDGE CORPORATION, Los Angeles 45, Calif.

TRANSCO PRODUCTS, INC., 12210 Nebraska Ave., Los Angeles 25, Calif.
Res., Design, Dev., & Mfr. of Antenna Systems & Components for Missile, Aircraft & Ground Installations.

WHEELER LABORATORIES, INC., 122 Cutter Mill Road, Great Neck, N. Y.
Consulting Services, Research and Development, Microwave Antennas and Waveguide Components

The charge for an Institutional Listing is $25.00 per issue or $75.00 for four consecutive issues. Application may be made to the Technical Secretary, The Institute of Radio Engineers, 1 East 79th Street, New York 21, N.Y.